Radiation Reaction in the Interaction of Ultraintense Laser with Matter and Gamma Ray Source

ONG JIAN FUH

Department of Physics
Graduate School of Science
Osaka University
Osaka JAPAN

July 26, 2016

Radiation Reaction in the Interaction of Ultraintense Laser with Matter and Gamma Ray Source

ONG JIAN FUH

THESIS SUBMITTED IN FULFILMENT OF THE REQUIREMENTS FOR THE DEGREE OF DOCTOR OF PHILOSOPHY

Department of Physics
Graduate School of Science
Osaka University
Osaka JAPAN

July 26, 2016

Abstract

Radiation reaction (RR) force plays an important role in gamma ray production in the interaction of ultraintense laser with relativistic electron beams at the laser intensity beyond 10^{22} W/cm^2. The relationship between emission spectrum and initial kinetic energy of the electrons at such intensities has not been studied experimentally yet. The energy from both the relativistic electron beams and laser pulse may be converted into the gamma rays. Therefore, the conversion efficiency of energy purely from laser pulse into gamma rays is of great interest. We can use them as an alternative gamma ray source if the conversion efficiency is high enough.

We present the simulation results for the dynamics of an electron in strong laser field by taking into account the effects of RR. We have investigated how the effects of RR affect the emission spectrum and photon number distribution for different laser and electron beam conditions. We found that the peak locations of emission spectra are suppressed for higher initial kinetic energies of the electron interact with a long laser pulse duration.

We have studied the conversion efficiencies of laser energy into gamma ray energy. We found that that an electron with an energy of 40 MeV would convert maximally 80 $\%$ of the sum of electromagnetic work and its initial kinetic energy to the radiation energy when interacting with 10 fs laser pulse at the laser intensity of 2×10^{23} W/cm^2. By using this estimation, a bunch of electrons with the maximum charge of 1 nC at Helmholtz-Zentrum Dresden-Rossendorf (HZDR) would emit around 0.1 J of energy into gamma ray emis-

sion.

The laser field energy depletion can be neglected for a single electron. When considering a realistic electron beam with 10^9 electrons, the laser energy depletion has to be included, and we have to solve Maxwell's equations self-consistently via Particle-in-Cell (PIC) method. For this purpose, we performed three-dimensional PIC simulation by considering the interaction of a pulsed Gaussian beam with a finite size electron beam. We present the simulation results for electron charge density in strong laser field with and without RR. We investigate how the ponderomotive force affects the emission process at laser intensity more than 10^{23} W/cm^2. When treated self-consistently, however, the conversion efficiency reduces to 8% due to the laser field energy depletion. This is because the laser field energy reduction is sensitive to the motion perpendicular to the laser beam. As the energy of the electron beam increases, the laser energy reduction is relatively small. We emphasise that to obtain efficient gamma ray production at laser intensity more than 10^{23} W/cm^2, an electron beam with energy more than 1 GeV is required to reduce the laser energy change. The same requirement is also necessary in order to observe a clear signature of radiation reaction in the radiation spectrum at high power laser facility such as Extreme light Infrastructure (ELI) where the laser intensity is expected to reach the order of 10^{23-26} W/cm^2.

Acknowledgements

I would like to thank my supervisor, Professor Hideaki Takabe who shows great expertise and having his patience in this research. Special thanks to Professor Hosaka Atsushi for willing to become my new supervisor after the retirement of Professor Hideaki Takabe from Osaka University. Next, many thanks to Dr. T. Moritaka for guidances and advice on computer simulation throughout the research. Thanks to Teo Wei Ren, Wadagaki Tomoya for supports during the stay at Osaka. I would also like to thank Maxim Barkov for fruitful discussion. Besides, I would like to thank Professor Tom Cowan and R. Sauerbrey, HZDR, for their interest in the present research and encouragement during our research at Dresden, Germany. Thanks to Dr. Huang Lin Gen, Melanie Rödel and group members of HIBEF committee for useful discussion and support during my stay at HZDR. This work was partially supported by the General Coordinated Research program at National Institute for Fusion Science (NIFS13KNSS039) and also computer facilities at Cybermedia Center of Osaka University. Last but not least, I would like to thanks to my parents for their support and encouragement in my Ph.D. study.

Contents

List of Figures

Chapter 1

Introduction

The intensity of the laser has increased dramatically since the introduction of chirped pulse amplification (CPA) [2]. This opens up the opportunity for light-matter interaction into the relativistic regime. For instance, an electron at rest becomes relativistic in one laser period if the normalized laser amplitude exceeds unity such that

$$a_0 = \frac{|e||\mathbf{E}|}{mc\omega_0} \gtrsim 1 \tag{1.1}$$

where e and m are the charge and mass of the electron respectively, c is the speed of light, $|\mathbf{E}|$ and ω_0 are the amplitude and frequency of the laser respectively. The normalized laser amplitude is expressed in terms of laser wavelength and laser intensity as

$$a_0 = 0.85 \times 10^{-9} \lambda[\mu\text{m}] \sqrt{I[\text{W/cm}^2]}. \tag{1.2}$$

The corresponding laser intensity for $a_0 \sim 1$ is 10^{18} W/cm^2 for $\lambda = 1$ μm. To date, focused laser intensity of the order of $\sim 2 \times 10^{22}$ W/cm^2 was experimentally achieved by the 300 TW HERCULES laser [3]. The "Moore's law" trend for laser (see Fig.1.1) predicts that the laser intensities are expected to reach to the order of 10^{25} W/cm^2 at Extreme Light Infrastructure (ELI) [4]. At such extreme intensities the exotic physics such as radiation reaction (RR) effects, e^--e^+ pair plasma and nonlinear Quantum Electrodynamics (QED) may be tested [5]. On the other hand, quantum field theory describes that the vacuum is

not empty. Instead, virtual particles and antiparticles can be created and annihilated in an extremely short time allowed by Heisenberg uncertainty principle. When an external electric field is applied to the vacuum at the Schwinger limit

$$E_S = m^2c^3/e\hbar = 1.3 \times 10^{16}\text{V/cm}, \tag{1.3}$$

real e^--e^+ pairs can be produced. The Schwinger limit is the critical electric field that needed to separate a virtual electron-positron pair out of vacuum providing the energy that exceeds the electron rest mass energy mc^2 over a Compton wavelength $\lambda_C = \hbar/mc$. However, the corresponding laser intensity at Schwinger limit is

$$I_S = 2.3 \times 10^{29}\text{W/cm}^2 \tag{1.4}$$

and perhaps difficult to be archived at ELI in the near future. On the contrary, Bell and Kirk [6, 7] showed that pair production can be archived by two counterpropagating circularly polarized laser beams at the laser intensity of the order of 10^{24} W/cm^2. The seed electron is confined for a long time by two counterpropagating pulse lasers to emit high energy photons. The high energy photons then interact with the laser to produce pairs. These pairs repeat the same process and trigger an avalanche which is usually called QED cascades. The studies of QED cascades by using the laser in laboratory [8, 9, 10] become popular as it plays an essential role in understanding the high-energy astrophysical phenomena [11, 12].

At the intensity of the order of 10^{23} W/cm^2 and above the effects of radiation reaction become dominant in a single laser period [13]. The dynamics of an electron changes significantly due to its own radiation emission. The study of radiation reaction were pursued vigorously by Lorentz, Abraham, and Dirac in the context of classical electrodynamics. The covariant expression for radiation reaction is known as Lorentz-Abraham-Dirac (LAD) equation [14, 15, 16]. However, the solution of this equation suffers from the physical inconsistency where an electron is accelerated exponentially in the absence of an external field.

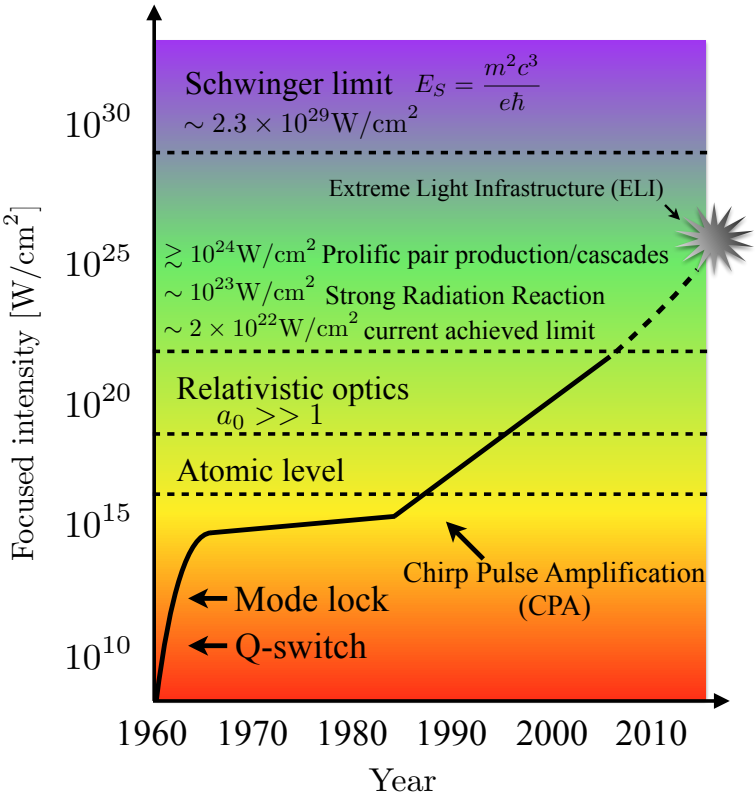

Figure 1.1: The "Moore's law" for laser.

An alternative way to avoid such physical inconsistency was proposed by Landau and Lifshitz such that the RR reaction is small as compared to the Lorentz force in the instantaneous rest frame of the electron. Therefore, radiation reaction force was considered as terms of first order perturbation and the Landau-Lifshitz (LL) [17] equation was obtained. The acceleration of an electron described by the LL equation vanishes as the external field goes to zero.

Apart from the LL model, there were many different models proposed to solve the inconsistency of the LAD equation (see Ref. [18] for a review of different models). In spite of many models proposed, the LAD equation is still the subject of extensive investigation and is still an open question.

In addition, QED effects such as electron recoil become substantial if the electric field exceeds the Schwinger limit or $\chi \geq 1$ where

$$\chi = \frac{\hbar}{mc}\frac{\sqrt{-f_L \cdot f_L}}{mc^2} \tag{1.5}$$

is the relativistic gauge invariant parameter and

$$f_L^\mu = \gamma(\mathbf{f}_{Le} \cdot \mathbf{u}/c, \mathbf{f}_{Le}), \tag{1.6}$$

$\mathbf{f}_{Le}$ is the Lorentz force and $\mathbf{u} = c^2\mathbf{p}/\sqrt{m^2c^4 + \mathbf{p}^2c^2}$. It is very hard to achive such condition even at 10^{23} W/cm^2 for a non-relativistic electron. However, this is possible if an ultrarelativistic electron interacts with a counterpropagating laser field where the laser frequency "seen" by the electron is Doppler up-shifted. Therefore, the laser field undergoes Lorentz transformation and exceeds the Schwinger limit. For an ultrarelativistic electron initially counterpropagating with respect to the laser this parameter is expressed as [19]

$$\chi = 2\frac{\hbar\omega_0}{mc^2}\gamma_0 a_0. \tag{1.7}$$

For instance, the condition $\chi \sim 1$ can be achived for a counterpropagating 1 GeV electron interacting with a laser field at intensity 2×10^{22} W/cm^2. This configuration is widely utilized in the production of high energy radiation such as Thomson backscattering and is distinguished from Compton backscattering if quantum effects are important.

The mechanism of Thomson/Compton backscattering is of key importance for high brilliance x-ray or gamma ray production. Such high brilliance sources are of interest in many applications. For example, resonant photonuclear isotope transmutation (RPIT) and resonant photonuclear isotope detection (RPID) [see Appendix A]. For such process to be effective, the gamma rays in the energy range of 10 - 20 MeV with photon intensity more than $10^{13}/s$ in 0.1% bandwidth is required. A recent experiment is capable to produce gamma rays with photon intensity of the order of $10^{17}/s$ in 0.1% bandwidth at 15 MeV via nonlinear relativistic Thomson scattering with laser intensity of the order of 10^{18} W/cm^2 [20]. On top of that, one may expect that if we increase the laser intensity and initial electron beam energy the photon production rate may increase subsequently.

However, the physics of photon production at the laser intensity of the order of 10^{22} W/cm^2 and beyond may not rely solely on Compton/Thomson backscattering. At these intensities ($a_0 >> 1$) the processes become nonlinear and the effect of radiation

reaction also comes into play [21]. The laser energy conversion rate, emission spectrum, and photon production rate may be greatly different from what we expect. Therefore, the production of gamma rays at such intensities becomes a subject of great interest to us.

In the previous studies on related topics, the conversion efficiency of laser energy into gamma ray was measured by calculating the ratio of total emitted energy to laser pulses energy [22, 23, 19]. However, extra care has to be taken when measuring the conversion efficiency for an electron beam from linear accelerator when radiation reaction effect is included. This is because the energy from the electron beam can be converted into radiation emission.

A remarkable experiment was done at Stanford Linear Accelerator (SLAC) by using 46.6 GeV electron beam collide with a terawatt laser at $I \sim 10^{18}$ W/cm^2 ($a_0 \simeq 0.8$, $\chi \simeq 0.4$) to study the nonlinear QED effects [24]. In addition, a laser-Thomson backscattering experiment was carried out at Helmholtz-Zentrum Dresden-Rossendrof (HZDR) with DRACO Ti:sapphire laser system and the ELBE linear accelerator [25]. Electron bunches of 22.5 MeV with charge of 77 pC undergo head-on collision with the laser at $a_0 \simeq 0.05$. There is no similar experiment performed up to date at $I \gtrsim 10^{22}$ W/cm^2. Thus, theoretical predictions of laser-matter interaction would help to determine the feasibility of such experiments at higher power laser facilities, in particular, the ongoing upgrade of DRACO laser system to 500 TW and high peak power diode-pumped laser system PEnELOPE [26] at HZDR.

The goals of this thesis are listed below:

1. To find out how the radiation spectra change with the inclusion of radiation reaction and how the interacting electron trajectory changes consequently.

2. To find out if the emission spectra are changed then how much the change is for high energy gamma ray.

3. To find out what are the optimized conditions for high energy gamma ray production for applications.

This thesis is organized as follows. In Chapter 2, we review the LAD equation and different models proposed to solve the physical inconsistency. We discuss the classical radiation dominant regime and moderate quantum regime and observe that the classical emission overestimates the production of high energy photon.

In Chapter 3, we describe our numerical approach and compare it to recent experimental results. After that, we present the trajectories, time evolution of electron energy, radiation spectrum, photon number distribution and radiation angular distribution in the same chapter. We found the suppression of the peak locations of radiation spectra as a result of cumulative effects of RR. A maximum conversion efficiency is observed for an electron with the energy of 40 MeV interacting with 10 fs laser pulse at the laser intensity of 2×10^{23} W/cm^2.

In Chapter 4, we discuss the concept of Particle-in-Cell method. A realistic laser beam such as pulsed Gaussian laser beam is discussed in this chapter.

In Chapter 5, we present the 3D PIC simulation results of 40 MeV and 1 GeV electron beam. We show that the ponderomotive force plays a crucial role in determining radiation emission. The laser field energy depletion is then shown to reduce the conversion efficiency when compared to the case of the single-particle model.

Conclusions are given in Chapter 6. Finally, we discuss the uses of gamma ray in resonant photonuclear isotope transmutation (RPIT) and resonant photonuclear isotope detection (RPID) in Appendix A.

Chapter 2

Radiation Reaction

2.1 Lorentz-Abraham-Dirac

The dynamics of an electron in external electric and magnetic field is governed by the Lorentz equation

$$\mathbf{f}_{Le} = e[\mathbf{E} + \mathbf{u} \times \mathbf{B}] \tag{2.1}$$

where $\mathbf{E}$ and $\mathbf{B}$ are the electric and magnetic field. Radiation emission of an accelerated electron is not taken into account. During radiation emission, energy and momentum are lost and this leads to a radiation reaction force which is in the opposite direction of motion. As a result, the dynamics of an electron is modified. The radiation reaction is one of the most fundamental problems in the classical electrodynamics and is still widely studied in present days. The first attempt to take into account the effect of radiation reaction in nonrelativistic regimes was done by Lorentz [27]. The radiation reaction force was derived from the Larmor formula which gives the power emitted by accelerated electron and the energy loss corresponding to the reaction force. The equation of motion is written as

$$m\dot{\mathbf{v}} = \mathbf{F}_{ext} + \mathbf{F}_{rad} \tag{2.2}$$

where $\mathbf{F}_{ext}$ is the Lorentz force and $\mathbf{F}_{rad}$ is the reaction force. Assuming the particle motion is periodic, the average work done by the radiation reaction force is equal to negative of the Larmor formula integrated over one period from t_1 to t_2. Integrating the Larmor power formula we obtain

$$\begin{aligned}\int_{t_1}^{t_2} \mathbf{F}_{rad} \cdot \mathbf{v} dt &= -\int_{t_1}^{t_2} \frac{2}{3}\frac{e^2}{c^3}\dot{\mathbf{v}} \cdot \dot{\mathbf{v}} dt \\ &= \frac{2}{3}\frac{e^2}{c^3}\int_{t_1}^{t_2} \ddot{\mathbf{v}} \cdot \mathbf{v} dt - \frac{2}{3}\frac{e^2}{c^3}\dot{\mathbf{v}} \cdot \mathbf{v}|_{t_1}^{t_2}. \end{aligned} \tag{2.3}$$

The second term or the boundary term on the right-hand side of Eq. (2.3) vanishes for periodic motion of an electron in an external field and then we can write

$$\int_{t_1}^{t_2} \left(\mathbf{F}_{rad} - \frac{2}{3}\frac{e^2}{c^3}\ddot{\mathbf{v}} \right) \cdot \mathbf{v} dt = 0. \tag{2.4}$$

In this way, the radiation reaction force is written as

$$\mathbf{F}_{rad} = \frac{2}{3}\frac{e^2}{c^3}\ddot{\mathbf{v}} \tag{2.5}$$

while the equation of motion can be reduced to

$$m\left(\dot{\mathbf{v}} - \frac{2e^2}{3mc^3}\ddot{\mathbf{v}} \right) = \mathbf{F}_{ext}. \tag{2.6}$$

The new equation of motion contains second time derivative of the velocity. In the absence of external field, the solution reads

$$\dot{\mathbf{v}}(t) = \mathbf{a}e^{t/\tau_0} \tag{2.7}$$

where

$$\tau_0 = \frac{2e^2}{3mc^3} = 6.4 \times 10^{-24} s. \tag{2.8}$$

This solution is unphysical because the electron is accelerated to extremely high velocities in a very short time. Such physical inconsistent solution is usually termed as "runaway" solution.

In order to generalize the equation of motion including the radiation reaction force to the relativistic case, we may make the replacement $\mathbf{v} \longrightarrow v^\mu$ as four-vector generalization. Furthermore, the relativistic generalization of Eq. (2.6) has to be Lorentz invariant so that the time t is replaced by proper time τ. The relativistic equation takes the form

$$\frac{dv^\mu}{d\tau} = \frac{e}{mc} F^{\mu\nu} v_\nu + \tau_0 \ddot{v}^\mu. \tag{2.9}$$

However, Eq. (2.9) does not satisfy the constraint $v^\mu v_\mu = c^2$ such that $d\left(v^\mu v_\mu\right)/d\tau = 0$. Eq. (2.9) should be modified by adding the extra term $\tau_0 v^\mu \dot{v}^\mu \dot{v}_\mu / c^2$ which can be neglected in the non-relativistic limit shown in Eq. (2.2) so that Eq. (2.9) is in Lorentz invariant form. The equation becomes

$$\frac{dv^\mu}{d\tau} = \frac{e}{mc} F^{\mu\nu} v_\nu + \Gamma^\mu \tag{2.10}$$

where

$$\Gamma^\mu = \tau_0 \left(\ddot{v}^\mu + v^\mu \dot{v}^\mu \dot{v}_\mu / c^2\right). \tag{2.11}$$

The first and second term in Eq. (2.11) correspond to the Schott term and radiation damping term respectively. Eq. (2.11) is known as Abraham four vector. It is neither radiation reaction nor external force as the Schott term differs from the negative of emission rate. However, the relativistic form of the equation of motion doesn't avoid the runway solution due to the Schott term.

In 1938, Dirac suggested to start from the coupled Maxwell and Lorentz equations

in order to solve the problem of a radiating electron self-consistently:

$$\begin{aligned} \partial_\mu F_T^{\mu\nu} &= -\frac{4\pi}{c} J^\nu \\ \partial_\lambda F_{T,\mu\nu} + \partial_\mu F_{,T\nu\lambda} + \partial_\nu F_{T,\lambda\mu} &= 0 \\ m_0 \frac{dv^\mu}{d\tau} &= e F_T^{\mu\nu} v_\nu \end{aligned} \tag{2.12}$$

where $F_T^{\mu\nu} = F_{ext}^{\mu\nu} + F_{ret}^{\mu\nu}$, with $F_{ext}^{\mu\nu}$ being the external/incident electromagnetic field, $F_{ret}^{\mu\nu}$ being the field of the moving electron, while m_0 is the bare electron mass and $J^\nu(x) = ec \int d\tau \delta[x - x(\tau)] v^\nu$ is the current. In the work by Dirac [16], the field of a moving charge is taken as both retarded and advanced field. In the later work by Rohrlich [28] it is found that the advanced field is not necessary for the derivation of radiation reaction force. The physical interpretation of the Schott term arises when the retarded field is separated into two parts [29].

The field of a moving charge is determined by the retarded Liénard-Wiechert solution of the Maxwell equations

$$\begin{aligned} F_{ret}^{\mu\nu} &= \frac{e}{\rho^2 c} \left(v^\mu u^\nu - v^\nu u^\mu \right) \\ &\quad + \frac{e}{\rho c^2} \left[\left(a^\mu v^\nu - a^\nu v^\mu \right) / c - u^\mu \left(\frac{v^\nu}{c} a^\mu u_\mu + a^\nu \right) + u^\nu \left(\frac{v^\mu}{c} a^\mu u_\mu + a^\mu \right) \right] \end{aligned} \tag{2.13}$$

where ρ is the distance between retarded point and field point in the instantaneous rest frame of the charge at the retarded time and u_μ is spacelike unit vector. The field Eq. (2.13) can be decomposed into two parts

$$F_{ret}^{\mu\nu} = F_I^{\mu\nu} + F_{II}^{\mu\nu} \tag{2.14}$$

where $F_I^{\mu\nu}$ and $F_{II}^{\mu\nu}$ correspond to the first term and second term of Eq. (2.13) respectively. The first term $F_I^{\mu\nu}$ is called velocity field and is essentially the static field as it is proportional to ρ^{-2}, whereas the second term $F_{II}^{\mu\nu}$ is called acceleration field as it

depends on acceleration. The second term is also called radiation field. Next, the energy-momentum tensor can be evaluated as

$$\begin{aligned} T^{\mu\nu} &= \frac{1}{4\pi}\left(F^{\mu\alpha}F^{\nu}_{\alpha} + \frac{1}{4}\eta^{\mu\nu}F_{\alpha\beta}F^{\alpha\beta}\right) \\ &= T^{\mu\nu}_{I,I} + T^{\mu\nu}_{I,II} + T^{\mu\nu}_{II,II}. \end{aligned} \tag{2.15}$$

The physical meaning of these tensors arises by evaluating their divergence. The divergence of the tensor $T^{\mu\nu}$ is

$$\partial_\mu T^{\mu\nu} = \frac{1}{4\pi}F^{\beta\nu}\partial_\alpha F^{\alpha}_{\beta} \tag{2.16}$$

and we obtain

$$\partial_\mu T^{\mu\nu}_{I,I} = -\frac{e^2}{2\pi\rho^5}a^\mu u_\mu R^\nu \tag{2.17}$$

$$\partial_\mu T^{\mu\nu}_{II,II} = 0 \tag{2.18}$$

$$\partial_\mu\left(T^{\mu\nu}_{I,I} + T^{\mu\nu}_{I,II} + T^{\mu\nu}_{II,II}\right) = 0. \tag{2.19}$$

where $R^\mu \equiv x^\mu - z^\mu(\tau)$ and $\rho = u_\mu R_\mu$.

For a charged particle moving with constant velocity, the momentum of the charged particle contains the bare momentum and the contribution from the Coulomb field. When the charged particle is in acceleration, the contribution of acceleration to the momentum is taken into account. The energy-momentum tensor, $T^{\mu\nu}_{I,I} + T^{\mu\nu}_{I,II}$ corresponds to the four-momentum of an accelerating particle while $T^{\mu\nu}_{II,II}$ corresponds to the radiated four-momentum. The electromagnetic field contribution to the momentum is equal to $e^2 v^\mu / 2c^2\epsilon$. The momentum contribution from the acceleration and electromagnetic field is

$$P^\mu_{I,I:I,II}(\tau) = \left(\frac{e^2}{2c^2\epsilon}\right)v^\mu - \frac{2}{3}\frac{e^2}{mc^3}a^\mu \tag{2.20}$$

where the limit $\epsilon \to 0$ is to be taken. The second term of Eq. (2.20) is recognized as the

Schott term. The total momentum is then

$$\begin{aligned} p^{\mu} &= p^{\mu}_{bare} + P^{\mu}_{I,I:I,II} \\ &= \left(m_0 + \frac{e^2}{2c^2\epsilon}\right) v^{\mu} - \frac{2}{3}\frac{e^2}{mc^3} a^{\mu} \end{aligned} \tag{2.21}$$

where $p^{\mu}_{bare} = m_0 v^{\mu}$.

When the acceleration of the charged particle is zero, the term $\frac{e^2 v^{\mu}}{2c^2\epsilon}$ is added to $m_0 v^{\mu}$. If we assume the electron as a uniformly charged sphere of radius ϵ the quantity $\frac{e^2}{2c^2\epsilon}$ is divergent in the limit $\epsilon \to 0$ (of a point charge). Therefore, in order to handle the divergence, $\frac{e^2}{2c^2\epsilon}$ is grouped into m ($m = m_0 + \frac{e^2}{2c^2\epsilon}$) to form the physical charged particle mass which is usually observed. This is sort of "classical renormalization" concept.

Furthermore, by including the radiated four-momentum with the present of external force

$$\frac{dp^{\mu}}{d\tau} + \frac{dP^{\mu}_{II,II}}{d\tau} = F^{\mu}_{ext} \tag{2.22}$$

one finds

$$ma^{\mu} = F^{\mu}_{ext} + \tau_0 \left(\dot{a}^{\mu} - a^2 v^{\mu}\right) \tag{2.23}$$

which is the Lorentz-Abraham-Dirac (LAD) equation. The LAD equation also did not avoid the runaway solution.

2.2 Landau-Lifshitz Model

There were plenty of models proposed for the avoidance of runway solution in LAD equation. One of the standard ways was introduced by Landau and Lifshitz [17]. In the instantaneous rest frame of the electron, the radiation reaction force is much smaller than the Lorentz force. This permits the substitution $dv^{\mu}/d\tau \to e/mcF^{\mu\nu}v_{\nu}$ into the LAD

equation. On the other hand, this also corresponds to first-order perturbation expansion to the electron four velocity $v^\mu = v_0^\mu + \tau_0 v_1^\mu + \mathcal{O}(\tau_0^2)$ [18]. The resulting equation is Landau-Liftshitz (LL) equation

$$\frac{dv^\mu}{d\tau} = \frac{e}{mc}F^{\mu\nu}v_\nu + \tau_0\left(\frac{e}{mc}\dot{F}^{\mu\nu}v_\nu + \frac{e^2}{m^2c^2}F^{\mu\nu}F_{\alpha\nu}v^\alpha + \frac{e^2}{m^2c^2}(F^{\alpha\nu}v_\nu)(F_{\alpha\lambda}v^\lambda)v^\mu\right). \tag{2.24}$$

In the LL equation, electron acceleration is zero when the electromagnetic field is turned off and the runaway solution is avoided. The LL equation can be reduced to the 3-dimensional form which is convenient for computational simulation. The 3-dimensional LL equation reads

$$\begin{aligned}\frac{d\gamma\beta}{dt} &= \frac{e}{mc}\left(\mathbf{E}+\beta\times\mathbf{B}\right) - \frac{2e^2}{3mc^2}\mathbf{g}^0 \\ \mathbf{g}^0 &= \frac{e}{mc^2}\gamma\left(\frac{\partial}{\partial t}+\mathbf{v}\cdot\nabla\right)\left(\mathbf{E}+\beta\times\mathbf{B}\right) + \left(\frac{e}{mc^2}\right)^2 c\left[\left(\beta\cdot\mathbf{E}\right)\mathbf{E}+\left(\mathbf{E}+\beta\times\mathbf{B}\right)\times\mathbf{B}\right] \\ &\quad - \left(\frac{e}{mc^2}\right)^2\gamma^2 c\beta\left[\left(\mathbf{E}+\beta\times\mathbf{B}\right)^2 - \left(\beta\cdot\mathbf{E}\right)^2\right].\end{aligned} \tag{2.25}$$

2.3 Sokolov Model

The LL equation is not the only model proposed to overcome the unphysical solution of LAD equation. There are many models discussed in Ref. [18]. The question of energy conservation in the Landau-Lifshitz equation was raised by Sokolov [22, 30, 31]. He pointed out that the Landau-Lifshitz equation conserves neither the generalized momentum of electron nor the total energy-momentum of the system. The dynamics of radiating electron begins with the equations,

$$\dot{p}^\mu = \frac{e}{c}F^{\mu\nu}\dot{x}_\nu - (\dot{p})^\mu_{rad}, \quad \dot{x}^\mu = m^{-1}p^\mu + (\dot{x})^\mu_{rad} \tag{2.26}$$

where $(\dot{p})^{\mu}_{rad}$ and $(\dot{x})^{\mu}_{rad}$ are to be determined. The second equation indicates that the four-velocity is not collinear to the four-momentum for an accelerated charged particle. This fact arises when we obtain the total momentum of an accelerating electron with renormalized mass in Eq. (2.21). The identities $\dot{x}^2 = c^2$ and $p^2 = m^2c^2$ cannot be satisfied simultaneously by Eq. (2.26). If one chooses to satisfy identity $\dot{x}^2 = c^2$ and by assuming the dipole radiation, we obtain

$$(\dot{p})^{\mu}_{rad} = -\frac{m\tau_0\ddot{x}^2}{c^2}\dot{x}^{\mu}, \quad (\dot{x})^{\mu}_{rad} = \tau_0\ddot{x}^{\mu}. \tag{2.27}$$

The combination of Eq. (2.26) and Eq. (2.27) gives LAD equation. The total energy becomes $E^2/c^2 = \mathbf{p}^2 + m^2(c^2 + \tau_0^2\ddot{x}^2)$ where m is the electron rest mass and $\ddot{x}^2 < 0$. The satisfaction of identity $\dot{x}^2 = c^2$ by Eq. (2.26) leads to the decreases of electron invariant mass. The rest mass energy of the electron can eventually vanishes into radiation which violate the energy-momentum conservation law.

Instead, in order to satisfy the energy-momentum conservation or the identity $p^2 = m^2c^2$, which is possible with the following choice [31]:

$$(\dot{p})^{\mu}_{rad} = \frac{I_{QED}}{mc^2}p^{\mu}, \quad (\dot{x})^{\mu}_{rad} = \frac{\tau_0}{m}\frac{I_{QED}}{I_E}f^{\mu}_L \tag{2.28}$$

where f^{μ}_L is given in Eq. (1.6) and

$$I_{QED} = \int_{\omega_{min}}^{\infty} \hbar\omega \frac{dW}{d\tau d\omega} d\omega \tag{2.29}$$

is the quantum emission intensity, $I_E = -\tau_0 f_L^2/m$ is the dipole emission intensity and $f_L = \frac{e}{mc}F^{\mu\nu}v_{\nu}$ being the Lorentz force. The resulting equations of motion are

$$\frac{dp^{\mu}}{d\tau} = \frac{e}{mc}F^{\mu\nu}\dot{x}_{\nu} - \frac{I_{QED}}{mc^2}p^{\mu} \tag{2.30}$$

$$\dot{x}^{\mu} = m^{-1}p^{\mu} + \frac{\tau_0}{m}\frac{I_{QED}}{I_E}f^{\mu}_L. \tag{2.31}$$

The velocity of an accelerated electron now contains an additional term. In the frame

where the electron momentum is zero, $\mathbf{p} = 0$, the velocity of the electron does not vanish where $\dot{\mathbf{x}} = \tau_0 e\mathbf{E}/m$. This indicates that extra work is done to compensate the energy loss. The non-vanishing of electron velocity leads to the impossibility to have an instantaneous rest frame for a radiating particle and the concept of proper time changed [32]. For a free particle, the worldline is parameterized by proper time and the identities $p^2 = m^2c^2$ and $\dot{x}^2 = c^2$ satisfied simultaneously. However, for a radiating charged particle, the worldline is not parameterized by the proper time. Instead, it would be the time measured in the frame where the spatial momentum is zero [33]. In other words, the violation of the identity $\dot{x}^2 = c^2$ implies the breaking of Lorentz invariance. The identity $\dot{x}^2 = c^2$ is violate by a term proportional to χ:

$$\dot{x}^2 = c^2\left(1 - \frac{\chi^2}{137^2}\right). \tag{2.32}$$

The violation of the Lorentz invariance is less than 1 % for $\chi < 13$. Therefore, we can assume the Lorentz invariance is preserved below this limit. The model proposed by Sokolov is still subject to controversy and debate [34]. Nevertheless, Sokolov model has an advantage in numerical computation as compared to LL equation in Eq. (2.25) where the time derivative of the field is avoided. For instance, in classical limit, $I_E = I_{QED}$, the three vector formulation is written as [22]

$$\frac{d\mathbf{p}}{dt} = \mathbf{f_{Le}} + \frac{e}{c}[\bar{\mathbf{u}} \times \mathbf{B}] - \frac{\mathbf{u}\mathcal{E}^2}{m^2c^6}(\bar{\mathbf{u}} \cdot \mathbf{f_{Le}}) \tag{2.33}$$

$$\frac{d\mathbf{x}}{dt} = \mathbf{u} + \bar{\mathbf{u}}, \quad \bar{\mathbf{u}} = \frac{\tau_0}{m}\frac{\mathbf{f_{Le}} - \mathbf{u}(\mathbf{u} \cdot \mathbf{f_{Le}})/c^2}{1 + \tau_0(\mathbf{u} \cdot \mathbf{f_{Le}})/(mc^2)} \tag{2.34}$$

$$\frac{\mathcal{E}}{mc^2} = \sqrt{1 + \left(\frac{\mathbf{p}}{mc}\right)^2}, \quad \mathbf{u} = \frac{c^2\mathbf{p}}{\mathcal{E}}, \tag{2.35}$$

where $\bar{\mathbf{u}}$ being the back-reaction effect of electron velocity. The energy equation is written as

$$\frac{d\mathcal{E}}{dt} = e(\mathbf{u} + \bar{\mathbf{u}}) \cdot \mathbf{E} - \frac{\mathcal{E}^2}{m^2c^4}(\bar{\mathbf{u}} \cdot \mathbf{f_{Le}}). \tag{2.36}$$

2.4 Classical radiation-dominated regime

The radiation reaction (RR) force on the charged particle is much weaker than Lorentz force in non-relativistic limit and it is also small in instantaneous rest frame of the charged particle for the case of relativistic limit, if the wavelength λ and the external field amplitude E satisfy $\lambda >> \alpha\lambda_C$ and $E << E_S/\alpha$ where E_S is the Schwinger limit (see Eq. (1.3)). However, there is a regime in the ultrarelativistic case where the RR force is comparable to the Lorentz force in laboratory frame while much weaker in the instantaneous rest frame of the charged particle. This regime is so-called classical radiation-dominated regime (CRDR) where the quantum effect is neglected ($\chi << 1$). This regime was investigated by many authors and being discussed in detail in Ref. [5]. The definition of CRDR in the background laser field is defined as a significant comparison of average energy loss by the electron in one laser period to the initial kinetic energy of electron [21]. A. Di Piazza [13, 35] obtained the parameter, R_C that determine the condition for CRDR for a counterpropagating electron with respect to laser field by solving the LL equation and is written as

$$R_C = \frac{2}{3}\alpha\frac{\hbar\omega_0}{mc^2}\gamma_0 a_0^2(1+\beta_x) \tag{2.37}$$

where γ_0 is initial gamma factor and $\beta_x = \sqrt{\gamma_0^2 - 1}/\gamma_0$. This parameter determine the strength of RR. The effects of RR are strong if $R_C \gtrsim 1$ and negligible if $R_C << 1$.

The same condition can be obtained by using the same method for Sokolov's model: the equation of motion is multiplied by the laser wave vector k_0. The major term that contributes to RR is the last term of Eq. (2.31). By setting $I_{QED} = I_E = \tau_0(k_0 \cdot p)^2 c^2 a_0^2 |d\psi/d\xi|^2$ where $\xi = k_0 \cdot x$ and ψ is an arbitrary scalar function of ξ, we obtain

$$(k_0 \cdot p) = \frac{(k_0 \cdot p)|_{\xi=0}}{1 + R_C \int_0^\xi |\frac{d\psi}{d\xi}|^2 d\xi}. \tag{2.38}$$

The term $(k_0 \cdot p)$ is proportional to the electron kinetic energy. When $R_C >> 1$, the kinetic energy of electron reduces and being converted into radiation energy. When $R_C << 1$, there is no significant energy conversion from the kinetic energy of electron into radiation energy. However, there will be a region where $R_C << 1$ while $\chi \sim 1$. For example, the a laser field of intensity $I = 10^{22}$ W/cm^2 ($a_0 = 85$) and wavelength $\lambda = 1$ μm ($\hbar\omega_0 = 1.23$ eV, $T = 3fs$ [one laser period]) counterpropagating with 1 GeV ($\gamma_0 \approx 1957$, $\beta_x \approx 1$) electron is

$$R_C \approx 0.33, \quad \chi \approx 0.8. \tag{2.39}$$

In this case, the effects of RR are insignificant, but the quantum effect is not negligible at $\chi \approx 0.8$. The quantum effects will modify the radiation emission spectrum instead of the effects of RR.

2.5 Moderate quantum regime

At $\chi \sim 1$, emitted radiation carries away a large amount of the electron energy. In this situation, the change in momentum of the electron is discontinuous and the classical equation of motion fails [36]. This effect is often referred as electron recoil or quantum recoil. The quantum recoil can be explained in the context of photon rather than the classical field for an emitting radiation. However, if we can obtain a correct description of radiation emission in this regime, the correction to the classical trajectory can provide an acceptable approximation to the quantum processes. Besides, the classical approach of the radiation emission overestimates the total radiated power when χ approach unity. The electron can emit radiation more than its own energy and do not conserve energy. When treated quantum mechanically, the maximum emitted photon energy is limited by the electron energy [7, 37, 38]. The quantum correction to classical equation is not included in the LL equation. However, quantum modification is included in Sokolov model and represented by I_{QED} in Eq. (2.31). To include quantum effects, the following substitution is made on

the second equation of Eq. (2.34) [30]:

$$\tau_0 \longrightarrow \tau_0 \frac{I_{QED}}{I_E}. \tag{2.40}$$

The expression I_{QED} can be expressed by the probability rate of photon emission [39, 40]

$$\begin{aligned} dW_{em} &= \frac{\alpha mc^2}{\sqrt{3}\pi\hbar\gamma}\left[\left(1-\xi+\frac{1}{1-\xi}\right)K_{2/3}(\delta)\right. \\ &\left. -\int_{\delta}^{\infty} K_{1/3}(s)ds\right]d\xi \end{aligned} \tag{2.41}$$

where

$$\xi = \frac{\hbar\omega}{\gamma mc^2},\ \delta = \frac{2\xi}{3(1-\xi)\chi} \tag{2.42}$$

and $K_\nu(x)$ is modified Bessel function. The parameter ξ ensures that electron cannot emit photon with energy larger than its own. At classical limit $\chi << 1$, the quantum emission is reduced to classical synchrotron radiation

$$\begin{aligned} dP &= \mathcal{E}dW_{em} \\ &\rightarrow \frac{e^2\omega_c}{\sqrt{3}\pi c}\frac{1}{\gamma^2}\frac{\omega}{\omega_c}[2K_{2/3}(\delta) - \int_{\delta}^{\infty} K_{1/3}(s)ds]d\omega \end{aligned}$$

where P is the power radiated, ω_c is the critical frequency and $\delta \longrightarrow 2\xi/3\chi$. When integrated with respect to the emitted photon frequency, one obtains the expression I_E (see Eq. (9) - (19) in Ref. [30]).

Fig. 2.1 shows the log-linear plot of the photon number distribution for 1 GeV single electron backscattered from 83 fs laser pulse of intensity $I = 10^{22}$ W/cm^2 by Sokolov model with and without quantum correction. The classical limit is where $I_{QED} = I_E$ being taken and it reduces to the LL equation. There is a clear distinction between quantum case and the classical case for high photon energy production. One would observe the suppression of high energy photon production in the experiment according to the quantum description. Although the production of high energy photon is small for a single electron, it will be significant for an electron beam. We can obtain the total emission energy by in-

tegrating the area under the curve. Therefore, the inclusion of quantum recoil is necessary to avoid the overestimation of conversion efficiency. Since LL equation does not contain the term with quantum correction, the equation of motion suggested by Sokolov will be implemented.

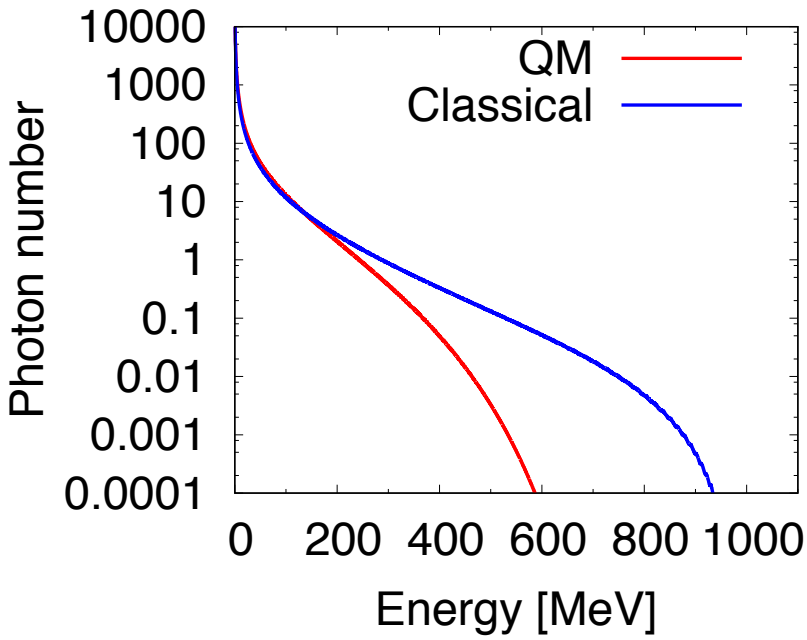

Figure 2.1: Photon number distribution for 1 GeV electron backscattered from 83 fs laser pulse of intensity $I = 10^{22}$ W/cm^2 by Sokolov model with (red line) and without (blue line) quantum correction. The classical limit is where $I_{QED} = I_E$ being taken. A clear distinction between quantum case and classical case at high photon energy is observed.

As $\chi \approx 1$, the creation of electron-positron pair from emitted hard photons by interacting with the same laser field may occur. This process is called the Breit-Wheeler process [41]. Unlike the radiation emission process, the Breit-Wheeler process is a threshold process. In order to create a pair with an optical laser with photon energy on the order of 1 eV, the energy of the counterpropagating photon should be at least 250 GeV. In strong laser field, $a_0 >> 1$, multi-photon process or non-linear Breit-Wheeler process may help in the pair creation. For 1 keV photon, around 10^6 optical laser photons are required to reach the threshold energy. However, the effective mass of electron and positron in strong laser field is $m_* = m\sqrt{1 + a_0^2/2}$ which leads to the up-shift of the threshold energy. Besides, the cross section $\sigma_{pair} \propto \exp(-8/3\chi_\gamma)$ where $\chi_\gamma = \chi\hbar\omega/\gamma_0 mc^2$ for counter-propagating photons with respect to the EM field [42]. For the condition in Eq. (2.39),

$\chi_\gamma << 1$ and the probability for pair production is suppressed. It was also mentioned that the pair could be created at the laser intensity of 10^{24} W/cm^2 with two counterpropagating circularly polarized laser beam.

We will work at initial kinetic energy of electron in the range of 10 MeV - 1 GeV which is within the current achievable electron beam energy by laser wakefield acceleration, [43] the availability of 600 MeV accelerator facilities at ELI [44] and maximum total energy of 40 MeV electron beam with bunch charge up to 1 nC from Electron Linac of high Brilliance and low Emittance (ELBE) at the Helmholtz-Zentrum Dresden-Rossendorf (HZDR) [45]. The pair production is assumed to be negligible in the process considered.

2.6 Ponderomotive Force

Apart from the effects of radiation reaction and quantum effects, the ponderomotive force also plays a crucial role in the interaction of the electron with the intense laser field particularly a short pulse laser. The ponderomotive force is a second order force for a charged particle moving in a spatially inhomogeneous oscillating external field. The first order force being the force for a charged particle moving in a spatially homogeneous oscillating external field. The derivation of the ponderomotive force can be obtained if the trajectory of the charged particle is treated as a perturbation such that $x = x_0 + x_1 + x_2$ where x_0 is the initial position of the charged particle and x_1 and x_2 are the first order and second order solution respectively. A crucial assumption for this solution is that the spatial variation of the field is much larger than the wavelength of the oscillating field. By assuming an external electric field in one dimension

$$E(x,t) = E(x)\cos(\omega_0 t) \tag{2.43}$$

where ω_0 is the angular frequency of the oscillating field and $E(x)$ vary slowly around its initial position, the first order solution can be written as

$$m\frac{d\dot{x}_1}{dt} = eE(x_0)\cos(\omega_0 t) \tag{2.44}$$

$$\dot{x}_1 = \frac{e}{m\omega}E(x_0)\sin(\omega_0 t) \tag{2.45}$$

$$\delta x_1 = -\frac{e}{m\omega^2}E(x_0)\cos(\omega_0 t). \tag{2.46}$$

This is the solution for a charged particle in uniform oscillating field. If the electric field is expanded around its initial position by means of Taylor expansion to the first order

$$E(x) = E(x_0) + \delta x_1 \frac{d}{dx}E(x). \tag{2.47}$$

the second order equation of motion is written as

$$m\frac{d\dot{x}_2}{dt} = e\delta x_1 \frac{d}{dx}E(x_0)\cos(\omega_0 t). \tag{2.48}$$

Substituting Eq. (2.46) into Eq. (2.48), one obtains

$$m\frac{d\dot{x}_2}{dt} = -\frac{e^2}{m^2\omega_0^2}E(x_0)\frac{d}{dx}E(x_0)\cos^2(\omega_0 t). \tag{2.49}$$

Averaging the time oscillating term over one period the equation of motion takes the form

$$F_p = -\frac{e^2}{4m\omega_0^2}\frac{d}{dx}E^2(x_0). \tag{2.50}$$

Eq. (2.50) is called the ponderomotive force which is proportional to the gradient of electric field square. When this force is strong, the charged particle tend to move into regions of diminishing field strength. The direction of the motion is independent of the sign of the charged particle. For a three-dimensional system including the magnetic field, the ponderomotive force can be obtained by using the Faraday's law $c\nabla \times \mathbf{E}(\mathbf{x}) = -\omega\mathbf{B}(\mathbf{x})$.

The resulting equation is

$$F_p = -\nabla\Phi_p \tag{2.51}$$

where

$$\begin{aligned}\Phi_p &= \frac{e^2}{2m\omega_0^2} < E^2(x_0) > \\ &= \frac{m}{2} < \dot{x}_1^2 > .\end{aligned} \tag{2.52}$$

is the ponderomotive potential. Eq. (2.51) can also be interpreted as the minus gradient of the average oscillating energy. For a relativistic particle travel in an external field, their kinetic energy is $mc^2(\gamma - 1) \simeq mc^2(\sqrt{1+\mathbf{a}^2} - 1)$ where $\mathbf{a} = e\mathbf{A}/mc^2$. By taking the minus gradient of the average energy, the ponderomotive force in relativistic form is written as

$$\begin{aligned}F_p &= -mc^2\nabla(\sqrt{1+ < \mathbf{a}^2 >}) \\ &= -\nabla m_{eff}c^2\end{aligned} \tag{2.53}$$

where $m_{eff} = m\sqrt{1+ < \mathbf{a}^2 >}$ being the effective mass of a charged particle in an external field. A more detail information about the ponderomotive force can be found in Ref. [46, 47].

Chapter 3

Numerical Scheme for Single Electron

In this chapter, we describe the numerical scheme to simulate the motion of an electron in the laser field. The motion of a radiating electron is governed by Sokolov equation. In order to verify the numerical scheme, we compare our simulation to a recent published experimental result. The trajectories, time evolution of electron energy, emission spectra, photon number distribution and photon angular distribution are presented. Different kinds of conversion efficiencies are introduced. These conversion efficiencies are then shown for various laser intensities and different pulse duration.

3.1 Algorithm implementation

We followed part of the algorithm implemented by Ref. [30]. The equation of motion Eq. (2.33) is solved by using the standard leapfrog scheme. The position of the electron is normalized by the Larmor radius for the speed of light R_m and unit magnetic field $B' = 1$. The simulation variables are normalised as follows:

$$\begin{aligned}
\mathbf{x}' &\longrightarrow \frac{\mathbf{x}}{R_m},\ t' \longrightarrow \frac{ct}{R_m},\ \mathbf{p}' \longrightarrow \frac{\mathbf{p}}{mc},\ \gamma \longrightarrow \frac{E}{mc^2}, \\
\mathbf{u}' &\longrightarrow \frac{\mathbf{u}}{c},\ \mathbf{E}' \longrightarrow \frac{e\mathbf{E}R_m}{mc^2},\ \mathbf{B}' \longrightarrow \frac{e\mathbf{B}R_m}{mc}, \\
\mathbf{f}'_{Le} &= \frac{d\mathbf{p}'}{dt'} = \mathbf{E}' + \mathbf{u}' \times \mathbf{B}'.
\end{aligned}$$

3. NUMERICAL SCHEME FOR SINGLE ELECTRON

We should emphasize that we start the normalization of Lorentz force and Sokolov's equations in SI unit such that $|\mathbf{E}'| = |\mathbf{B}'| = 1$ and $|\mathbf{E}| = c|\mathbf{B}|$ for electromagnetic field in vacuum and the velocity is normalized by the speed of light. The particle is pushed forward in time via leap-frog Boris scheme (see Sec. 4.1.4). Energy and velocity of the electron are obtained. After that, the Lorentz force is recovered from the momentum. At this stage, the value χ is calculated for the used of emission process. The term $\bar{\mathbf{u}}$ is obtained from the Lorentz force and velocity. The RR force is then added to the momentum and velocity. Finally, the particle position is obtained. The procedures are listed as follows:

1. $\mathbf{p}'^{n+1/2} = \mathbf{p}'^{n-1/2} + \Delta t'\, \mathbf{f}'_{Le}(\mathbf{E}', \mathbf{B}')$

2. $\gamma^{n+1/2} = \sqrt{1 + (\mathbf{p}'^{n+1/2})^2}$
   $\mathbf{u}'^{n+1/2} = \mathbf{p}'^{n+1/2}/\gamma^{n+1/2}$

3. $\mathbf{f}'_{Le} = (\mathbf{p}'^{n+1/2} - \mathbf{p}'^{n-1/2})/\Delta t$

4. $\chi = \frac{3}{2}\frac{\tau'_0}{\alpha}\gamma\sqrt{(\mathbf{E}' + \mathbf{u}' \times \mathbf{B}')^2 - (\mathbf{E}' \cdot \mathbf{u}')^2}$

5. $\bar{\mathbf{u}}' = \tau'_0 \frac{\mathbf{f}'_{\mathbf{Le}} - \mathbf{u}'(\mathbf{u}' \cdot \mathbf{f}'_{\mathbf{Le}})}{1 + \tau'_0(\mathbf{u}' \cdot \mathbf{f}'_{\mathbf{Le}})}$

6. $\mathbf{p}'^{n+1/2} \longrightarrow \mathbf{p}'^{n+1/2} + \Delta t\{-[\bar{\mathbf{u}}' \times \mathbf{B}'] - \mathbf{u}'^{n+1/2}(\gamma^{n+1/2})^2(\mathbf{f}'_{\mathbf{Le}} \cdot \bar{\mathbf{u}}')\}$

7. $\mathbf{u}'^{n+1/2} = \mathbf{p}'^{n+1/2}/\sqrt{1 + (\mathbf{p}'^{n+1/2})^2} + \bar{\mathbf{u}}'$

8. $\mathbf{x}'^{n+1/2} = \mathbf{x}'^{n} + \mathbf{u}'^{n+1/2}\Delta t'$

The parameter χ determines the importance of QED effects. During the computation, the lower limit of χ is set to be 1×10^{-3}. Below this limit the motion of the electron is treated as classical. Above this limit, the motion of the electron is modified as Eq. (2.40) and I_E is taken as classical synchrotron emission intensity. In the calculation of emission spectrum, the probability of photon emission is negligible if χ is below this limit.

A logarithmic grid for $\chi_k = A_0 \exp[\alpha(k - 1.5)]$ and $k \in [1, 200]$ is introduced where $A_0 = 1 \times 10^{-3}$ and $\alpha = [\ln(1000) - \ln(0.001)]/199$ such that $\chi_{k=1} = 1 \times 10^{-3}$

and $\chi_{k=200} = 1 \times 10^3$. In order to assemble the emission, energy bin is introduced. The emission energy $\mathcal{E} = (\gamma^{n+1/2})^2(\mathbf{f}'_{\mathbf{Le}} \cdot \bar{\mathbf{u}}')\Delta t'$ is added into the suitable bin. The normalised emission spectrum is calculated as

$$\mathcal{E}_{rad,i,k} \longrightarrow \mathcal{E}_{rad,i,k} + \frac{\mathcal{E} dW_{em,i,k}}{W_{em,k}} \tag{3.1}$$

where i is a particular energy bin. The differential probability $dW_{em,i,k}$ depends on χ and $\mathcal{E}$ while total emission probability $W_{em,k}$ depends only on χ of each time step. Instead of calculating the differential probabilities and total probabilities at every time step, the data arrays of $W_{em,k}$ and $dW_{em,i,k}$ are prepared in advance. During the calculation process, the differential probability rate is obtained via interpolation at particular χ_k. The photon number distribution is obtained by dividing Eq. (3.1) with photon energy. In order to compute the angular distribution of emission, an angular grid for a polar angle is introduced such that $\theta_j = \cos^{-1}(-p_x/\sqrt{p_x^2 + p_y^2})$. The emission energy $\mathcal{E}$ is put into the proper angular grid. The photon number distribution is converted into observable results by multiplying the physical bin size and number of electrons. A bin size of 1 MeV is used throughout the simulation.

For the sake of comparison of the emission spectrum with RR and without RR, stage 5, 6 and 7 are not needed. The emission energy at each time step is obtained from total power emitted by an electron with the correction as in Eq. (2.40) [7]. The emission spectrum is then obtained from Eq. (3.1).

In the simulation code, the shape of the electron beam bunch may be considered by using representative points (electrons). These points are located two-dimensionally and uniformly around the center of the electron bunch. Then, the weight of each point is defined by

$$\begin{aligned} w_i &= \exp\left[\frac{-y_i^2 - z_i^2}{\sigma^2}\right] \\ weight_i &= \frac{w_i}{\Sigma_i w_i} \end{aligned} \tag{3.2}$$

according to the position of the point (y, z) where i is the number electrons. The dynamics of electrons is calculated for each point and the resulting emission spectrum is integrated by using weight to include the effect of finite beam size.

3.2 Comparison with experiment

In order to verify the feasibility of the numerical scheme, we compare our simulation result to a recently published experiment [20]. In the experiment, an electron beam is scattered from a laser pulse of wavelength $\lambda \approx 800$ nm and pulse duration of $\tau \approx (42 \pm 4)$ fs. In Fig. 3.1 (a), the measured laser intensity is shown with a sharp peak of $a_0 = 10$. Due to the small spatial extent of this sharp peak, there is only one in a hundred of the electrons effectively interacts in this region. Therefore, a peak at $a_0 = 2$ is used for numerical calculation. The laser pulse is assumed to be Gaussian with the width of ~ 100 μm. In Fig. 3.1(b), the electron spectrum with an average energy at 550 MeV is shown. The area under the spectrum indicated by the red line is taken to be the number of electrons in the bunch which contains about $N = 3.7 \times 10^8$ electrons. The diameter of the electron bunch is (30 ± 3) μm. The experimental results are shown in the green band in Fig. 3.2 (a). The effects of RR and quantum effects are assumed to be negligible in the simulation in Ref. [20] for $a_0 = 2$ and $a_0 = 1$. However, we included the effects of RR and quantum effects for $a_0 = 2$ in our simulation as shown in Fig. 3.2 (b). Our numerical scheme explains the experimental result at classical and small RR limit ($R_C \approx 1 \times 10^{-4}$, $\chi \approx 0.01$).

3.3 Dynamics of an electron in a laser pulse

In order to demonstrate the effects of RR in the interaction of a laser pulse with a counterpropagating ultrarelativistic electron, the setup shown in Fig. 3.3 is considered. A laser pulse which is linearly polarized in y direction and propagates in the $-x$ direction is

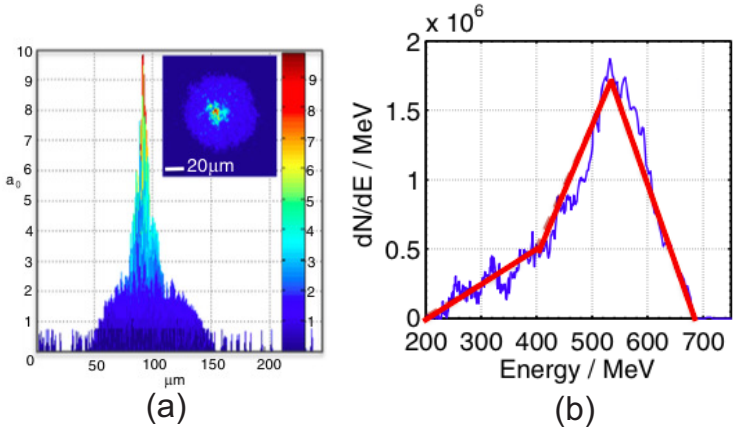

Figure 3.1: (a) Measured laser intensity for the scattering process . The laser profile was taken to be Gaussian with a peak at $a_0 = 2$. (b) The electron spectrum for scattering process. The area under the red line is estimated to be the number of electron. Reproduced with permission from G. Sarri *et al.*, Phys. Rev. Lett. 113, 224801 (2014). Copyright 2014 American Physical Society.

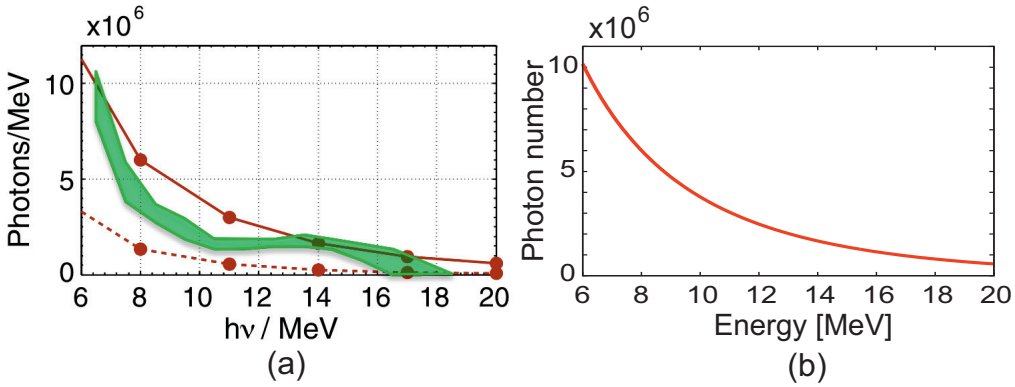

Figure 3.2: (a) The photon number distribution of the scattering process. The green band is the experimental results. The red line and red dashed line correspond to simulation results with $a_0 = 2$ and $a_0 = 1$ respectively. Reproduced with permission from G. Sarri *et al.*, Phys. Rev. Lett. 113, 224801 (2014). Copyright 2014 American Physical Society. (b) Our numerical result with RR and quantum effect included for $a_0 = 2$.

implemented, and the electric and magnetic field are expressed as

$$\begin{aligned} E_x &= E_z = 0 \\ E_y &= E_0 e^{-\frac{y^2+z^2}{\sigma_0^2}} e^{-\frac{(\omega_0 t - kx)^2}{(\omega_0 t_L)^2}} \sin(\omega_0 t - kx) \\ B_x &= B_y = 0 \\ B_z &= B_0 e^{-\frac{y^2+z^2}{\sigma_0^2}} e^{-\frac{(\omega_0 t - kx)^2}{(\omega_0 t_L)^2}} \sin(\omega_0 t - kx) \end{aligned} \tag{3.3}$$

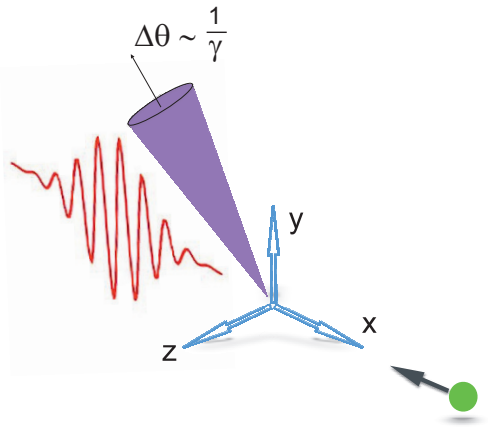

Figure 3.3: The setup of a laser pulse interacting with an ultrarelativistic electron.

where σ_0 is the laser waist radius, k is the laser wave vector and t_L is the laser pulse duration. The laser spot size is set to 2 μm. In this work, single electron travel along the laser beam axis is assumed. When the laser beam is focused to 2 μm the paraxial approximation or beyond paraxial approximation would be a more realistic laser pulse [48, 49]. At the vicinity of the laser beam axis, the paraxial approximation with the longitudinal electric and magnetic field components is sufficient for a laser beam with $\sigma_0 \geq 1.06\lambda$ [48]. Besides, it was shown that relativistic particle travel close to the beam axis does not experience a net acceleration by the electric field component along the trajectory of the particle [49]. Thus, it poses no serious modification to the radiation emission process. The amplitude of an oscillating electron in a laser field $y_0 \propto a_0\lambda/2\pi\gamma_0$. For $a_0 = 85, \gamma_0 = 100$ and $\lambda = 1$ μm, $y_0 \sim 0.14$ μm $<<$ 2 μm. Then the longitudinal component of the electric field is small compared to the transverse component such that $E_x/E_y \propto \xi\varepsilon \sim 2$ % where $\xi = y/\sigma_0$ and $\theta_0 = \lambda/\pi\sigma_0$ is the diffraction angle. Furthermore, the values of the Gouy phase change from 0 to $\pi/2$ as x changes from 0 to ∞ (see Sec. 4.2 and Ref. [50]). In this work, a pulsed laser beam is considered. At the edge of the pulse, the effect of Gouy phase is negligible as the field strength is small. Therefore, the approximation of Eq. (3.3) with $\sigma_0 = 2\lambda$ and $\lambda = 1$ μm provide an acceptable estimation for an electron moving along the laser beam axis.

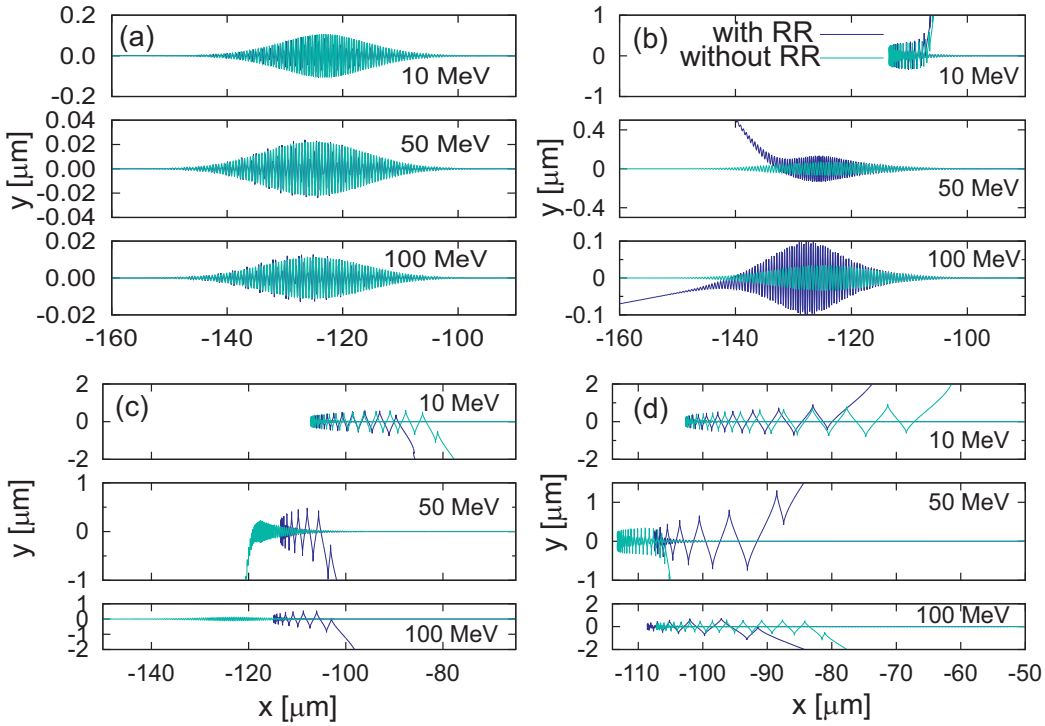

Figure 3.4: Electron trajectories with and without RR at (a)10^{21} W/cm^2, (b) 10^{22} W/cm^2, (c) 10^{23} W/cm^2 and (d) 10^{24} W/cm^2. The initial electron energies are 10 MeV, 50 MeV and 100 MeV. The amplitude of electron oscillation with RR is larger due to the decrease of Lorentz factor γ and the electron effective mass. In (a), $a_0 << \gamma_0$ the ponderomotive force is small and the electron passes through the laser; in (c) & (d), $a_0 >> \gamma_0$ the ponderomotive force is large and the electron changes its direction of motion.

3.3.1 Trajectories and time evolution of electron energy

Figure 3.4 shows the trajectories of the electron at different laser intensities with and without RR. The effects of RR are not significant at the laser intensity of the order of 10^{21} W/cm^2 as shown in Fig. 3.4 (a). As we increase one order of laser intensity, the effect of RR begins to appear. The amplitude of electron oscillation with RR is significantly larger as compared to the case without RR due to the decreasing of electron energy over time ($\gamma = \mathcal{E}/mc^2$, see Fig. 3.6 and Fig. 3.7). This in turn leads to the decreasing of electron effective mass. This is shown in Fig. 3.4 (b) for the case of 50 MeV and 100 MeV. The oscillation amplitude of the case of 100 MeV is almost two time larger for RR as compared to the case without RR due to the reason described above.

On the other hand, an electron interacting with the inhomogeneous oscillating electromagnetic field will experience the ponderomotive force. The electron tends to

move to the region of diminishing field amplitude as the ponderomotive force is proportional to the negative of the gradient of electric field square. If the field amplitude a_0 is large enough electron may reverse its trajectory. This is shown in Fig. 3.4 (b) for the case of 10 MeV and Fig. 3.4 (c) for the case of 10 MeV and 50 MeV. In the case of 100MeV with RR the electron is reflected by ponderomotive force, but the case without RR is seen to show the passing case. This depends on how much energy electron loses its kinetic energy during the interaction with the laser pulse. The final direction of the deflected electron (up or down) depends on its final position in the laser carrier envelope phase.

The regime that determines the passing thru and reflected case is generally categorised by the laser normalized amplitude, a_0 and initial Lorentz factor γ_0. For $a_0 << \gamma_0$ the ponderomotive force is small and the electron passes through the laser while $a_0 >> \gamma_0$ the ponderomotive force is large and the electron changes its direction of motion.

As shown in Fig. 3.5 (a), there is no difference between the initial energy and the final energy for the case without RR. When the effects of RR are included, the energy of electron decreases. Meanwhile in Fig. 3.5 (b), the electron first loses some amount of energy and then accelerated to higher energy for the case with RR. When the effects of RR are ignored, the electron is accelerated to the energy lower than the case of RR. In this work, the laser pulse with a spot size (waist radius) of 2 μm is used. When the electron is accelerated to very high energy, it escapes from the focused region. This explains the jump in electron energy at 240 fs in Fig. 3.5 (b) for the case of RR. The trajectory for the corresponding process is shown in Fig. 3.4 (d) for 100 MeV electron. The interval of the vertical scale is $[-2, 2]$ μm. The situation in Fig. 3.5 (a) corresponds to $a_0 << \gamma_0$ while in Fig. 3.5 (b) corresponds to $a_0 >> \gamma_0$. The intermediate situation $a_0 \sim \gamma_0$ is shown in Fig. 3.6 (c) where $a_0 = 268$ and $\gamma_0 \approx 200$ for 100 MeV electron. In this situation, the electron first lost energy and then accelerated to different final energy either lower or similar to its initial kinetic energy depends on its last position in the focused region.

In Fig. 3.6 (a), the time evolution of electron energy at the laser intensity of 10^{21} W/cm^2 is shown for electron initial energies of 10 MeV, 20 MeV, 30 MeV, 40 MeV, 50 MeV and 100 MeV. The same plots are shown in (b), (c) and (d) at the laser intensities

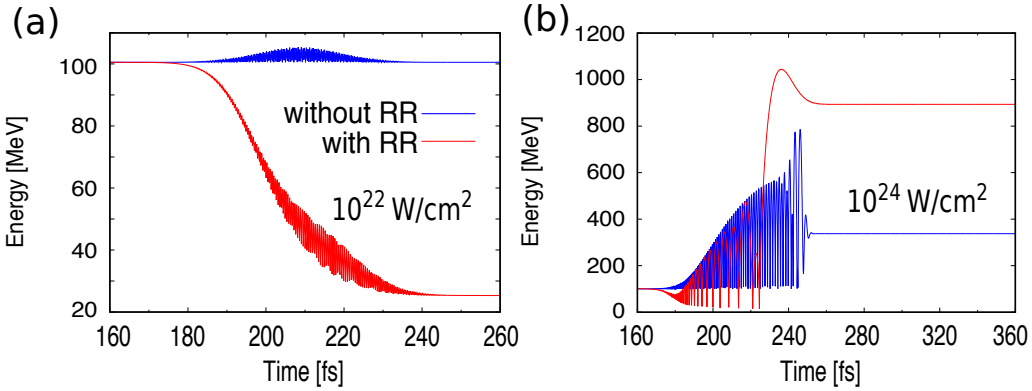

Figure 3.5: Comparison of the time evolution of electron energy at laser intensities (a) 10^{22} W/cm^2 and (b) 10^{24} W/cm^2 for case with RR (red line) and without RR (blue). The initial energy of electron for at both intensities is 100 MeV. The situation in (a) corresponds to the condition where $a_0 << \gamma_0$ while in (b) corresponds to the condition where $a_0 >> \gamma_0$.

of 10^{22} W/cm^2, 10^{23} W/cm^2 and 10^{24} W/cm^2 respectively. An electron with initial energy of 100 MeV propagates and loses its energy when interacting with the laser pulse at 10^{21} W/cm^2 at 190 fs. The electron settles down to lower energy after leaving the laser pulse as shown in Fig. 3.6 (a). However, for the case of 10 MeV to 50 MeV electron does not show significant energy losses.

When laser intensity is increased in one order of magnitude to 10^{22} W/cm^2, electron with initial energies 30 MeV, 40 MeV, 50 MeV and 100 MeV shows a pattern of energy loss where 100 MeV being the strongest as shown in Fig. 3.6 (b). Meanwhile, the electron with an initial energy of 10 MeV interacts with the laser pulse at 180 fs gains energy and is accelerated to higher energy. These results correspond to the trajectories shown in Fig. 3.4 (b) and the reasons explained there.

If the laser intensity is further increased to 10^{23} W/cm^2 as shown in Fig. 3.6 (c), the electron first loses some energy when interacting with the laser pulse. Then the electron is accelerated to higher energy in the case of 100 MeV. For other cases, electrons gain energy directly from the laser pulse. Similar results are observed at the laser intensity of 10^{24} W/cm^2 for all energies as shown in Fig. 3.6 (d).

Similar plot is shown in Fig. 3.7 for the cases of 200 MeV, 400 MeV, 600 MeV, 800 MeV and 1000 MeV. At the laser intensity of 10^{21} W/cm^2 in Fig. 3.7 (a), the electrons show the pattern of energy loss for all cases and settle down to different final energies. On

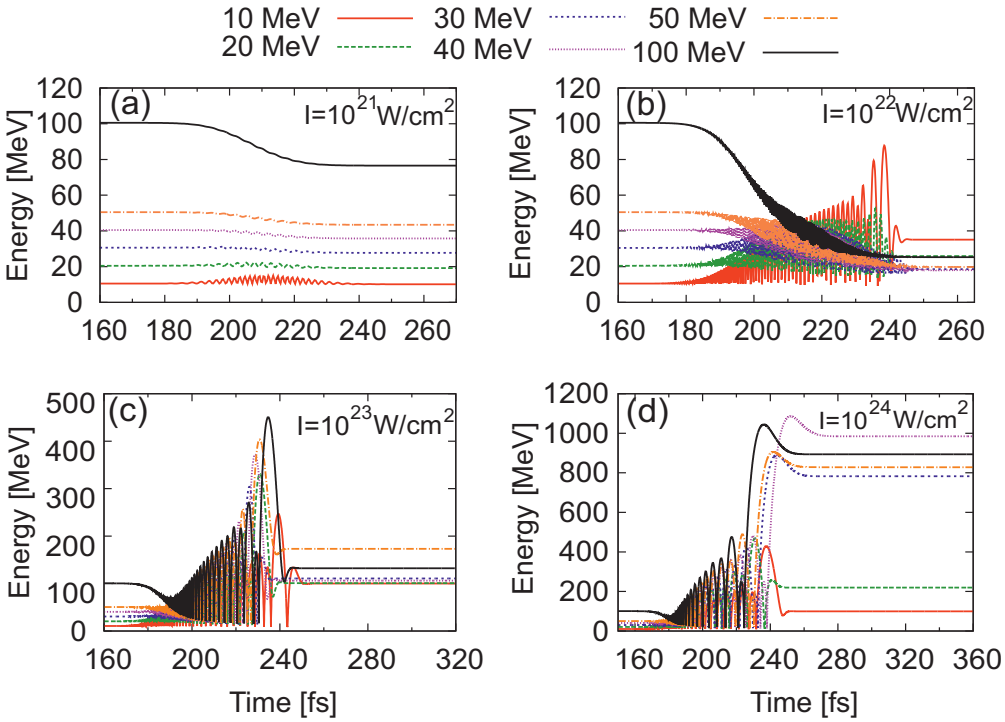

Figure 3.6: The time evolution of electron energy at different laser intensities are shown with the effects of RR included. The electron initial energies are 10 MeV, 20 MeV, 30 MeV, 40 MeV, 50 MeV and 100 MeV.

the other hand, the electrons lose their energy and come to the same final energy (i.e. 30 MeV) for intensity 10^{22} W/cm^2 as shown in Fig. 3.7 (b). The similar pattern also occur in Fig. 3.7 (c) and (d) at the laser intensity of 10^{23} W/cm^2 and 10^{24} W/cm^2 where the electrons energies converge to the same point around 180-190 fs. It is unclear what is the reason for this behaviour; however, quantum effects are expected to responsible for this behaviour. A further study on this behaviour should be carried out in the future.

The situation in Fig. 3.7 (c) at 10^{23} W/cm^2 is similar to the case of 100 MeV in Fig. 3.6 (c) except that the electron does not gain energy higher than its initial energy. Meanwhile, at the laser intensity of 10^{24} W/cm^2 in Fig. 3.6 (d) the electrons gain energy higher than its own except for the case of 400 MeV. The final energy of the electron is dependent on the laser spot size.

3.3.2 Emission spectra for long and short laser pulse duration

When a relativistic electron moves in the laser field, high energy radiation is emitted in the direction of electron momentum. The emission spectra of electrons with initial

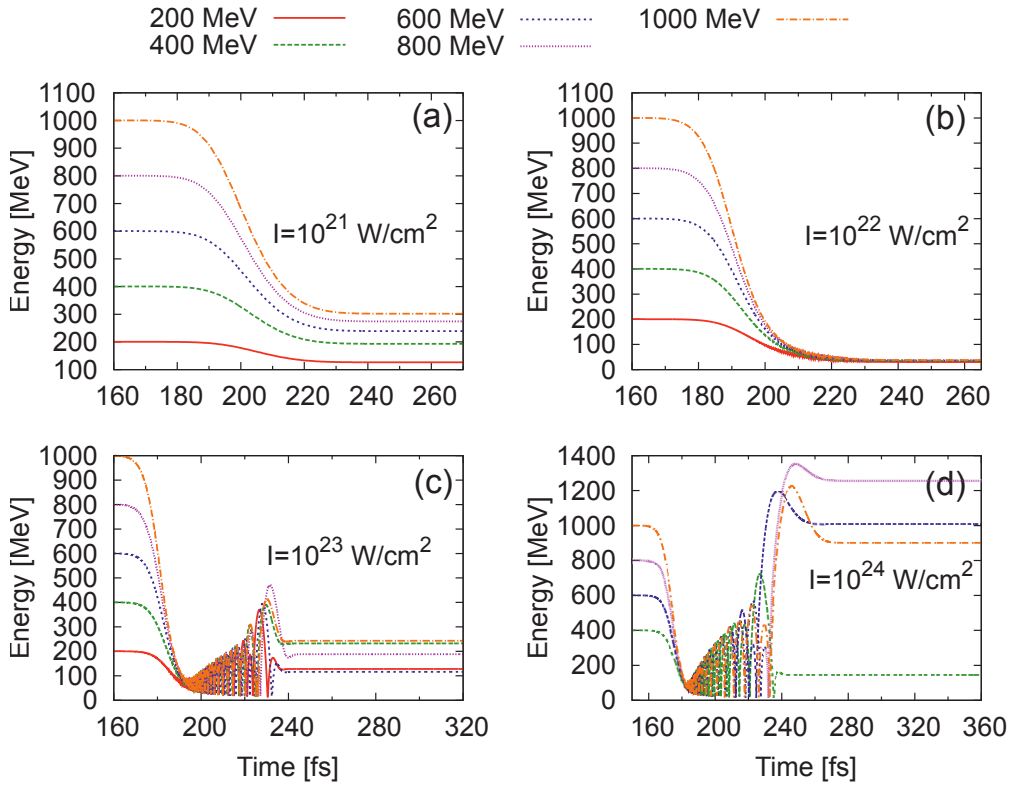

Figure 3.7: The time evolution of electron energy at different laser intensities are shown with the effects of RR included. The electron initial energies are 200 MeV, 400 MeV, 600 MeV, 800 MeV and 1000 MeV.

energy between 10 MeV - 1GeV scattering from 83 fs laser pulse at $I = 10^{21}$ W/cm^2 and $I = 10^{22}$ W/cm^2 are shown in Fig. 3.8. The emission spectra is normalized to initial kinetic energy of electron. Intuitively, one may expect that the peak location of the emission spectrum will increase as we increase the initial kinetic energy of the electron. For instance, the peaks of the emission spectra shift to the right when the energy of the electron is increased as shown in Fig. 3.8 (a). However, the peaks are saturated around 1 MeV at $I = 10^{22}$ W/cm^2 even if the electron energy is increased to 1 GeV as shown in Fig. 3.8 (b). It was shown that an electron with an initial energy of 1 GeV counterpropagtes with respect to the laser at $I = 10^{22}$ W/cm^2 ($R_C \approx 0.33$) is below the CRDR. However, the condition for CRDR is defined for single laser period. For $R_C < 1$ the integral term in Eq. (2.38) can be larger than unity for a laser pulse. In order to make a prediction, we assume a linearly polarized vector potential of the laser field that resembles Gaussian shape

$$\mathbf{a} = a_0 \psi(\xi) \hat{\mathbf{y}} \tag{3.4}$$

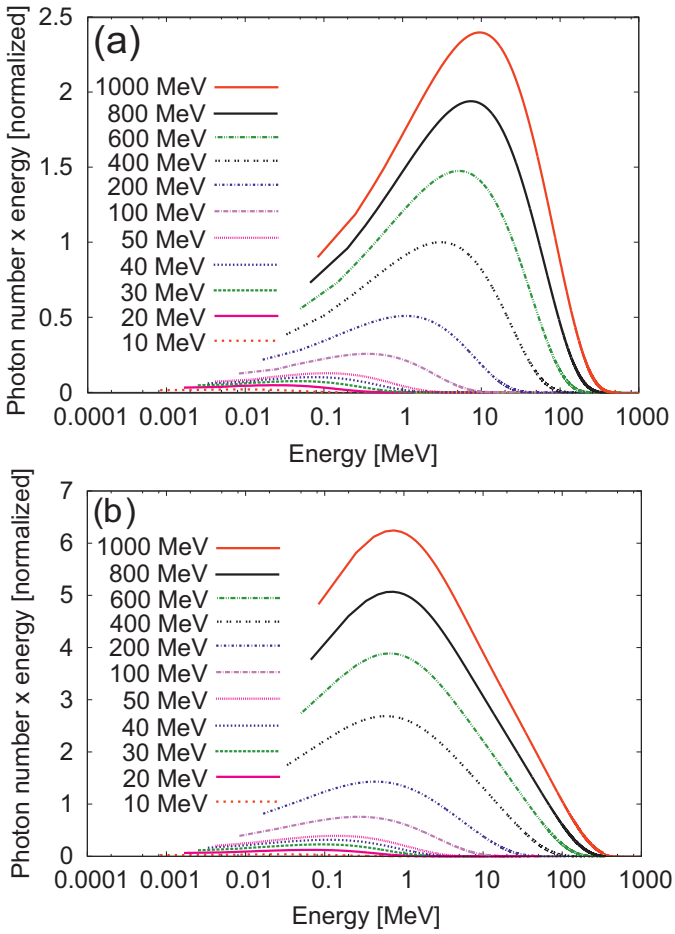

Figure 3.8: Emission spectra of an electron with different initial energy interacting with 83 fs laser pulse at (a) $I = 10^{21}$ W/cm^2 and (b) $I = 10^{22}$ W/cm^2. The emission spectra is normalized to initial kinetic energy of electron. The peak location of the spectra at $I = 10^{22}$ W/cm^2 are saturated as the initial energy of electron increases due to RR effects.

where $\psi(\xi) = g(\xi)e^{i\xi}$, $g(\xi) = \text{sech}(\xi/\xi_0)$, $\xi_0 = \omega_0 t_L = 2\pi N$ and N is the number of laser cycles. The pulse shape function $g(\xi) = \text{sech}(\xi/\xi_0)$ is chosen instead of $g(\xi) = \exp[-(\xi/\xi_0)^2]$ and the condition $g' << g$ is satisfied for simplicity of analytic estimation. The second term of the denominator of Eq. (2.38) becomes

$$R_C \xi_0 \tanh\left(\frac{\xi}{\xi_0}\right). \tag{3.5}$$

For a short laser pulse duration, $\xi_0 \sim 1$, the term $R_C\xi_0 \longrightarrow R_C$ and the effects of RR are negligible for $R_C << 1$. For a long laser pulse duration, $\xi_0 >> 1$ and $R_C\xi_0 \gtrsim 1$ then the RR is not negligible even if $R_C << 1$. As a result, the effects of RR become significant as a cumulative effect.

The difference in the photon number distribution between the laser intensity of 10^{21} W/cm^2 and 10^{22} W/cm^2 can be observed in the production of high energy photon. For instance, no photon with energy of 1 MeV is produced by 10 MeV electron at 10^{21} W/cm^2 as shown in Fig. 3.9 (a), while some photons with this energy are produced at 10^{22} W/cm^2 as shown in Fig. 3.9 (b). The number of photon produced with the energy of 1 MeV at the laser intensity of 10^{22} W/cm^2 by the electron with energy above 100 MeV are roughly the same as shown in Fig. 3.9 (b). It can be concluded that the increase in laser intensity opens the channel for high energy photon production. The effects of RR on photon production will be shown next.

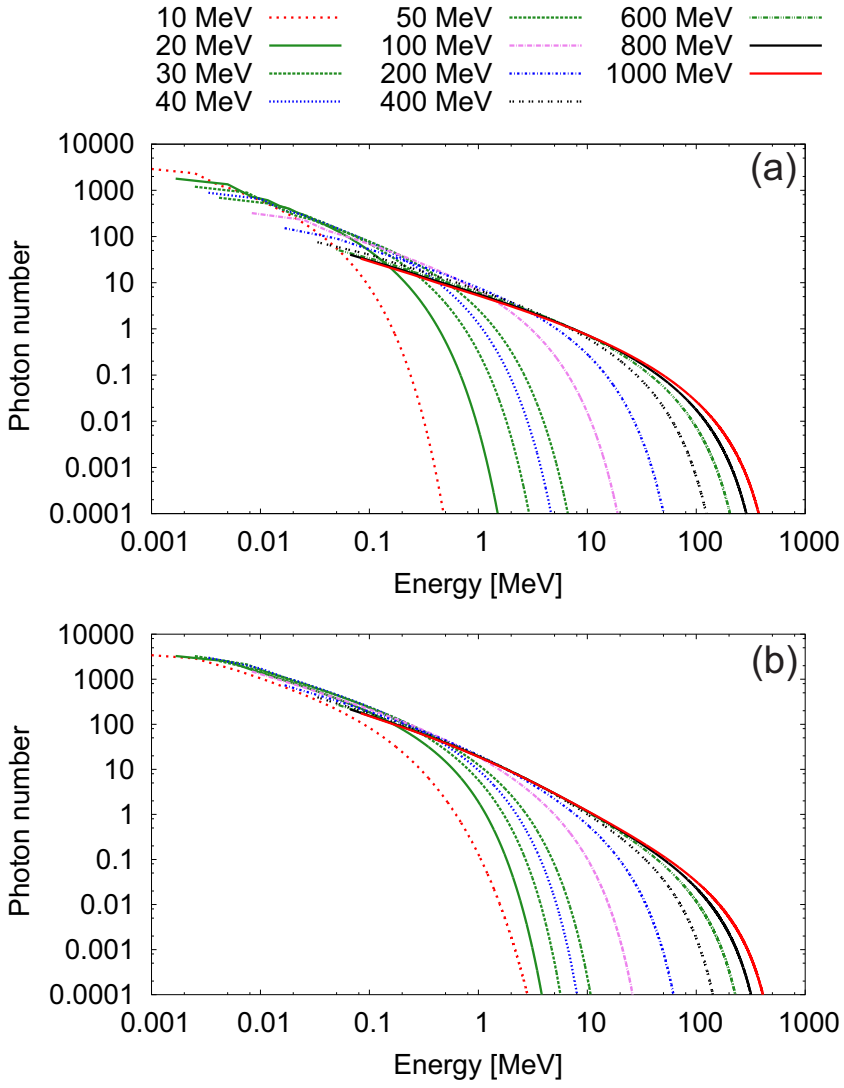

Figure 3.9: Photon number distribution of an electron with different initial energy interacting with a 83 fs laser pulse at (a) $I = 10^{21}$ W/cm^2 and (b) $I = 10^{22}$ W/cm^2.

The comparison of emission spectra and photon number distributions for 100 MeV

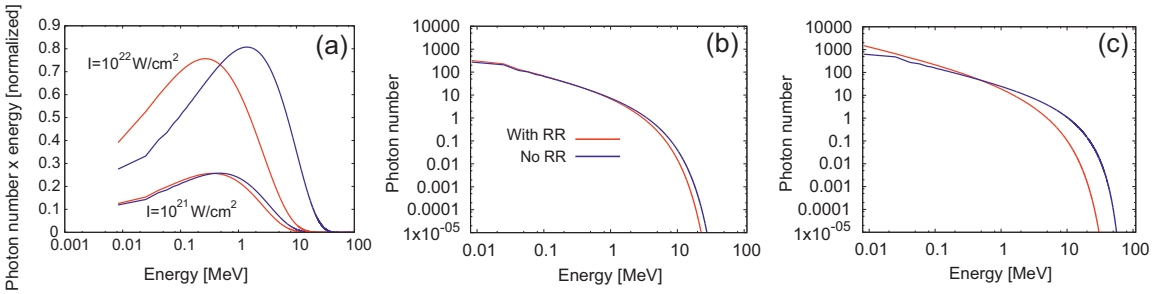

Figure 3.10: Comparison of emission spectra and photon number distribution with RR and without RR for 83 fs laser pulse interacting with 100 MeV electron. (a) The emission spectra for two different intensities. (b) The photon number distribution at the laser intensity of $I = 10^{21}$ W/cm^2 and (c) at $I = 10^{22}$ W/cm^2. In 0.1% bandwidth at 15 MeV photon energy, an electron emits about 2.5×10^9 photons per pulse with RR while 7.2×10^{10} photons per pulse without RR at $I = 10^{22}$ W/cm^2. The difference of photon production rate is small at $I = 10^{21}$ W/cm^2.

electron are shown in Fig. 3.10 (a) & (b) at $I = 10^{21}$ W/cm^2 with $R_C \approx 3 \times 10^{-3}$. For example, a laser pulse of 1000 cycles, the RR becomes significant but for a 83 fs, the pulse duration is about 25 cycles. Thus, for 83 fs pulse duration, the cumulative effects of RR are small where $R_C\xi_0 \approx 0.47 < 1$. The same situation at $I = 10^{22}$ W/cm^2 gives $R_C \approx 0.03$ and the cumulative effects of RR become significant for a 83 fs laser pulse ($R_C\xi_0 \approx 4.71 >> 1$) as seen in Fig. 3.10 (a) & (c). The number of emitted photon will be different for an electron scattering off a 83 fs pulse at $I = 10^{22}$ W/cm^2. For instance, an electron emits about 2.5×10^9 photons per pulse in 0.1% bandwidth of photon energy at 15 MeV. This is 30 times smaller that the case without RR. On the other hand, there is only about 5 times difference for the case at $I = 10^{21}$ W/cm^2 as seen in Fig. 3.10 (b).

The emission spectra of similar configuration and parameters with pulse duration of 10 fs are shown in Fig. 3.11 (a) & (b) for laser intensity of 10^{21} W/cm^2 and 10^{22} W/cm^2 respectively. It is easily observed that the spectra scaled intuitively with electron energy because the cumulative effects of RR are small for a 10 fs laser pulse. Fig. 3.12 compares the spectra with and without RR for a pulse duration of 10 fs and $R_C\xi_0 \approx 0.56 < 1$ at the laser intensity of 10^{22} W/cm^2. From this figure, we can conclude that the RR dominantly affects the spectrum when the laser pulse duration is long.

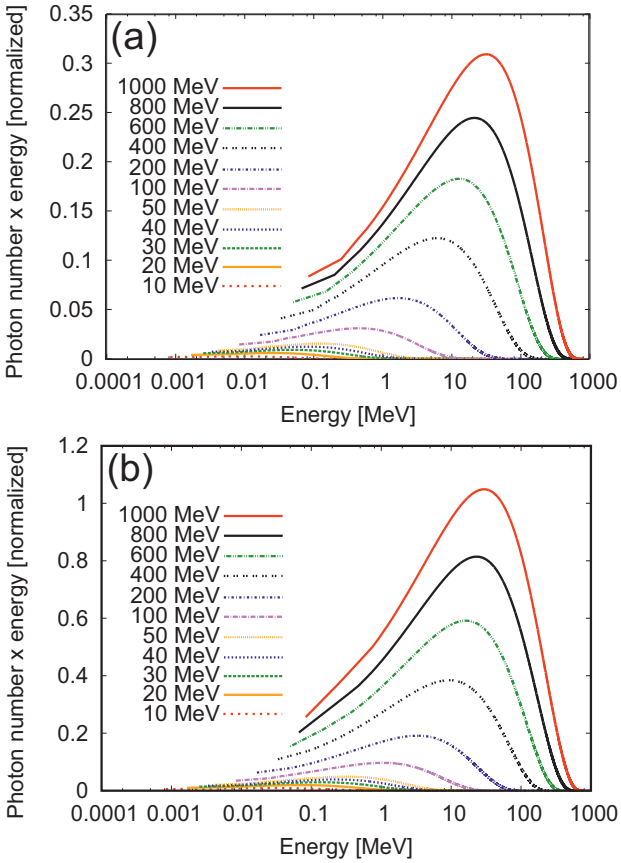

Figure 3.11: Emission spectra of an electron with different initial energy interacting with 10 fs laser pulse of intensity (a) $I = 10^{21}$ W/cm^2 and (b) $I = 10^{22}$ W/cm^2.

3.3.3 Peaks of the emission spectra

In order to compare the peak location of our results to the case without RR, we use the result of synchrotron radiation in which the effects of RR is not taken into account. Following the principle of synchrotron radiation in uniform magnetic field, a charged particle moves at relativistic speed in circular orbit emits radiation into a cone of $\Delta\theta \propto 1/\gamma$ and observer sees the radiation with a time duration of [17, 27]

$$T = \frac{1}{2\gamma^2}\frac{\rho}{c\gamma} \tag{3.6}$$

where ρ is the radius of curvature. The emission spectrum contains harmonics and extends up to critical frequency

$$\hbar\omega_c = \frac{3}{2}\gamma^3\frac{\hbar c}{\rho}. \tag{3.7}$$

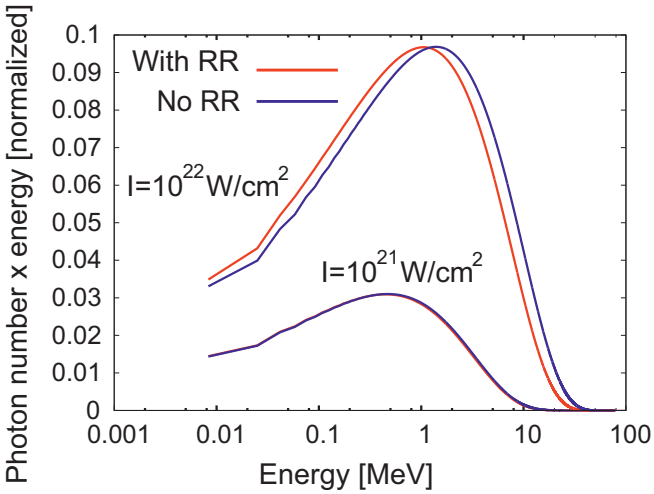

Figure 3.12: Comparison of emission spectra and photon number distribution with RR and without RR for a laser pulse duration of 10 fs interacting with 100 MeV electron.

For an arbitrary motion of a charged particle in the external field, a portion of the path traveled are assumed resembling an arc of circle. The critical frequency is written as

$$\hbar\omega_c = \frac{3}{2}\gamma^2\frac{\hbar eB}{m} \tag{3.8}$$

where the radius of curvature is given by $m\beta c\gamma/eB$ and $\beta \to 1$ for a particle that moves with ultrarelativistic speed. In the case of an electron that counterpropagates with respect to a laser pulse such that $\gamma - p' = 2\gamma$,

$$\chi = \frac{2}{3}\frac{\hbar\omega_0}{mc^2}(\gamma - p')\left|\frac{d\mathbf{a}(\xi)}{d\xi}\right| \sim \frac{4}{3}\frac{\hbar\omega_0}{mc^2}a_0\gamma. \tag{3.9}$$

Following, Ref. [30] the critical frequency can be written as

$$\hbar\omega_c = \frac{4}{3}\gamma^2\hbar\omega_0 a_0. \tag{3.10}$$

From synchrotron radiation, the peak of the emission spectrum is located at

$$\hbar\omega_{peak} = 0.29\hbar\omega_c. \tag{3.11}$$

This relation does not include the effect of RR. Eq. (3.11) is plotted as blue solid and red dashed lines at 10^{22} W/cm^2 and 10^{21} W/cm^2 respectively in Fig. 3.13. The data points are obtained from numerical results with the effects of RR. For a pulse duration of 83 fs (Fig. 3.13 (a)) the peak locations at 10^{22} W/cm^2 (blue square points) fall below the peak locations at 10^{21} W/cm^2 (red triangle points) at electron energy 200 MeV and above. There is not much different for electron energies 40 MeV - 100 MeV. The effects of RR for 83 fs pulse are strong at 10^{22} W/cm^2 with increasing initial kinetic energy of the electron. The peaks of emission spectra are strongly suppressed. In contrast, the peaks follow the relation in Eq. (3.11) at 10^{21} W/cm^2 and 10 fs pulse duration (Fig. 3.13 (b), red triangle points). Similarly, the peak locations at 10^{22} W/cm^2 follow the relation up to 100 MeV and begin to deviate (Fig. 3.13 (b), blue square points) and converge to the same points as in 10^{21} W/cm^2 at 600 MeV - 1000 MeV.

3.3.4 Angular distributions

In synchrotron radiation, the radiation is emitted in the direction of the electron momentum within a very narrow angle. Most of the radiation is emitted within $\Delta\theta$ where $\Delta\theta \propto 1/\gamma$. In Fig. 3.14, the angular distributions of 100 MeV electron interacting with 83 fs laser pulse at 10^{21} W/cm^2 and 10^{22} W/cm^2 were shown for the case with RR and without RR. With the inclusion of RR, the Lorentz factor decreases as electron moves in the laser field. In other words, the electron is slowed down by its own emission and the average Lorentz factor, $< \gamma >$ decreases. This results in the broadening of angular spread. This effect becomes large for higher intensity where RR effectively modifies the electron energy.

3.3.5 Conversion efficiency

We define the total emitted energy and electromagnetic work done normalized to initial kinetic energy of electron $\mathcal{E}_{rad}/\mathcal{E}_0$ and $\mathcal{E}_{EM}/\mathcal{E}_0$ respectively as two different conversion quantities for an electron. The electromagnetic work done is calculated by

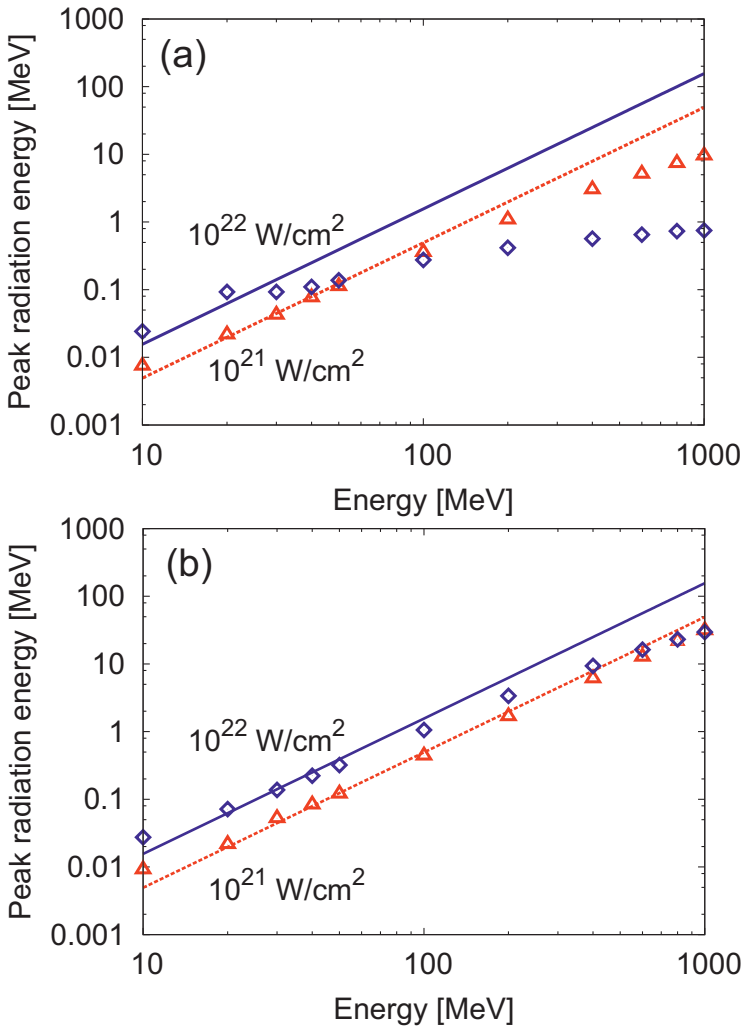

Figure 3.13: The peaks of the emission spectra versus initial kinetic energy of electron for (a) 83 fs and (b) 10 fs laser pulse. The points are numerical results with RR while the lines are the prediction of the peaks as given in Eq. (3.11) without RR.

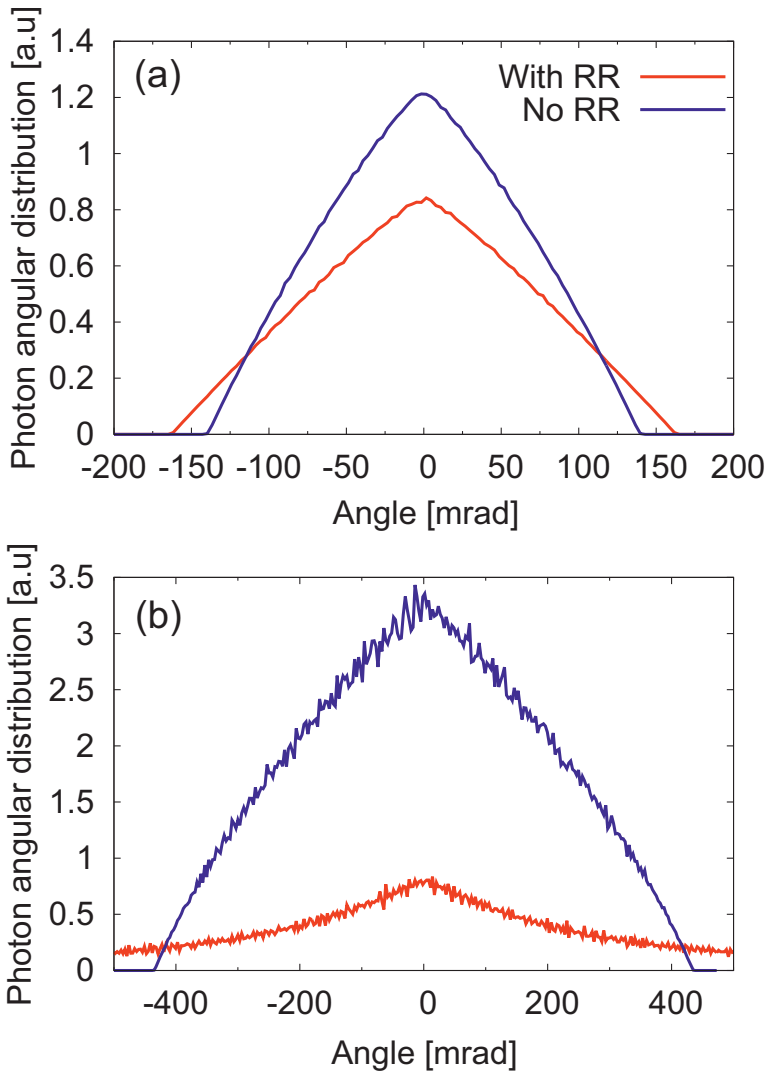

Figure 3.14: Radiation angular distribution of an 100 MeV electron interacting with a 83 fs laser pulse at (a) $I = 10^{21}$ W/cm^2 and (b) $I = 10^{22}$ W/cm^2. The angular spread of radiation is larger for RR case due to the decreasing of Lorentz factor.

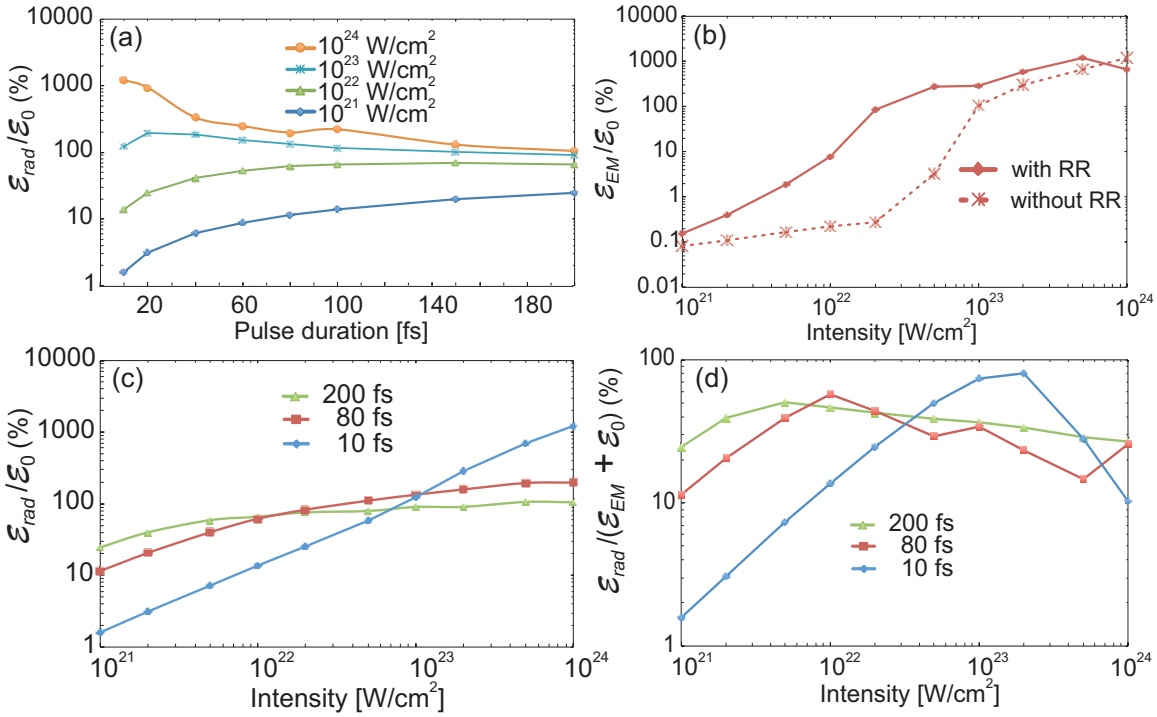

Figure 3.15: (a) Total emitted energy normalized to initial kinetic energy of electron $\mathcal{E}_{rad}/\mathcal{E}_0$ as the function of laser pulse duration where $\mathcal{E}_0 = 40$ MeV. (b) Electromagnetic work done normalized to electron initial energy as the function of laser intensity with RR (solid line) and without RR (dashed line) for pulse duration of 80 fs. (c) Total emitted energy normalized to initial kinetic energy of electron $\mathcal{E}_{rad}/\mathcal{E}_0$ as the function of laser intensities. (d) Radiation energy conversion from electromagnetic work done and initial kinetic energy of electron. Points are numerical result and connected by lines.

integrating the second term on the right hand side of Eq. (2.36):

$$\mathcal{E}_{EM} = \int e(\mathbf{u} + \bar{\mathbf{u}}) \cdot \mathbf{E}\, dt. \tag{3.12}$$

These values may be larger than 100 % and indicating the possibility of excess energy conversion from laser pulse. We also define $\mathcal{E}_{rad}/(\mathcal{E}_{EM} + \mathcal{E}_0)$ as radiation energy conversion from electron initial energy and electromagnetic work done. We consider an electron with initial kinetic energy of 40 MeV which is available at ELBE in HZDR [45].

Fig. 3.15 (a) shows the total emitted energy normalized to electron initial energy as the function of pulse duration. At the laser intensity of 10^{21} W/cm^2 and 10^{22} W/cm^2, the RR is small for a short laser pulse. Thus, only small amount of electron energy is lost into radiation energy. As the laser pulse duration increases, the RR becomes large as a cumulative effect and total electron energy lost into radiation is increased. This

was discussed in Sec. 3.3.2. For these two intensities, the radiation energy comes from the electron and the electromagnetic work done is relatively small. Therefore, the total radiation energy loss is limited by electron initial energy for pulse duration beyond 100 fs and not more than 100 $\%$. At the laser intensity of 10^{23} W/cm^2 and 10^{24} W/cm^2, the total radiation energy is more than 100 $\%$. The excess of energy is drawn from the laser pulse. This is related to electromagnetic work done as shown in Fig. 3.15 (b). However, not all the electromagnetic work done is converted into radiation energy. Most of the work done is used on electron acceleration to higher energy. The longer the pulse duration, the more energy gain by electron for acceleration. Therefore, the emitted radiation energy is suppressed as pulse duration increases.

The work done by the electric field is a conversion of field energy into the momentum of the charged particles. In order to make the field energy conversion happen, the electron velocity has to be parallel to the electric field. The parallel component of electron velocity propagating inside the laser pulse is small for a high initial kinetic energy of the electron. This can be understood from Fig. 3.4 where the velocity is proportional to the trajectory. Therefore, this implies that the work done for an electron with an initial energy of 1 GeV is very small. The decrease of electromagnetic work done with the increasing of the initial kinetic energy of an electron applies to both cases with RR and without RR. However, the work done for the case with RR is slightly higher than the case without RR. This is due to the decreasing of electron effective mass that leads to a larger parallel component of electron velocity. This explains the curve shown in Fig. 3.15 (b). As the laser intensity increases, where $a_0 >> \gamma_0$, the electron reverses its direction of motion for the case with RR. The work done by electromagnetic field become very large, and most of the work done is used to accelerate the electron to higher energy. For the case without RR, the electron may not reverse its direction of motion and the work done remains small. This is shown in Fig. 3.15 (b) from the laser intensity of 10^{22} W/cm^2 to 10^{23} W/cm^2. Beyond that, electron reverses its trajectory for both cases with RR and without RR. Therefore, the difference of the work done in both cases appears to be small.

In Fig. 3.15 (c) the normalized emitted radiation energies are shown as the func-

tion of laser intensities. At the laser intensity of 10^{21} W/cm^2 and 10^{22} W/cm^2, the radiation energy comes mostly from electron. As laser intensity increases to 10^{23} W/cm^2 the electromagnetic work done is dominant and electron emits radiation energy more than its own initial kinetic energy. As described in Fig. 3.15 (a), the longer the pulse duration, the more energy gain by electron for acceleration instead of emission of radiation at the laser intensity of 10^{23} W/cm^2 to 10^{24} W/cm^2. The same explanation applies to the emitted radiation energy for the same laser intensity.

On the other hand, the emitted radiation energy normalized to the total of electromagnetic work and its initial kinetic energy is shown in Fig. 3.15 (d). The optimum of the conversion rate for different pulse duration is observed. For a pulse duration of 10 fs, electron converts up to 80 $\%$ of the total of electromagnetic work and its initial kinetic energy at the laser intensity of 2×10^{23} W/cm^2. The electron emits a total energy of 1.8×10^{-11}J. For a bunch of 6×10^9 electrons from ELBE at HZDR, the total emission energy would be 0.1 J. As the laser intensity is further increased, the radiation emission is limited by electron initial kinetic energy and the electromagnetic work done goes to electron acceleration.

3.4 Summary

In summary, we have demonstrated the effects of RR in the numerical simulation of an ultraintense laser pulse interact with a relativistic electron. In the consideration of the QED effects, we employed the Sokolov's model in the simulation. We began by considering an electron with kinetic energy within the range 10 MeV - 1 GeV undergoes head on collision with counterpropagating 83 fs Gaussian shape laser pulse. We observed that the dynamic of an electron in laser pulse is different with and without RR included. By including the RR effects, the amplitude of electron oscillation is larger due to the decreasing of Lorentz factor γ and lead to the decreases of electron effective mass. For $a_0 << \gamma_0$ the ponderomotive force is small and the electron has sufficient energy to pass through the

laser pulse. While for $a_0 >> \gamma_0$ the ponderomotive force is large and electron direction of motion is reversed.

From the emission spectra, we found that the effects of RR could be observed by using a laser with longer pulse duration at intensities $\sim 10^{22}$ W/cm^2 interacting with 100 MeV counterpropagating electron. It was shown that the peaks of emission spectra were suppressed as the initial kinetic energy of electron increased. We found that such suppression is due to the cumulative effects of RR in many cycles laser pulse. These effects are small for a 10 fs laser pulse. For an electron with an energy of 100 MeV undergoes head on collision with a laser pulse of 83 fs pulse duration, the electron emits roughly 2.5×10^9 photons per pulse at photon energy 15 MeV in 0.1% bandwidth with RR included. At the same energy and bandwidth, the electron would emit around 7.2×10^{10} photons per pulse without RR effect which is 30 times higher from the former case. On the other hand, the electron emits radiation into wider angle if RR is taken into account as the electron continuously lost a significant amount of energy inside the laser pulse. By taking into account the effects of RR, electron losses significant amount of energy into radiation emission and part of the electromagnetic work done on the electron is also converted into radiation emission. The total emitted energy is limited by the initial kinetic energy of the electron and also the work done. For a bunch of 6×10^9 electrons with an initial energy of 40 MeV would emit about 0.1 J of radiation when interacting with a 10 fs laser pulse at the laser intensity of 2×10^{23} W/cm^2. The laser energy reduction is assumed to be negligible for the dynamic of an electron in the laser pulse. The laser pulse energy is then assumed to be constant. For a bunch of 1 billion electrons or higher, the laser energy loss has to be included and treated self-consistently by solving Maxwell's equations.

Chapter 4

Particle-in-Cell (PIC) Method

4.1 Particle-in-Cell Algorithm

Particle-in-Cell (PIC) method was developed in the late 1950's and early 1960's to bring the connection between theoretical and experimental study in the field of plasma physics. In plasma, the motion of electrons and ions are governed by the electromagnetic field generated by themselves. In a straightforward manner, one may compute the force for each particle. However, it is impossible to calculate all of them even with the most powerful supercomputer up to date for a typical laboratory plasma consisting 10^{10-14} particles in one centimetre cube. This makes the numerical analysis of the behaviour of plasma becomes difficult. Instead, one can make the assumption such that one simulation particle is a representation of many real particles. Such particle is called *superparticle* or *macroparticle*. By doing this, the computational power required can be reduced and making the numerical analysis of plasma possible.

On the other hand, when this assumption is made, the charge and mass of simulation particle are enlarged while the ratio between them is kept. This makes the force among the simulation particles become large as compared to the real plasma and increases the collisional effect. This becomes a problem to the study of the plasma behaviour especially high-temperature plasma in many phenomena in which the collisional effect is negligible. In order to reduced the collisional effect, the *Finite-Size Particle* (FSP) is used

instead of *Zero-Size Particle* (ZSP).

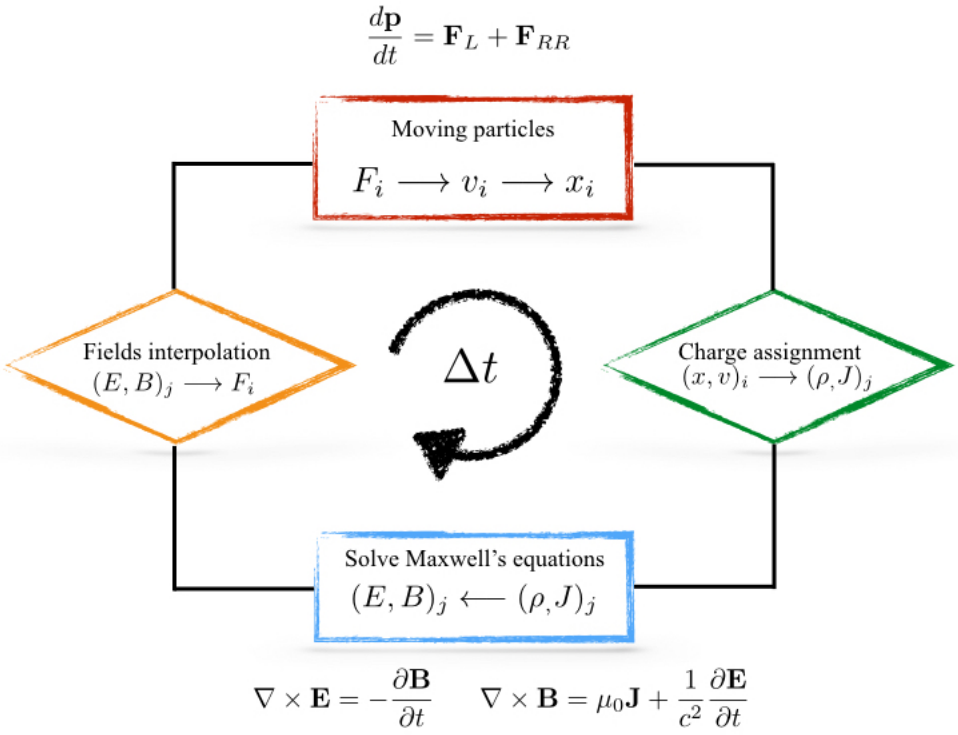

Figure 4.1: The flow chart of PIC method in one time step. The field components are first interpolated to the particle position. The particle position and velocity are pushed forward in one time step. $\mathbf{F_{RR}}$ is the correction to the Lorentz force. From the particle position and velocity, charge density and current density are assigned to the nearest grid points. After that, the new fields are computed by Maxwell's equations. This process repeats until the simulation terminated.

In PIC method, the simulation space is divided into the grid. The electromagnetic fields, charge density and current density are defined on the grid nodes. Meanwhile, the particles can move freely through the grid. Since the fields are defined on the grid nodes, they are interpolated to the position of the particle so that the particle can be pushed to its new position by solving the equation of motion. The particle is pushed forward in time by using leapfrog Boris scheme. Next, the charge of simulation particle is assigned to its neighbouring grid nodes and the new fields are computed by Maxwell's equations. The information of the new fields and particles are brought to the next iteration, and the same process is repeated. The steps are shown in Fig. 4.1.

The radiation reaction force and radiation spectrum are computed based on the method introduced in Sec. 3.1. Detail of Boris scheme and method of solving Maxwell's

equations will be discussed in the coming sections.

4.1.1 Finite-Size Particle (FSP)

The finite-size particle is an artificial simulation particle in which the shape or charge distribution is pre-defined. The shape of FSP is defined such that they feel the Coulomb force of each other when they are far apart while the force is small when they are near. For instance, a collection of point charges or zero-size particle can be described using delta function as

$$q^{SP}\delta(\mathbf{r}-\mathbf{r}_p) \tag{4.1}$$

where r_p is the position of the superparticle and q^{SP} is the chrage of a superparticle so that

$$q^{SP} = \mathcal{M}q \tag{4.2}$$

where $\mathcal{M}$ is the number of real particle in the superparticle. The delta function is three dimensional where $\delta(\mathbf{r}) = \delta(x)\delta(y)\delta(z)$. However, the Coulomb force between two superparticles in two and three dimensions becomes large when they are close to each other. The Coulomb force scales as $r^{-(D-1)}$ where D is the number of spatial dimensions. On the other hand, Coulomb force falls off slowly at large distance and gives rise to the collective behaviour of plasma. In order to keep the collective behaviour while reducing the collisional effect, Eq. (4.1) is replaced by

$$q^{SP}S(\mathbf{r}-\mathbf{r}_p). \tag{4.3}$$

where $S(\mathbf{r})$ is shape factor. The shape factor is symmetry with respect to the origin and the integral in all space is

$$\int S(\mathbf{r})d^3r = 1. \tag{4.4}$$

and $S(\mathbf{r}-\mathbf{r}_p) = S(x-x_p)S(y-y_p)S(y-y_p)$. The charge density and current density are written as

$$\begin{aligned} \rho(\mathbf{r},t) &= \sum_s q_s^{SP} \sum_p^{N_s^{SP}} S(\mathbf{r}-\mathbf{r}_p) \\ \mathbf{J}(\mathbf{r},t) &= \sum_s q_s^{SP} \sum_p^{N_s^{SP}} \mathbf{v}_{ps} S(\mathbf{r}-\mathbf{r}_p) \end{aligned} \tag{4.5}$$

where s is the species of particle (e.g. ion, electron, positron) and N_s^{SP} is the total number of superparticle for each species.

4.1.2 Field interpolation and Charge decomposition

The FSP is placed at any location in the simulation space. In order to push the particle forward by using the equation of motion, the fields have to be interpolated to the particle position. For example, the average effective electric and effective magnetic field acting on the superparticle in one dimension are

$$E(x_p,t) = \int E(x)S(x-x_p)dx. \tag{4.6}$$

Eq. (4.6) calculates the overlap of shape function with the function $E(x)$ representing the fields in a grid cell. By assuming $E(x)$ is constant and performing integration from $x_p - \Delta x$ to $x_p + \Delta x$ for a triangular shape factor the field at particle position is

$$E(x_p,t) = \frac{1}{2}\left(\frac{1}{2}+\Delta\right)^2 E_{i-1} + \left(\frac{3}{4}-\Delta^2\right) E_i + \frac{1}{2}\left(\frac{1}{2}-\Delta\right)^2 E_{i+1} \tag{4.7}$$

where $\Delta = \frac{x_i - x_p}{\Delta x}$ where Δx is the grid spacing. The overlap of the shape function with the constant fields in a grid cell is illustrated in Fig. 4.2. Besides, the charge density and current density in Eq. (4.5) are continuous in space and have to assign to its neighbouring cell nodes so that the new fields can be obtained by solving Maxwell's equations. This method is very similar to the field interpolation. It calculates the overlap of the shape function with the i^{th} cell. The charge density and current density decomposition are

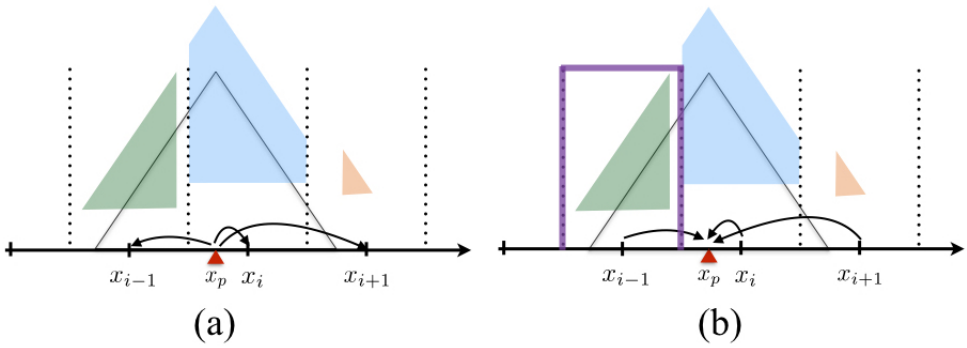

Figure 4.2: The illustration of (a) density decomposition and (b) field interpolation. The region between the dotted lines indicates the territory of x_i. The coloured areas are the overlap of the particle shape function with the (a) grid and (b) field. The colour box represents the field which is assumed to be constant inside a grid territory.

written as

$$\begin{aligned} \rho(i) &= \sum_s q_s^{SP} \sum_p^{N_s^{SP}} \frac{1}{\Delta x} W(x_i - x_p) \\ J(i) &= \sum_s q_s^{SP} \sum_p^{N_s^{SP}} \frac{v_{ps}}{\Delta x} W(x_i - x_p) \end{aligned} \tag{4.8}$$

where

$$W(x_i - x_p) = \begin{cases} \frac{3}{4} - \Delta^2, & \text{if } |\Delta| \leq \frac{1}{2} \\ \frac{1}{2}(\frac{3}{2} - |\Delta|)^2, & \text{if } \frac{1}{2} < |\Delta| \leq \frac{3}{2} \\ 0, & |\Delta| > \frac{3}{2} \end{cases} \tag{4.9}$$

is the weight function for a triangular shape factor. The equation of motion for superparticle reads

$$\frac{d\gamma \mathbf{u}_{sp}}{dt} = \frac{Q_s}{M_s} \left[\mathbf{E}(x_{sp}, t) + \mathbf{u}_{sp} \times \mathbf{B}(x_{sp}, t) \right] \tag{4.10}$$

where Q_s/M_s is the charge to mass ratio for superparticle. It should be noted that the charge to mass ratio of the superparticle is the same as single point particle.

4.1.3 Maxwell's equations

The 3 dimensional Maxwell's equations are

$$\nabla \cdot \mathbf{E} = \frac{\rho}{\epsilon_0} \tag{4.11}$$

$$\nabla \cdot \mathbf{B} = 0 \tag{4.12}$$

$$\nabla \times \mathbf{E} = -\frac{\partial \mathbf{B}}{\partial t} \tag{4.13}$$

$$\nabla \times \mathbf{B} = \mu_0 \mathbf{J} + \frac{1}{c^2}\frac{\partial \mathbf{E}}{\partial t}. \tag{4.14}$$

In PIC method, $\nabla \cdot \mathbf{E} = \rho/\epsilon_0$ and $\nabla \cdot \mathbf{B} = 0$ are assumed to be satisfied at initial condition. Therefore, the charge is conserved and one have to solve only Eq. (4.13) and Eq. (4.14). For instance, by inserting $\nabla \cdot \mathbf{E} = \rho/\epsilon_0$ into Eq. (4.14) and taking the divergence of both side, one obtain the continuity equation

$$\nabla \cdot \mathbf{J} + \frac{\partial \rho}{\partial t} = 0 \tag{4.15}$$

which is a statement of charge conservation. The Maxwell's equations are discretized in space and time and solved by using Finite Different Time Domain (FDTD) method. In FDTD method, fields are distributed onto the grid nodes as shown in Fig. 4.3. This is

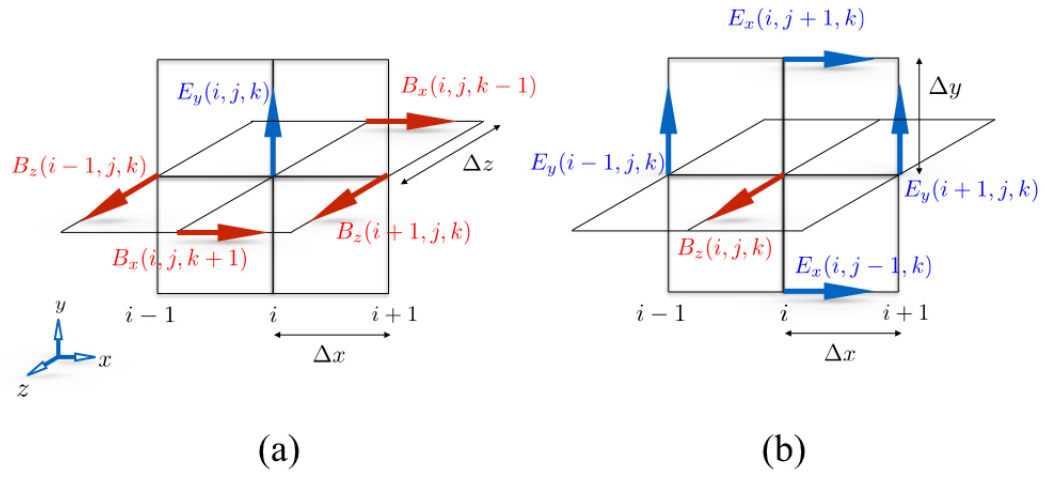

Figure 4.3: The position of the field components on the grid nodes. (a) The transverse magnetic mode (TM) and (b) the transverse electric (TE) mode.

slightly different from Yee scheme [51] where the field components are defined at the centre of a grid. The time and space derivative are discretized according to the finite centre difference which is accurate to second order. In the time domain, the update of $\mathbf{E}$ field and $\mathbf{B}$ field are staggered according to leapfrog scheme. The $\mathbf{E}$ field is advanced by integer time step while $\mathbf{B}$ field is advanced by half integer time step. The discretized form of Eq. (4.13) and Eq. (4.14) reads

$$\begin{aligned} E_y^{n+1}(i,j,k) = E_y^n(i,j,k) &+ c\Delta t \left[\frac{(B_x^{n+\frac{1}{2}}(i,j,k+1) - B_x^{n+\frac{1}{2}}(i,j,k-1))}{2\Delta z} \right. \\ &- \left. \frac{(B_z^{n+\frac{1}{2}}(i+1,j,k) - B_z^{n+\frac{1}{2}}(i-1,j,k))}{2\Delta x} \right] \\ &- J_y^{n+\frac{1}{2}}(i,j,k)\Delta t \\ B_z^{n+\frac{3}{2}}(i,j,k) = B_z^{n+\frac{1}{2}}(i,j,k) &+ c\Delta t \left[\frac{(E_y^{n+1}(i+1,j,k) - E_y^{n+1}(i-1,j,k))}{2\Delta x} \right. \\ &- \left. \frac{(E_x^{n+1}(i,j+1,k) - E_x^{n+1}(i,j-1,k))}{2\Delta y} \right]. \end{aligned} \tag{4.16}$$

Meanwhile, the magnetic field at integer time step is obtained as follow for the used of particle pusher:

$$B_z^{n+1}(i,j,k) = \frac{1}{2}[B_z^{n+\frac{3}{2}}(i,j,k) + B_z^{n+\frac{1}{2}}(i,j,k)]. \tag{4.17}$$

For the stability and accuracy of this scheme, the time step have to satisfy the Courant condition such that $c\Delta t/\Delta x < 1/\sqrt{3}$ for $\Delta x = \Delta y = \Delta z$.

On the other hand, the calculation of charge density and current density requires the position and velocity of the particle which is defined at the different time. Thus, the local charge conservation can not be guaranteed. In order to make sure the local charge conservation at each time step, the current density should be derived from the continuity equation in finite difference form. In this scheme, Gauss law and $\nabla \cdot \mathbf{B} = 0$ should be initially satisfied so that the charge conservation is ensured for each time step. This current conserving scheme is valid for an arbitrary form-factor in Cartesian coordinate.

Detail steps and algorithm of this scheme can be found in Ref. [52].

4.1.4 Boris pusher

After obtaining the field at particle position, the new position and momentum of particle are calculate according to the equation of motion:

$$\begin{aligned} \frac{d\gamma \mathbf{u}_{sp}}{dt} &= \frac{Q_s}{M_s}\left[\mathbf{E}(x_{sp},t) + \mathbf{u}_{sp} \times \mathbf{B}(x_{sp},t)\right] \\ \frac{d\mathbf{x}_{sp}}{dt} &= \mathbf{u}_{sp}. \end{aligned} \tag{4.18}$$

Although the superparticle is used in plasma simulation but the number of superparticles required is still very large. Particle pusher in the simulation is the most CPU time consuming since each particle needs to be moved separately. Therefore, an efficient particle pusher is important. There are two schemes used for the particle pusher namely the implicit and explicit pusher. In the implicit method, the velocity of the particle is updated using the new field. Whereas, in the explicit method the velocity of the particle is updated using the old force which is easier and faster. Two frequently used explicit pusher are leapfrog method and Boris method [53]. The leapfrog method of Eq. (4.18) is written as

$$\begin{aligned} \mathbf{p} &= \gamma \mathbf{u} \\ \frac{\mathbf{p}^{n+\frac{1}{2}} - \mathbf{p}^{n-\frac{1}{2}}}{\Delta t} &= \frac{Q_s}{M_s}\left[\mathbf{E}^n + \frac{\mathbf{p}^{n+\frac{1}{2}} + \mathbf{p}^{n-\frac{1}{2}}}{2\gamma^n} \times \mathbf{B}^n\right] \\ \frac{\mathbf{x}^{n+1} - \mathbf{x}^n}{\Delta t} &= \frac{\mathbf{p}^{n+\frac{1}{2}}}{\gamma^{n+\frac{1}{2}}}. \end{aligned} \tag{4.19}$$

In Boris pusher, the electric force and magnetic force are separated completely by substituting

$$\begin{aligned} \mathbf{p}^{n-\frac{1}{2}} &= \mathbf{p}^{-} - \frac{Q_s}{M_s}\mathbf{E}\frac{\Delta t}{2} \\ \mathbf{p}^{n+\frac{1}{2}} &= \mathbf{p}^{+} + \frac{Q_s}{M_s}\mathbf{E}\frac{\Delta t}{2} \end{aligned} \tag{4.20}$$

into second equation of Eq. (4.19). As a result, it becomes

$$\frac{\mathbf{p}^{+}-\mathbf{p}^{-}}{\Delta t} = \frac{Q_s}{2M_s}\left[\frac{\mathbf{p}^{+}-\mathbf{p}^{-}}{2\gamma^n}\times\mathbf{B}^n\right] \tag{4.21}$$

which is a rotation. At first, $\mathbf{p}^{n-\frac{1}{2}}$ undergoes half time step acceleration by electric force to get $\mathbf{p}^{-}$. Then, $\mathbf{p}^{-}$ is rotated by the magnetic force to obtain $\mathbf{p}^{+}$ and then undergoes the remaining half time step acceleration by electric force to obtain $\mathbf{p}^{n+\frac{1}{2}}$. The Boris algorithm is summarized as follow:

- $\mathbf{p}^{-} = \mathbf{p}^{n-\frac{1}{2}} + \frac{Q_s}{M_s}\mathbf{E}\frac{\Delta t}{2}$
- $\mathbf{t} = \frac{Q_s}{M_s}\frac{\mathbf{B}^n}{\gamma^n}\frac{\Delta t}{2}$
- $\mathbf{p}^{*} = \mathbf{p}^{-} + \mathbf{p}^{-}\times\mathbf{t}$
- $\mathbf{s} = \frac{2\mathbf{t}}{1+t^2}$
- $\mathbf{p}^{+} = \mathbf{p}^{-} + \mathbf{p}^{*}\times\mathbf{s}$
- $\mathbf{p}^{n+\frac{1}{2}} = \mathbf{p}^{+} + \frac{Q_s}{M_s}\mathbf{E}\frac{\Delta t}{2}$.

4.1.5 Energy balance

In PIC method, the field evolves according to Maxwell's equations. During the interaction, energy is transferred from particle to field or vice versa. Thus it is important to check the energy balance for the whole process. The energy equation for the field is written as

$$\frac{\partial W_{EM}}{\partial t} + \nabla\cdot\mathbf{S} = -\mathbf{J}\cdot\mathbf{E} \tag{4.22}$$

where $W_{EM} = \frac{1}{2}\left[\epsilon_0\mathbf{E}^2 + \frac{1}{\mu_0}\mathbf{B}^2\right]$ is the electromagnetic field total energy density and $\mathbf{S}$ is the Poynting vector. Integrating Eq. (4.22) over the volume on both side and substitute the particle energy equation

$$\frac{d\mathcal{E}_e}{dt} = \int \mathbf{J}\cdot\mathbf{E}d^3x - \frac{d\mathcal{E}_{rad}}{dt}. \tag{4.23}$$

one obtains

$$\frac{\partial}{\partial t}\left[\int W_{EM} d^3x + \mathcal{E}_e + \mathcal{E}_{rad}\right] = -\oint \mathbf{S}\cdot d\mathbf{A}. \tag{4.24}$$

Integrating both sides of this equation and assuming that the volume covered over the whole interaction domain goes to infinity, we can write the energy balance equation as

$$\frac{\Delta\mathcal{E}_{field} + \Delta\mathcal{E}_e + \Delta\mathcal{E}_{rad}}{E_{initial}} = 0 \tag{4.25}$$

where $E_{initial} = E_e + E_{laser}$, $\Delta\mathcal{E}_{field} = \mathcal{E}_{field}(t) - \mathcal{E}_{field}(t=0)$, $\Delta\mathcal{E}_e = \mathcal{E}_e(t) - \mathcal{E}_e(t=0)$ and $\Delta\mathcal{E}_{rad} = \mathcal{E}_{rad}(t) - \mathcal{E}_{rad}(t=0)$. $\mathcal{E}_{rad}(t=0)$ is assumed to be zero.

4.1.6 Normalization

Introducing the normalization variables with respect to the wavelength:

$$\begin{aligned}
\mathbf{x}' &\longrightarrow \frac{\mathbf{x}}{\lambda},\ t' \longrightarrow \frac{ct}{\lambda},\ \mathbf{p}' \longrightarrow \frac{\mathbf{p}}{mc},\ \gamma \longrightarrow \frac{E}{mc^2},\\
\mathbf{u}' &\longrightarrow \frac{\mathbf{u}}{c},\ \mathbf{E}' \longrightarrow \frac{e\mathbf{E}\lambda}{mc^2},\ \mathbf{B}' \longrightarrow \frac{e\mathbf{B}\lambda}{mc}\\
\mathbf{J}' &\longrightarrow \frac{4\pi^2}{cen_{cr}}\mathbf{J},\ \rho' \longrightarrow \frac{4\pi^2}{en_{cr}}\rho.
\end{aligned}$$

where the current density and charge density are normalized with respect to critical density, $n_{cr} = m\omega^2\epsilon_0/e^2$. Upon normalization, the equation of motion for superparticle becomes

$$\frac{d\gamma\mathbf{u}'_{sp}}{dt'} = \frac{Q_s}{M_s}\left[\mathbf{E}'(x'_{sp}, t') + \mathbf{u}'_{sp}\times\mathbf{B}'(x'_{sp}, t')\right] \tag{4.26}$$

where Q_s/M_s is the normalized charge to mass ratio such that $Q_e/M_e = -1$ for electron and $Q_i/M_i = Z/(M_i/m_e)$ for ion with charge number, Z and ion mass, M_i. The

normalized charge and current density is then

$$\begin{aligned} \rho'(i) &= N_{const} \sum_s Q_s \sum_p^{N_s^{SP}} W'(x'_i - x'_p) \\ J'(i) &= N_{const} \sum_s Q_s \sum_p^{N_s^{SP}} v'_{ps} W'(x'_i - x'_p). \end{aligned} \tag{4.27}$$

and

$$\begin{aligned} N_{const} &= 2\alpha\lambda'_C \frac{N_s}{N_s^{SP}} \\ W'(x'_i - x'_p) &= \frac{1}{\Delta x'} W(x_i - x_p) \end{aligned} \tag{4.28}$$

with $Q_e = -1$ for electron and $Q_i = Z$ for ion. Meanwhile, normalized Maxwell's equations read

$$\nabla' \cdot \mathbf{E}' = \rho' \tag{4.29}$$

$$\nabla' \cdot \mathbf{B}' = 0 \tag{4.30}$$

$$\nabla' \times \mathbf{E}' = -\frac{\partial \mathbf{B}'}{\partial t'} \tag{4.31}$$

$$\nabla' \times \mathbf{B}' = \mathbf{J}' + \frac{\partial \mathbf{E}'}{\partial t'} \tag{4.32}$$

and the continuity equation is

$$\nabla' \cdot \mathbf{J}' + \frac{\partial \rho'}{\partial t'} = 0. \tag{4.33}$$

The normalized field energy is written as

$$\mathcal{E}'_{field} = \int \frac{1}{2} \left[\mathbf{E}'^2 + \mathbf{B}'^2 \right] d^3x' \tag{4.34}$$

and multiplied by $\mathcal{E}_0 = \frac{emc^2\lambda}{2\alpha\lambda_C}$ to obtain the field energy in Joule.

It was mentioned that the charge to mass ratio for particle and superparticle are the same. Therefore, the dynamics of a superparticle is the same as single particle. However, when the effects of RR is considered the characteristic time is different by a factor of $\mathcal{M}$

from the single particle. The characteristic time for a superparticle is expressed as

$$\tau_0^{SP} = \mathcal{M}\frac{2e^2}{3mc^3}. \tag{4.35}$$

As a result, the particle dynamics would be different for a different number of particle per superparticle. In order to ensure the correct dynamics of superparticle when RR is included, it is necessary to assume that characteristic time of the superparticle is the same as the single particle. This approach gives the same result for particle dynamics and radiation spectrum regardless of the number of real particle in one superparticle [54].

4.2 Fields of Gaussian beams

In order to obtain the laser intensity beyond the order of 10^{22} W/cm^2 for a fixed laser power, the laser needs to be focused to a waist radius of the order of the laser wavelength. For example, a 10 PW laser is focused to 1 μm waist radius gives the laser intensity of the order of $\sim 10^{24}$ W/cm^2. The fields of a tightly focused laser beam need to be described beyond paraxial approximation. Besides, the fields described in PIC method need to satisfy Maxwell's equations $\nabla \cdot \mathbf{E} = 0$ and $\nabla \cdot \mathbf{B} = 0$ to the order of the diffraction angle, $\theta_0 = 2/k\sigma_0$.

The fields of a pulsed Gaussian beam propagating in the $x-$direction can be obtained in a similar way as in McDonald [49, 50] and Y. I. Salamin [48]. Beginning with the configuration specified in Fig. 3.3, the vector potential polarized along the $y-$axis and propagate along the $x-$axis is:

$$\mathbf{A}(x, y, z, t) = \hat{\mathbf{y}} A_0 \Psi(x, y, z) g(\eta) e^{i\eta} \tag{4.36}$$

where g is the laser pulse shape function, $\Psi(x, y, z)$ is spatial envelope function and $\eta =$

$\omega t - kx$. The vector potential needs to satisfy the wave equation

$$\nabla^2 \mathbf{A} = \frac{1}{c^2}\frac{\partial^2 \mathbf{A}}{\partial t^2} \tag{4.37}$$

and it is related to the scalar potential by the Lorentz gauge

$$\nabla \cdot \mathbf{A} + \frac{1}{c^2}\frac{\partial \Phi}{\partial t} = 0. \tag{4.38}$$

The electric field and magnetic field in term of the vector potential and scalar potential are written as

$$\begin{aligned} \mathbf{E} &= -\nabla\Phi - \frac{\partial \mathbf{A}}{\partial t} \\ \mathbf{B} &= \nabla \times \mathbf{A}. \end{aligned} \tag{4.39}$$

Inserting Eq. (4.36) into the wave equation one obtains

$$\nabla^2 \Psi - 2ik\frac{\partial \Psi}{\partial x}\left(1 - \frac{g'}{g}\right) = 0 \tag{4.40}$$

where $g' = dg/d\eta$. In order for Eq. (4.40) to be consistent, the condition $g'/g \ll 1$ have to be satisfied. Making the change of the variable in term of the laser waist radius, σ_0 and Rayleigh length $x_r = k\sigma_0^2/2$

$$\xi = \frac{y}{\sigma_0}, \quad \upsilon = \frac{z}{\sigma_0}, \quad \zeta = \frac{x}{x_r}, \quad \rho^2 = \xi^2 + \upsilon^2 \tag{4.41}$$

Eq. (4.40) takes the form

$$\nabla_\perp^2 \Psi - 4i\frac{\partial \Psi}{\partial \zeta} + \theta_0^2 \frac{\partial^2 \Psi}{\partial \zeta^2} = 0 \tag{4.42}$$

where

$$\nabla_\perp^2 = \frac{\partial^2}{\partial \xi^2} + \frac{\partial^2}{\partial \upsilon^2}. \tag{4.43}$$

Eq. (4.42) can be solved by the series expansion of

$$\Psi = \Psi_0 + \theta_0^2 \Psi_2 + \theta_0^4 \Psi_4 + ... \tag{4.44}$$

in term of the small parameter θ_0^2. Inserting this series expansion and collecting the terms with the coefficient of θ_0 and one obtains

$$\nabla_\perp^2 \Psi_0 - 4i\frac{\partial \Psi_0}{\partial \zeta} = 0, \tag{4.45}$$

$$\nabla_\perp^2 \Psi_2 - 4i\frac{\partial \Psi_2}{\partial \zeta} + \frac{\partial^2 \Psi_0}{\partial \zeta^2} = 0, \tag{4.46}$$

$$\nabla_\perp^2 \Psi_4 - 4i\frac{\partial \Psi_4}{\partial \zeta} + \frac{\partial^2 \Psi_2}{\partial \zeta^2} = 0. \tag{4.47}$$

The solution of Eq. (4.45) is the paraxial approximation [55] while the solution of Eq. (4.46) and Eq. (4.47) gives the higher order corrections [56]. These solutions are

$$\Psi_0 = f e^{-f\rho^2}, \tag{4.48}$$

$$\Psi_2 = \left(\frac{f}{2} - \frac{f^3\rho^4}{4}\right)\Psi_0, \tag{4.49}$$

$$\Psi_4 = \left(\frac{3f^2}{8} - \frac{3f^4\rho^4}{16} - \frac{f^5\rho^6}{8} + \frac{f^6\rho^8}{32}\right)\Psi_0, \tag{4.50}$$

where

$$f = \frac{i}{i+\zeta} = \frac{e^{i\Psi_G}}{\sqrt{1+\zeta^2}}; \quad \Psi_G = \tan^{-1}\zeta \tag{4.51}$$

and Ψ_G is the Gouy phase which change from $-\pi/2$ to $\pi/2$ as x change from $-\infty$ to ∞. Meanwhile, the structure of scalar potential is chosen analogous to the vector potential in the form of

$$\Phi = g(\eta)\phi(x,y,z)e^{i\eta}. \tag{4.52}$$

and one obtains

$$\frac{\partial \phi}{\partial t} = i\omega\phi\left(1 - \frac{g'}{g}\right) \sim \omega\phi. \tag{4.53}$$

By using the Lorentz gauge we obtain

$$\phi = \frac{i}{k}\nabla \cdot \mathbf{A}. \tag{4.54}$$

Eq. (4.39) can then be written as

$$\mathbf{E} = -i\omega\mathbf{A} - \frac{ic}{k}\nabla(\nabla \cdot \mathbf{A}); \;\; \mathbf{B} = \nabla \times \mathbf{A}. \tag{4.55}$$

The real part of the electric field and magnetic field components up to the order of θ_0^4 are

$$\begin{aligned}
E_x &= E\xi\left\{\theta_0 C_2 + \theta_0^3\left[-\frac{C_3}{2} + \rho^2 C_4 - \frac{\rho^4 C_5}{4}\right]\right\}, && (4.56)\\
E_y &= E\left\{S_1 + \theta_0^2\left[\xi^2 S_3 - \frac{\rho^4 S_4}{4}\right] + \theta_0^4\left[\frac{S_3}{8} - \frac{\rho^2 S_4}{4}\right]\right\}, && (4.57)\\
E_z &= E\xi\upsilon\left\{\theta_0^2 S_3 + \theta_0^4\left[\rho^2 S_5 - \frac{\rho^4 S_6}{4}\right]\right\}, && (4.58)\\
B_x &= \frac{E}{c}\upsilon\left\{\theta_0 C_2 + \theta_0^3\left[\frac{C_3}{2} + \frac{\rho^2 C_4}{2} - \frac{\rho^4 C_5}{4}\right]\right\}, && (4.59)\\
B_y &= 0, && (4.60)\\
B_z &= \frac{E}{c}\left\{S_1 + \theta_0^2\left[\frac{\rho^2 S_3}{2} - \frac{\rho^4 S_4}{4}\right] + \theta_0^4\left[-\frac{S_3}{8} + \frac{\rho^2 S_4}{4} + \frac{5\rho^4 S_5}{16} - \frac{\rho^6 S_6}{4} + \frac{\rho^8 S_7}{32}\right]\right\} && (4.61)
\end{aligned}$$

where

$$\begin{aligned}
E &= E_0 g(\eta) e^{-r^2/\sigma}; \;\; \sigma = \sigma_0\sqrt{1+\zeta^2}; \;\; r^2 = x^2 + y^2\\
C_n &= \left(\frac{\sigma_0}{\sigma}\right)^n \cos(\psi + n\Psi_G); \;\; n = 1, 2, 3, ...,\\
S_n &= \left(\frac{\sigma_0}{\sigma}\right)^n \sin(\psi + n\Psi_G);\\
\psi &= \psi_0 + \omega t - kx - \frac{kr^2}{2R}; \;\; R = x + \frac{x_r^2}{x}
\end{aligned} \tag{4.62}$$

and ψ_0 is the constant initial phase. The field components in Eq. (4.56) - (4.61) satisfy Maxwell's equations $\nabla \cdot \mathbf{E} = 0 = \nabla \cdot \mathbf{B}$ plus terms of order θ^6 [57]. A possible choice

of the temporal pulse function that satisfies the condition $g'/g \ll 1$ is

$$g(\eta) = \frac{1}{\cosh(\frac{\eta}{\eta_0})} \tag{4.63}$$

where $\eta_0 = \omega_0 t_L = 2\pi N$ and N is the number of laser cycles.

Chapter 5

3D PIC Simulation

In Chapter 3, the laser energy was assumed to be constant, and the fields are not solved by Maxwell's equations. This condition is valid for a single particle. However, Fig. 3.15 (b) showed that the electromagnetic work becomes significant at laser intensity above 10^{22} W/cm^2 without RR and 2×10^{23} W/cm^2 if RR is taken into account. In particular, when a bunch of 10^9 electrons are involved in the interaction. Thus, the laser energy can no longer be assumed to be constant, and the conversion efficiency will be overestimated. As a solution, we need to solve Maxwell's equations and the equation of motion for radiating charged particles self-consistently via Particle-in-Cell (PIC) method.

Besides, the laser energy cannot be defined for 2D system as there is only one spatial variation along the polarization plane. In order to study the laser field energy variation, 3D system is required. On the other hand, when the laser is focused into a waist radius of the order of laser wavelength, longitudinal field component cannot be neglected for off-axis electron. Therefore, 3D simulation is necessary when considering the finite beam size for laser and electron beam.

In the following sections, the 3D PIC simulation results will be presented. The results include the charge density, emission spectra, photon number distribution and photon angular distribution. Electron beams of different energy, namely 40 MeV and 1 GeV, were applied in the simulation. The 3D PIC simulation results were compared with the results obtained by using the method −where the beam profile is assumed, but Maxwell's

equations are not solved− described in Sec. 3.1.

5.1 Setting

To consider a more realistic situation, the laser beam is taken to be pulsed Gaussian beam up to 5$^{\text{th}}$ order correction as shown in Sec. 4.2. An electron beam with Gaussian profile is considered and the phase space distribution is

$$f(\mathbf{x},\mathbf{p}) = \exp\left[-\frac{x^2}{2\sigma_L^2} - \frac{y^2+z^2}{2\sigma_T^2} - \frac{p_i^2}{2\sigma_{p_i}^2}\right] \tag{5.1}$$

where $p_i^2/\sigma_{p_i}^2 = p_x^2/\sigma_{p_x}^2 + p_y^2/\sigma_{p_y}^2 + p_z^2/\sigma_{p_z}^2$, σ_{p_i} is the momentum spread while σ_L and σ_T being the longitudinal and transverse beam spread respectively. The value for σ_L and σ_T are both taken to be 1 μm while the momentum spread is taken to be 5 $\%$ of the initial momentum of the electron. A laser pulse with 10 fs pulse duration propagates in the $x-$direction from the left of the simulation domain and focused to 2 μm waist at the center as shown in Fig. 5.1 (b). Meanwhile, the electron beam propagates in the opposite direction as shown in Fig. 5.1 (a). There are a total of 40000 superparticles to represent 1×10^9 electrons. The size of the simulation domain in the $x-$direction has the length of 50 μm while 10 μm in both $y-$ and $z-$directions. The simulation domain has a total of 1000 $\times$ 200 $\times$ 200 cells. The time step is taken to fulfil the Courant condition where $c\Delta t = 0.5\Delta x$.

In the PIC simulation of an electron motion in the background field, the grid size is necessary to be smaller than the Larmor radius so that the information of electron can be well resolved. The Larmor radius for a relativistic electron ($v \approx c$) can be written as $R_m = \gamma\lambda/2\pi a_0$. For instance, $R_m = 0.046$ μm for a 40 MeV electron ($\gamma \approx 80$) at $a_0 = 380$ while $R_m = 0.374$ μm for 1 GeV electron ($\gamma \approx 2000$) at $a_0 = 850$. However, the Lorentz factor γ is dynamic and change over the time if the effects of RR is included. So, the grid size for each cell is set to be $\Delta x = \Delta y = \Delta z = \lambda/20 = 0.05$ μm for laser wavelength of $\lambda = 1$ μm and the time step becomes Δt =0.083 fs.

The mentioned grid size and time step are the smallest for current work. The smaller resolution required a more sophisticated parallelization which is limited by the time constraint of this study. The accuracy of the results are checked by the conservation of the total energy at every time step and are shown in Fig. 5.8 and Fig. 5.14. The energy is conserved within 0.1 % of the total initial energy (laser energy + electron beam) for the case of RR.

The simulations presented in this thesis consist of 16 full-scale 3D simulations. The interaction of four laser intensities with two different electron beam energies with and without RR were performed. A maximum memory of 200 GB and 1 hour computation time were spent for one simulation by the supercomputer with vectorization in Cybermedia Center Osaka University. Part of the simulations were performed by using the supercomputer at HZDR. A maximum memory of 200 GB and 13 hours computation time were spent for one simulation without vectorization.

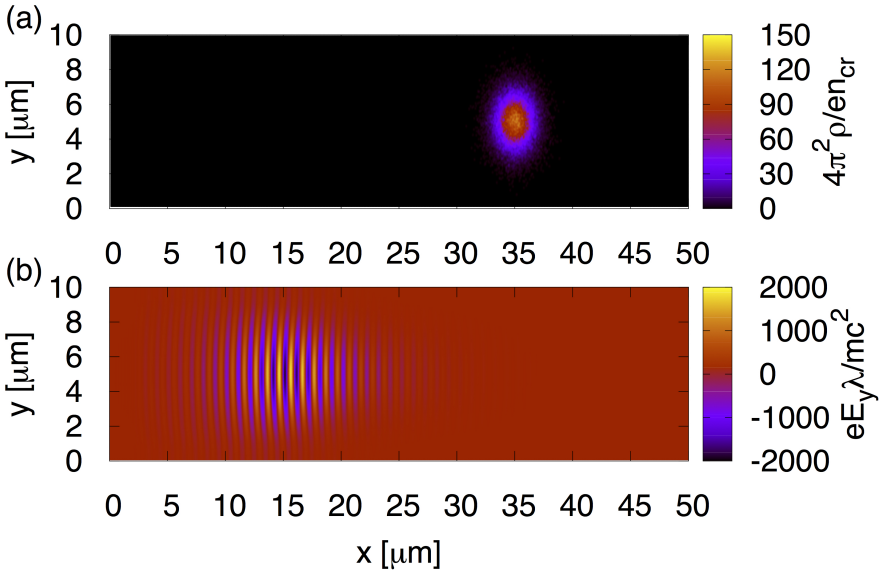

Figure 5.1: Initial setting of the simulation. (a) The charge density of an electron beam travelling in the $-x$ direction, (b) the field component E_y' for a pulsed Gaussian beam with 10 fs pulse duration propagates in the $+x$ direction and focused to 2 μm waist radius at $x = 25$ μm. The longitudinal and transverse beam spread for electron beam are $\sigma_L = 1$ μm and $\sigma_T = 1$ μm respectively with a total of 1×10^9 electrons.

5.2 Pulsed Gaussian Field Components

In this section, the electric and magnetic field components of pulsed Gaussian laser beam are presented. The field components described by Eq. (4.56) - (4.61) are set as initial conditions for the laser pulse and advanced in time through Maxwell's equations. The laser pulse with the laser intensity of 10^{23} W/cm^2 and pulse duration of 10 fs begins at $x = 12.5$ μm and reaches the focusing region at $x = 25$ μm. Eq. (4.63) is taken as laser temporal pulse shape. The constant initial phase ψ_0 is set to zero.

5.2.1 Results

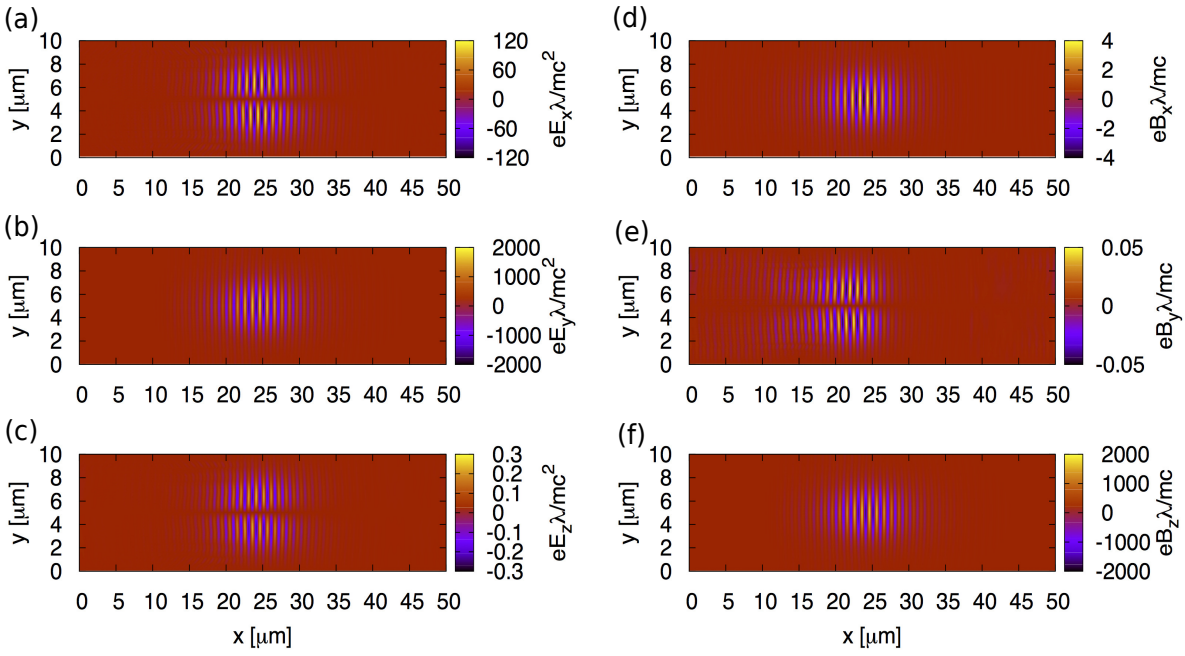

Figure 5.2: The field components (a) E'_x, (b) E'_y, (c) E'_y, (d) B'_x, (e) B'_y and (f) B'_z on the $x-y$ plane at $z = 5$ μm are given at the focusing region. Note that E'_y and B'_z are the strongest components while others are small.

Figure 5.2 (a) - (c) show the electric field components on the $x - y$ plane at $z = 5$ μm, while Fig. 5.2 (d) - (f) are the magnetic field components. The field components E'_x and E'_z is zero along the laser beam axis (i.e. $y = 5$ μm, also note that the difference of the scale for E'_y component compared to E'_x and E'_z). A particle that travels along the beam axis only reacts to E'_y. Meanwhile, the magnetic fields B'_y was set to zero as the initial

condition. However, the fields described by Eq. (4.56) - (4.61) do not satisfy Maxwell's equations exactly. Therefore, the field E'_x and E'_z will contributed to B'_y during the laser propagation as shown in Fig. 5.2 (e). The field magnitude of B'_y is 0.0025% of B'_z and 1.25% of B'_x. The contribution of B'_y to the radiation emission can be neglected for a relativistic particle.

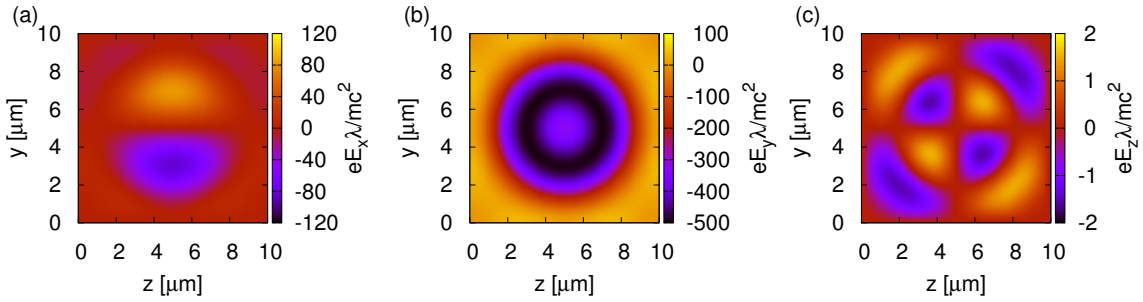

Figure 5.3: The snapshots of the electric field components (a) E'_x, (b) E'_y and (c) E'_z on the $y-z$ plane at $x = 25$ μm.

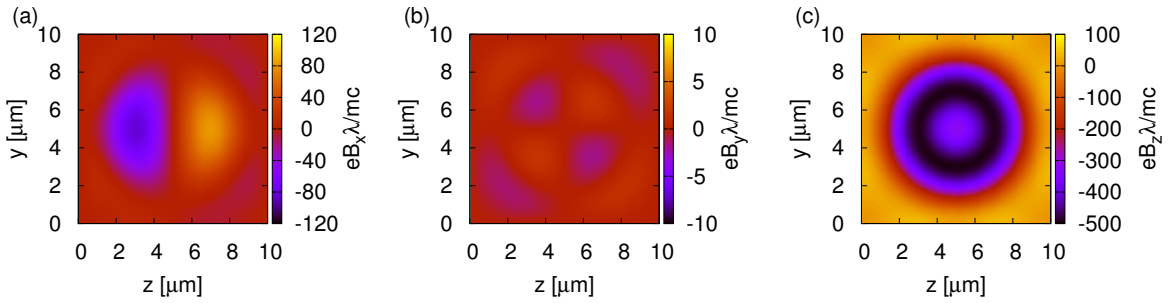

Figure 5.4: The snapshots of the magnetic field components (a) B'_x, (b) B'_y and (c) B'_z on the $y-z$ plane at $x = 25$ μm.

Figure 5.3 and 5.4 show the snapshots of the electric and magnetic field components on the $y-z$ plane at $x = 25$ μm. From this point of view, the electric field component E'_x is zero on the $x-z$ plane at $y = 5$ μm while E'_z is zero on both the $x-z$ plane at $y = 5$ μm and the $x-y$ plane at $z = 5$ μm. On the contrary, the magnetic field component B'_x is zero on the $x-y$ plane at $z = 5$ μm. A small component of B'_y is observed due to the similar reason to Fig. 5.2 (e). E'_x and B'_z being the strongest field components.

5.2.2 Discussions

The emission rate of a charged particle in an arbitrary external electromagnetic field is rather complex. However, there are two approximations can be taken so that the emission rate can be reduced to that of the constant crossed field (i.e. Eq. (2.41)) [58]. First, the wavelength and period of the field should vary in the scale much longer than the coherent interval. This is possible in the limit of $a_0 >> 1$ where the coherent interval $x_{coh} \approx (E_S/E_0)(\hbar/mc) = \lambda/2\pi a_0$ [7] which is the order of Larmor radius. Second, the field invariant parameters $f = |E'^2 - B'^2|/E_S'^2$ and $g = |\mathbf{E}' \cdot \mathbf{B}'|/E_S'^2$ should be much more smaller than unity or χ^2 where the normalized Schwinger field $E_S' = 4.12 \times 10^5$ for $\lambda = 1$ μm. These invariant parameters vanish for a plane electromagnetic wave but do not vanish for the fields described by Eq. (4.56) - (4.61). The cause of non-vanishing f and g is due to the longitudinal field components E_x' and B_x'. The invariant parameters for this laser beam are estimated to be $f, g < 10^{-6}$. We can then assume the field at particle position as constant cross field and Eq. (2.41) can be applied for the pulsed Gaussian beam.

5.3 Interaction of pulsed Gaussian laser beam with 40 MeV electron beam

In conjunction to the observation of high conversion efficiency from a single electron with an energy of 40 MeV at pulse duration of 10 fs at the laser intensity of 2×10^{23} W/cm^2 in Fig. 3.15 in Chapter 3, we performed 3D PIC simulation of the same process by inclusion of a more realistic situation as described in Sec. 5.1.

5.3.1 Results

When speaking in term of the classical radiation-dominant regime, $R_C\xi_0 > 1$ at 10^{23} W/cm^2 and the effects of RR should be strong. However, the effects of RR are not significant at the laser intensity of 2×10^{23} W/cm^2 and 10^{24} W/cm^2. This can be seen at Fig.

5.5 (a) & (b) and Fig. 5.6 (a) & (b). Both of these figures show the charge density of the electron beam with and without RR. Due to the 3-dimensional effects (of the finite laser spot size and electron beam size), the strong ponderomotive force repelled the electrons away from entering the laser pulse. At the edge of the laser beam, the field strength is weak and therefore the effects of RR is small.

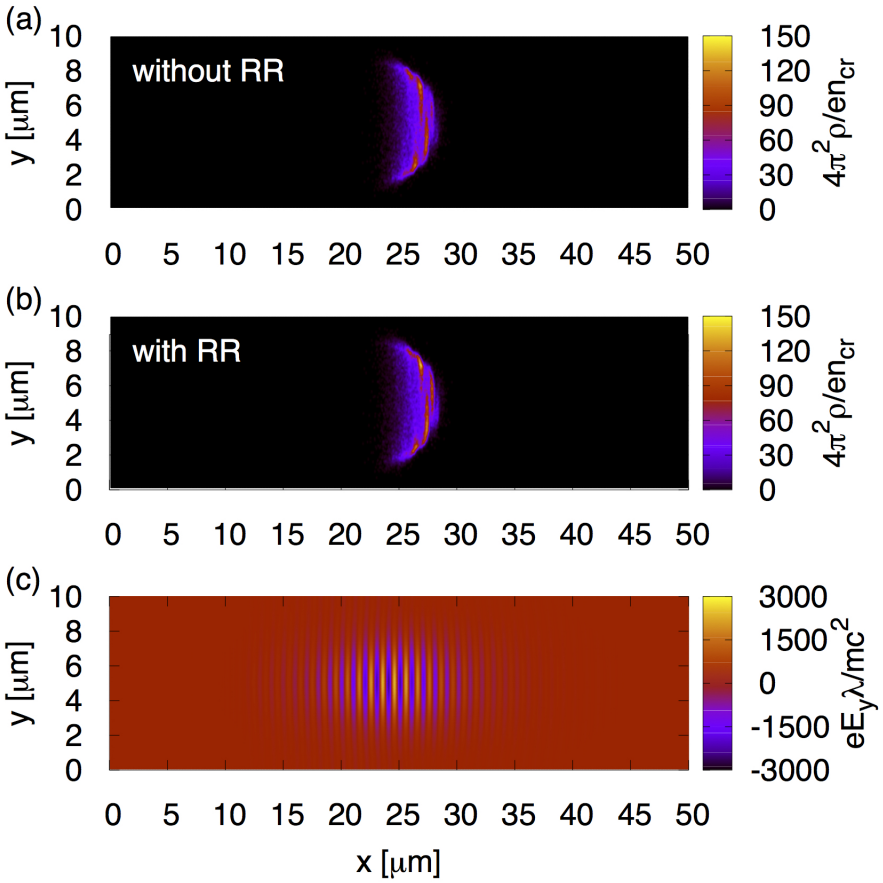

Figure 5.5: The charge density of 40 MeV electron beam (a) without RR, (b) with RR and (c) the field component E_y' at the laser intensity of 2×10^{23} W/cm^2 at the laser focusing region.

The comparison of emission spectra, photon number distributions, and photon angular distribution are shown in Fig. 5.7 at the laser intensity of 10^{24} W/cm^2 while the difference at the laser intensity of 2×10^{23} W/cm^2 is not noticeable as compared to the former case. In Fig. 5.7 (a), the peak locations of the emission spectra do not show a big difference. Meanwhile, there is some suppression of photon production at high photon energy when the RR is included as shown in Fig. 5.7 (b). The electron beam emits about

4×10^{18} photons per pulse in 0.1 % bandwidth at the photon energy of 15 MeV for the case with RR, which is one order smaller than the case without RR.

The strong ponderomotive force not only pushes the electrons to the region of a weaker field but also pushes them in the opposite direction (i.e. trajectories of electrons are reversed) as observed in the case of a single particle in Fig. 3.4 (d) of Chapter 3. Therefore, radiation will be emitted in the direction of the electron momentum and distributed over 2π direction. The rule of $\Delta\theta \propto 1/\gamma$ only valid for single electron but not for a whole bunch of electrons.

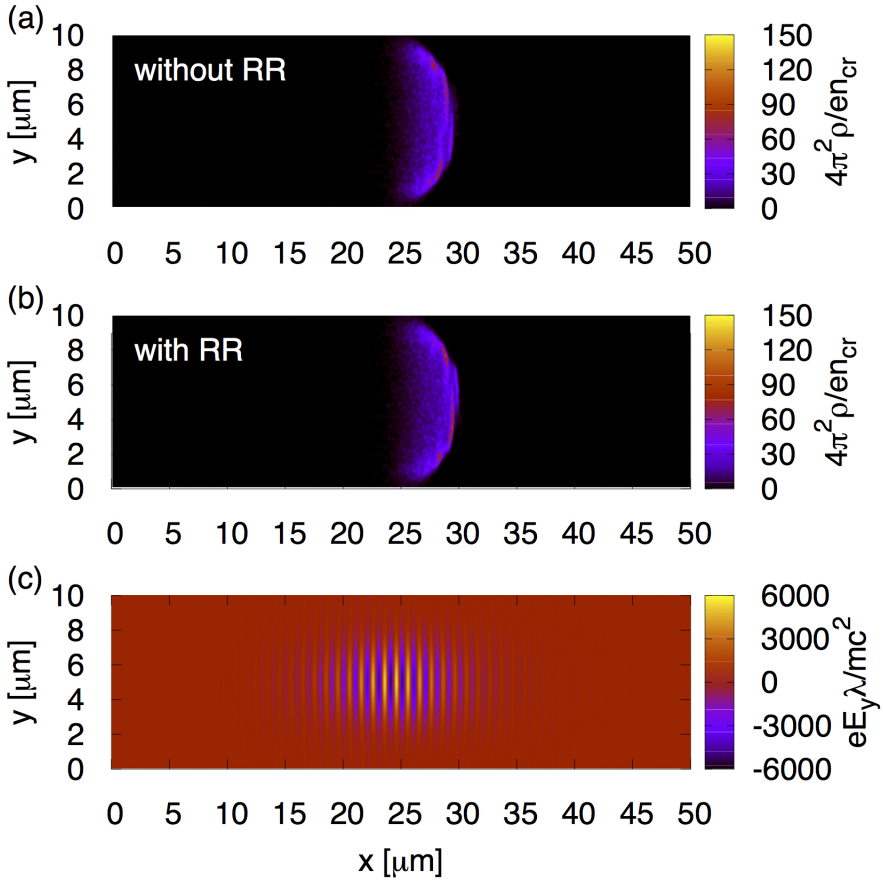

Figure 5.6: The charge density of 40 MeV electron beam (a) without RR, (b) with RR and (c) the field component E'_y at the laser intensity of 10^{24} W/cm^2 at the laser focusing region.

The time evolution of energy conservation at the laser intensity of 2×10^{23} W/cm^2 and 10^{24} W/cm^2 are shown in Fig. 5.8. The electric field energy and magnetic field energy of the electron beam are not taken into account as the initial conditions. When the field

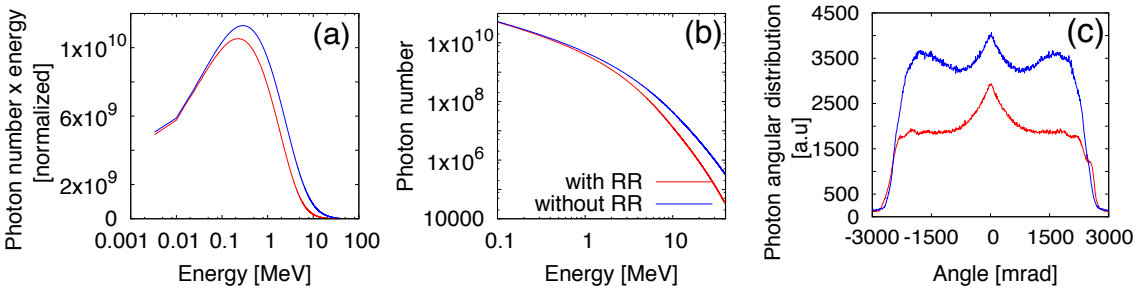

Figure 5.7: Comparison of (a) emission spectra, (b) photon number distribution and (c) photon angular distribution with RR and without RR at the laser intensity of 10^{24} W/cm^2. In 0.1 % bandwidth at 15 MeV photon energy, an electron beam emits about 4×10^{18} photons per pulse with RR while it is one order larger for the case without RR.

energy of the electron beam is taken into account via Maxwell's equations from the first time step, the fluctuation gradually decreases. However, the field energy from the beam is rather small and will not give a serious deviation to the total energy conservation.

One can observe that the laser field energy is transferred to electrons, and only a small fraction is converted into radiation emission. The strong laser field depletion at the laser intensity of 2×10^{23} W/cm^2 is due to a larger number of electrons with velocity parallel to E_y' in the strong field region as compared to the laser intensity of 10^{24} W/cm^2. At the laser intensity of 10^{24} W/cm^2, most of the electrons are in the region of a weaker field strength and laser field depletion is thus small. The total energy is conserved within 0.006 % for all cases shown in Fig. 5.8.

In addition, Fig. 5.9 shows the time evolution of the average energy for 40 MeV electron beam with the effects of RR included. At the laser intensities above 10^{22} W/cm^2 electrons are accelerated to higher energy which is similar to the case of an electron in Chapter 3. Due to the fact that the electrons are being pushed towards the region of weaker field strength, the values of χ are not more than 0.1 as shown in the secondary axis of Fig. 5.9. At such a low value of χ, pair production is unlikely to occur. This verified the assumption in Chapter 2 that pair production is negligible in such case.

5.3.2 Discussions

As discussed at the end of Sec. 5.1, the Larmor radius is not resolved for the cases of higher intensities for 40 MeV electron beam. The unresolved grid might lead to energy

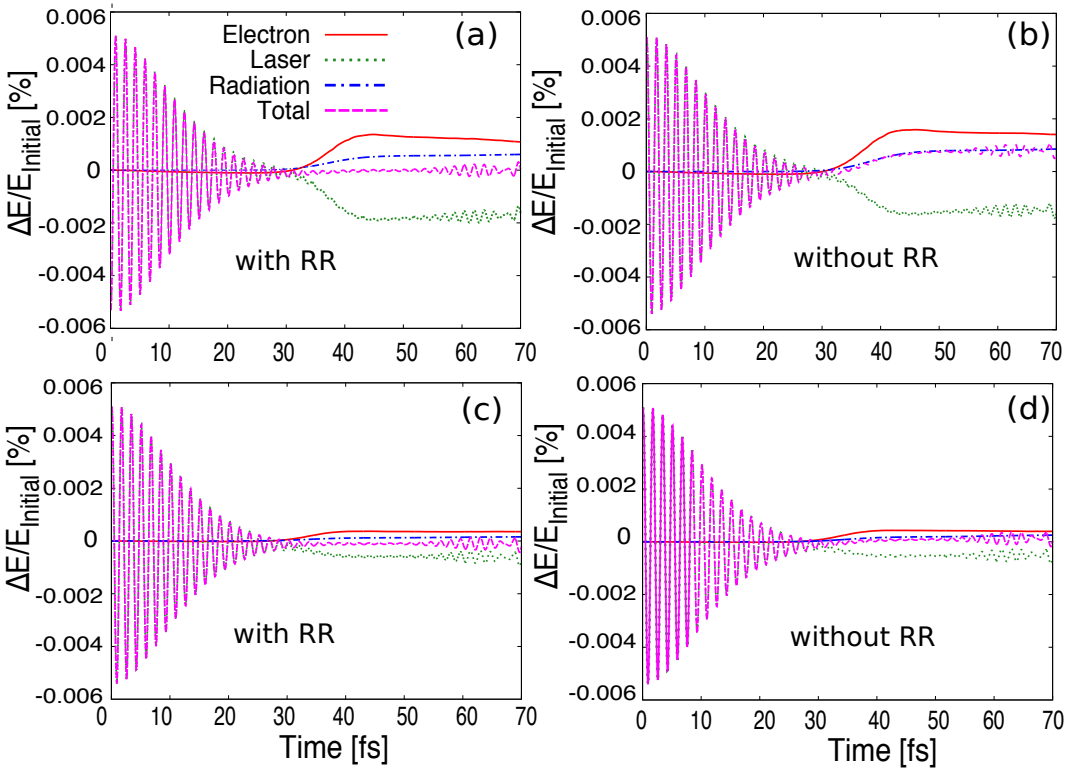

Figure 5.8: Time evolution of energy conservation (a) with RR and (b) without RR at the laser intensity of 2×10^{23} W/cm^2 while (c) with RR and (d) without RR for 10^{24} W/cm^2. The red line is electron energy balance while the green dotted line is the energy balance for laser field. The blue dash-dotted line is the energy balance for radiation emission. The pink dashed line is the total energy balance. The negative value indicates the energy loss of the electron or laser.

loss. For the cases where $a_0 >> \gamma_0$ most of the electrons are accelerated to higher energy and the Larmor radius changed. The choice of smaller grid size implies a larger number of grids are needed, and it is very challenging for 3-D simulation. Nevertheless, from the observation of Fig. 5.8, the energy balance is kept to an acceptable level.

5.4 Interaction of pulsed Gaussian laser beam with 1 GeV electron beam

After considered the case for an electron beam with an energy of 40 MeV in previous section, we proceed to study the same interaction by increasing the electron beam energy to 1 GeV. We focus on how the charge density and emission spectrum change as compared

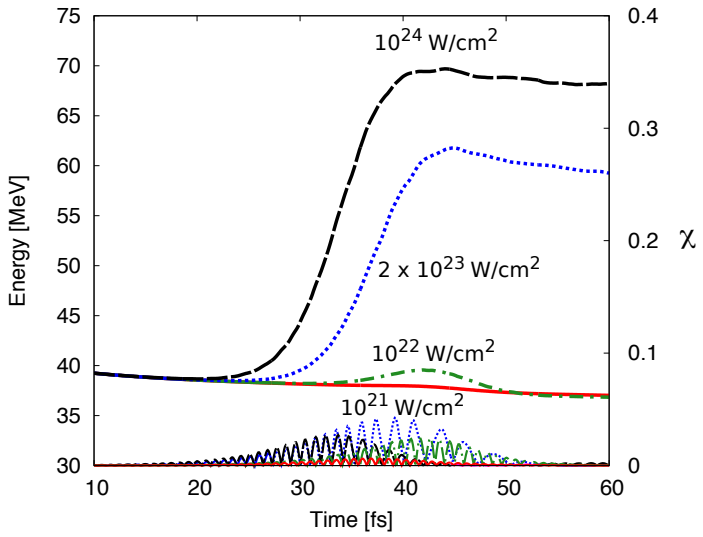

Figure 5.9: Time evolution of the average energy of 40 MeV electron beam for different laser intensities with the effects of RR included. The red solid line is at the laser intensity of 10^{21} W/cm^2, green dash-dotted line for 10^{22} W/cm^2, blue dotted line for 2×10^{23} W/cm^2 and black dashed line for 10^{24} W/cm^2. The χ parameter for different laser intensities are shown with corresponding colors at the bottom of the energy plots.

to the case of 40 MeV.

5.4.1 Results

The energy of electrons does not decrease throughout the whole process for the case without RR. Therefore, the charge density shown in Fig. 5.10 (a) & 5.11 (a) does not change. On the contrary, in Fig. 5.11 (b), the energy of electrons is lost into radiation emission at the beginning of the interaction. After that, those electrons with lower energy meet the condition $a_0 >> \gamma$ and being accelerated to higher energy. We can observe in Fig. 5.15 that the average energy loss is smaller than at the laser intensity of 10^{24} W/cm^2 as compared to 10^{23} W/cm^2. The strong ponderomotive force pushes the electrons in the direction away from the laser beam axis and increases the velocity parallel to E'_y.

The comparison of emission spectra, photon number distribution and photon angular distribution are shown in Fig. 5.12 & Fig. 5.13 at the laser intensity of 10^{23} W/cm^2 and 10^{24} W/cm^2 respectively. The peak locations of the emission spectra are shifted about 100 MeV at 10^{23} W/cm^2 in Fig. 5.12 (a) and more than 100 MeV at 10^{24} W/cm^2 in Fig. 5.13 (a). On the other hand, the difference in photon number between the case of RR and

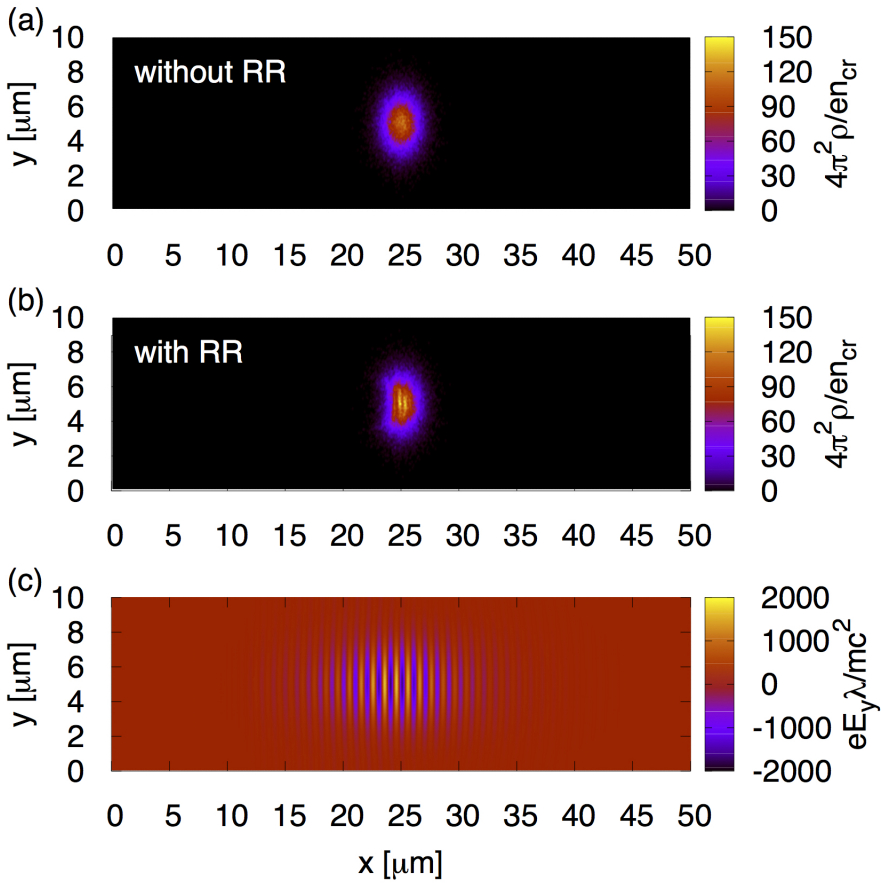

Figure 5.10: The charge density of 1 GeV electron beam (a) without RR, (b) with RR and (c) the field component E'_y at the laser intensity of 10^{23} W/cm^2 at the laser focusing region.

without RR becomes prominent starting from photon energy of 10 MeV at the laser intensity of 10^{23} W/cm^2 as shown in Fig. 5.12 (b). The electron beam emits about 7×10^{18} photons per pulse in 0.1 $\%$ bandwidth at the photon energy of 15 MeV for the case with RR, which is one order smaller than the case without RR. However, this difference is extended to lower photon energy at the laser intensity of 10^{24} W/cm^2 as shown in Fig. 5.13 (b). This is because there are a large number of electrons with velocity parallel to E'_y in strong field region for the case of RR as compared to the case without RR. This is in contrast to 40 MeV electron beam where parallel velocity components are the same for the cases with and without RR. Therefore, the production of low energy photon is significantly less for the case with RR. The electron beam emits about 9×10^{20} photons per pulse in 0.1 $\%$ bandwidth at the photon energy of 15 MeV for the case with RR, while

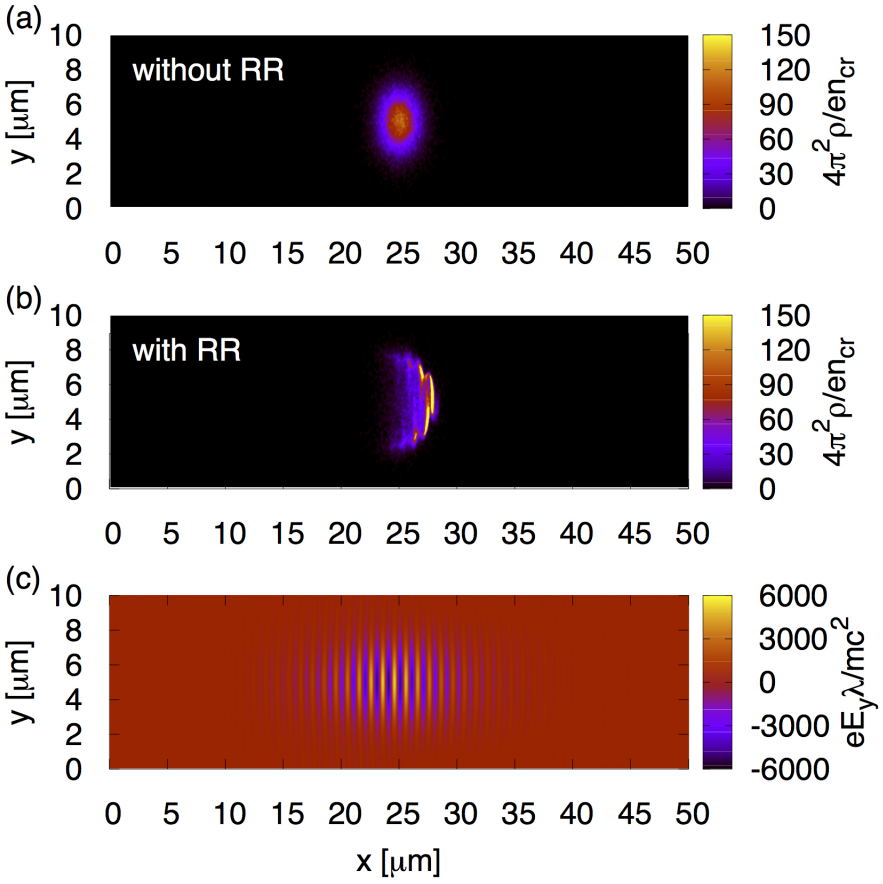

Figure 5.11: The charge density of 1 GeV electron beam (a) without RR, (b) with RR and (c) the field component E_y' at the laser intensity of 10^{24} W/cm^2 at the laser focusing region.

it is 1.2×10^{22} for the case without RR. Besides, the broadening of angular spread is as expected due to the decrease of average Lorentz factor and is stronger for higher laser intensity as seen in Fig. 5.12 (c) and Fig. 5.13 (c).

In addition, the time evolution of energy conservation at the laser intensity of 10^{23} W/cm^2 and 10^{24} W/cm^2 are shown in Fig. 5.14 for the case of with and without RR. In Fig. 5.14 (a), the laser field depletion is negligible and the radiation emission comes mostly from electron beam. It can be observed that at the laser intensity of 10^{24} W/cm^2, the energy difference for electron is -0.01 % and by adding the laser field depletion of -0.0025 % is equal to the radiation energy difference 0.0125 % as shown in Fig. 5.14 (c). This implies that the laser energy is transferred to the electrons and then converted into radiation emission. The negative value simply indicates the energy loss. The total energy

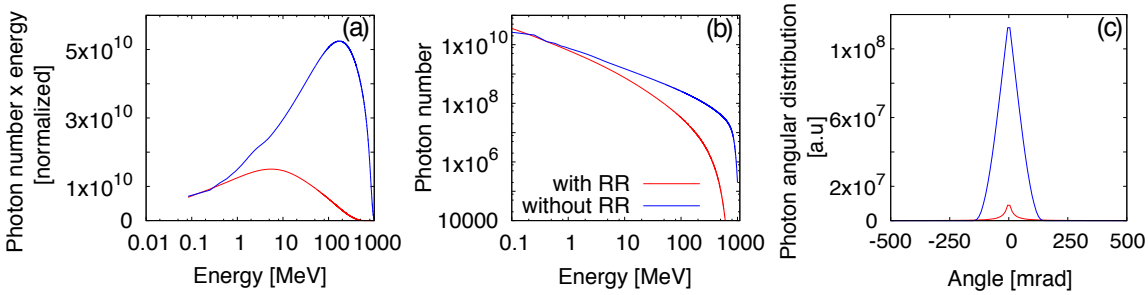

Figure 5.12: Comparison of (a) emission spectra, (b) photon number distribution and (c) photon angular distribution with RR and without RR at the laser intensity of 10^{23} W/cm^2. In 0.1 % bandwidth at 15 MeV photon energy, an electron beam emits about 7×10^{20} photons per pulse with RR while it is one order larger for the case without RR.

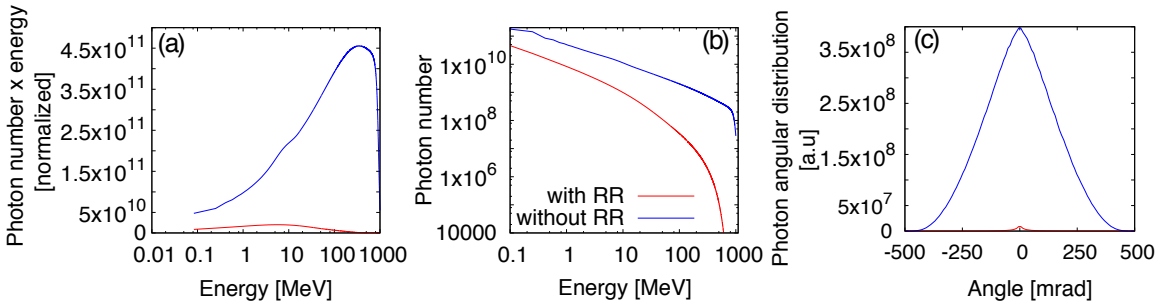

Figure 5.13: Comparison of (a) emission spectra, (b) photon number distribution and (c) photon angular distribution with and without RR at the laser intensity of 10^{24} W/cm^2. In 0.1 % bandwidth at 15 MeV photon energy, an electron beam emits about 9×10^{20} photons per pulse with RR while it is 1.2×10^{22} photons per pulse for the case without RR.

is conserved within 0.005 % for the case with RR for both intensities. On the other hand, the total energy is not conserved for the case without RR.

Figure 5.15 shows the time evolution of the average energy of 1 GeV electron beam. At electron energy of 1 GeV, the effects of RR is certainly significant for laser intensity more than 10^{21} W/cm^2 such that $R_C\xi_0 \gtrsim 0.5$. Besides, for the case of $a_0 << \gamma_0$ the electrons have enough energy to enter the centre of the laser field as observed in Fig. 5.10 & 5.11. The value of χ is then larger as compared to the case of 40 MeV electron beam. Even though the value of χ is greater than the case of 40 MeV, however, the pair production via non-linear Breit-Wheeler process is suppressed as discussed in Sec. 2.5.

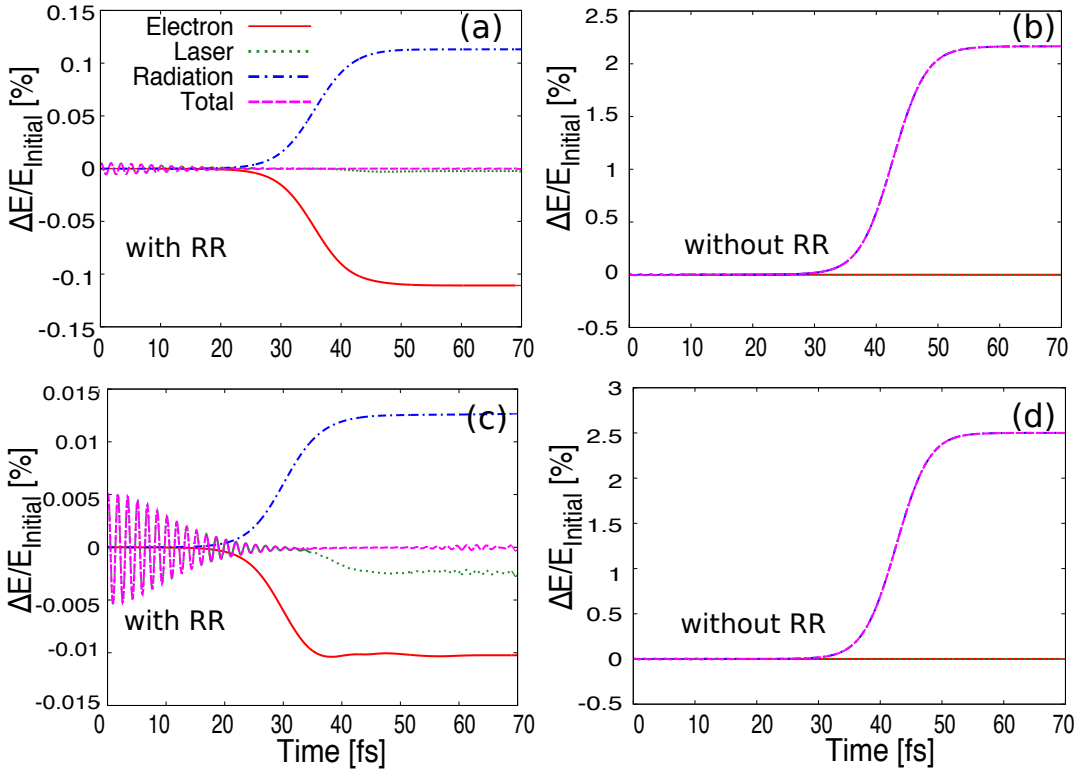

Figure 5.14: Time evolution of energy conservation (a) with RR and (b) without RR at the laser intensity of 10^{23} W/cm^2 while (c) with RR and (d) without RR for 10^{24} W/cm^2. The red line is electron energy balance while the green dotted line is the energy balance for laser field. The blue dash-dotted line is the energy balance for radiation emission. Pink dashed line is the total energy balance. The negative value indicates the energy loss of the electron or laser.

5.4.2 Discussions

From the observation, the effects of RR can be distinguished not only from the particle beam spread but also from the radiation spectra for 1 GeV electron beam interacts with the laser at the intensity of 10^{24} W/cm^2. If the laser pulse duration increases, the cumulative RR effect will be shown up with lower laser intensity and beam energy at experiment facilities such as ELI.

5.5 PIC vs non-PIC

From the previous section, we observed the laser field energy depletion for some situations via PIC simulation. Thus, it is essential for us to compare the difference of PIC method

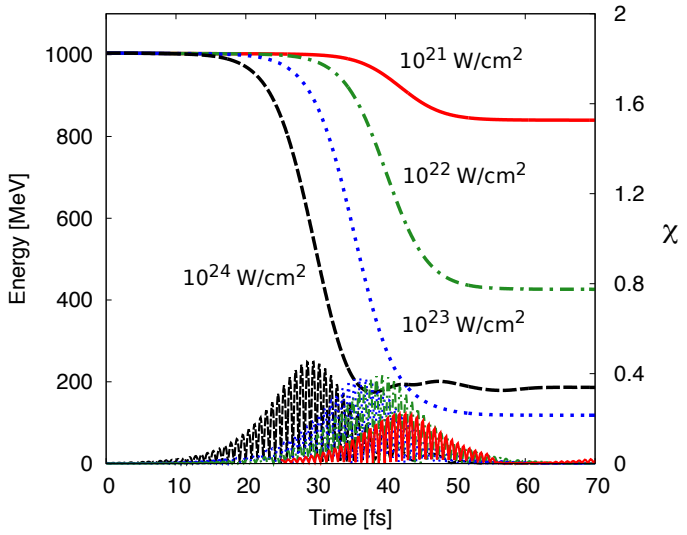

Figure 5.15: Time evolution of the average energy of 1 GeV electron beam at different laser intensities. The red solid line is at 10^{21} W/cm^2, green dash-dotted line at 10^{22} W/cm^2, blue dotted line at 10^{23} W/cm^2 and black dashed line at 10^{24} W/cm^2. The χ parameter at different laser intensities are shown with corresponding colors at the bottom of the energy plots.

to the method described in Sec. 3.1 and is referred as non-PIC. In the non-PIC method, a bunch of electrons is described by Eq. (3.2). Same laser parameters and beam conditions are assumed except that there is no momentum spread and longitudinal spread for the non-PIC method.

5.5.1 Results

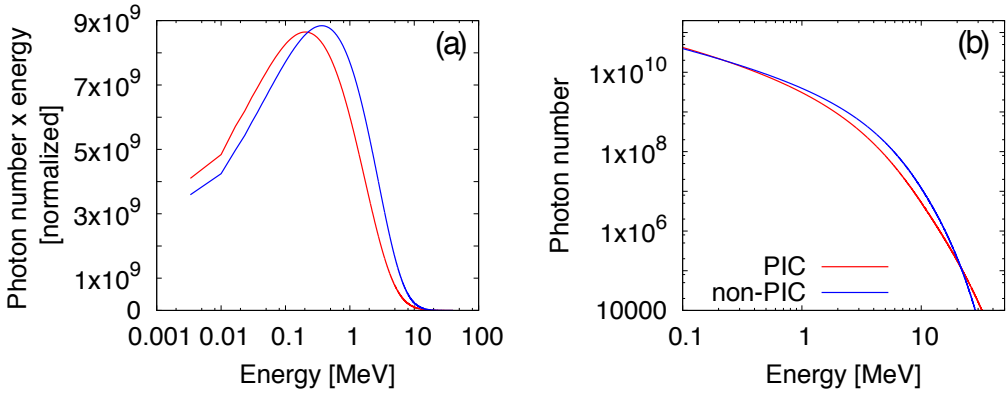

Figure 5.16: Comparison of (a) emission spectra and (b) photon number distribution for PIC (red solid line) and non-PIC (blue solid line) for a bunch of 10^9 electron with energy of 40 MeV interact with the laser intensity of 2×10^{23} W/cm^2.

Fig. 5.16 and 5.17 shows the difference on the emission spectra and photon number distribution at two laser intensities. It can be clearly observed that the difference is rather

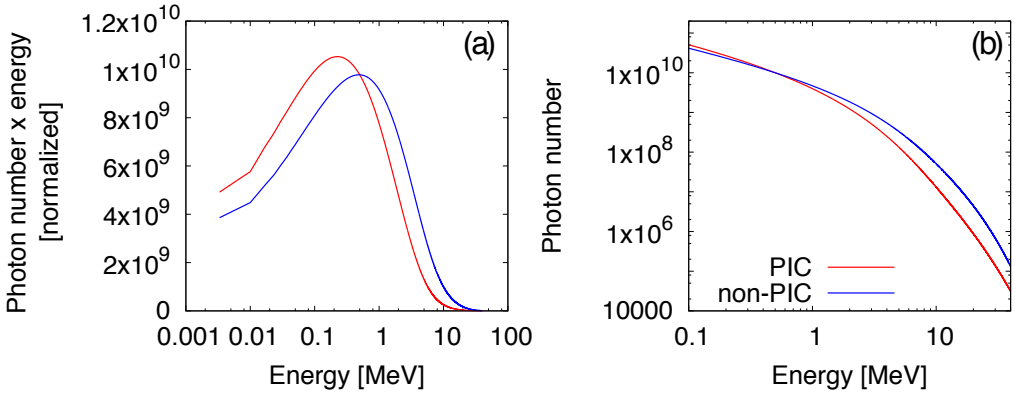

Figure 5.17: Comparison of (a) emission spectra and (b) photon number distribution for PIC (red solid line) and non-PIC (blue solid line) for a bunch of 10^9 electron with energy of 40 MeV interact with the laser intensity of 10^{24} W/cm^2.

small but not negligible. Small difference lies on the position of the peaks of the emission spectra in Fig. 5.16 (a) and 5.17 (a). Meanwhile the difference on the photon number distribution is small at the laser intensity of 2×10^{23} W/cm^2 in Fig. 5.16 (b). The difference on photon number distribution at the laser intensity of 10^{24} W/cm^2 begins from photon energy of 1 MeV. One of the reasons is that Larmor radius is not resolved by the grid in PIC method. In the non-PIC method, Maxwell's equations are not solved and therefore one can take spatial resolution as small as possible. However, in PIC method, smaller grid size would require a large number of cells and is very challenging for 3-D simulation. The second reason may due to the electron longitudinal and momentum beam spread that is not taken into account in the non-PIC method, but those effects are expected to be small. On the other hand, a similar comparison is shown in Fig. 5.18 for a bunch of 1.6×10^{10} electrons. The increase in the number of electrons in the regime $a_0 >> \gamma_0$ leads to the increases in the velocity parallel to E'_y and leads to higher electromagnetic work done.

The conversion efficiencies defined in Sec. 3.3.5 are compared to the single particle (blue square points), PIC (red square points) and non-PIC method (green triangle points) for 40 MeV electron beam in Fig. 5.19. The case of 1 GeV electron beam is shown in black crosses and joined with black dashed line in the same figure. In single particle model, an electron moves along the laser beam axis, and the interaction with the other field components is assumed to be negligible. When a finite beam size is considered,

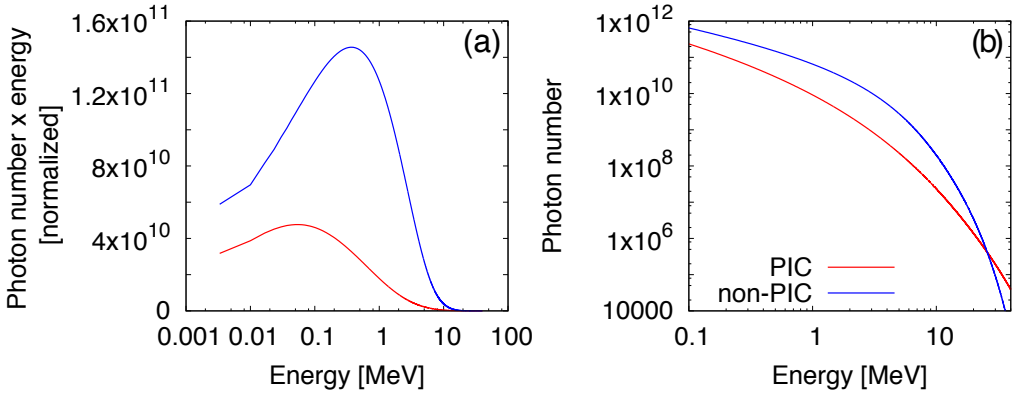

Figure 5.18: Comparison of (a) emission spectra and (b) photon number distribution for PIC (red solid line) and non-PIC (blue solid line) for a bunch of 1.6×10^{10} electron with energy of 40 MeV interact with the laser intensity of 2×10^{23} W/cm^2.

the conversion efficiencies are shifted to a lower value. The difference between PIC and non-PIC is certainly obvious at the laser intensity of 2×10^{23} W/cm^2 as the field depletion is large as shown in Fig. 5.8. The conversion efficiencies at the laser intensity of 10^{21} W/cm^2 and 10^{24} W/cm^2 are so close for the cases of PIC and single particle model. The strong ponderomotive force moves the electrons in the direction perpendicular to (away from) the laser beam. It means that the ponderomotive force does the work on the electrons, and the energy of the laser is carried away in the form of kinetic energy rather than radiation emission. As a consequence, the conversion efficiency is significantly reduced. When an electron beam with the energy of 1 GeV is considered, the ponderomotive force is overcome and the conversion efficiencies increase for all intensities.

5.5.2 Discussions

After taking into account the laser field depletion, the conversion efficiency at the laser intensity of 2×10^{23} W/cm^2 reduces to about 8 $\%$ while the remaining 92 $\%$ is carried away by the electrons. On the other hand, about 77 $\%$ of radiation energy is converted from the total of electromagnetic work and the initial kinetic energy of 1 GeV electron beam at the laser intensity of 10^{24} W/cm^2. More study should be carried out by means of PIC method to investigate whether the conversion efficiency will increase at the laser intensity of 10^{25} W/cm^2 and 10^{26} W/cm^2.

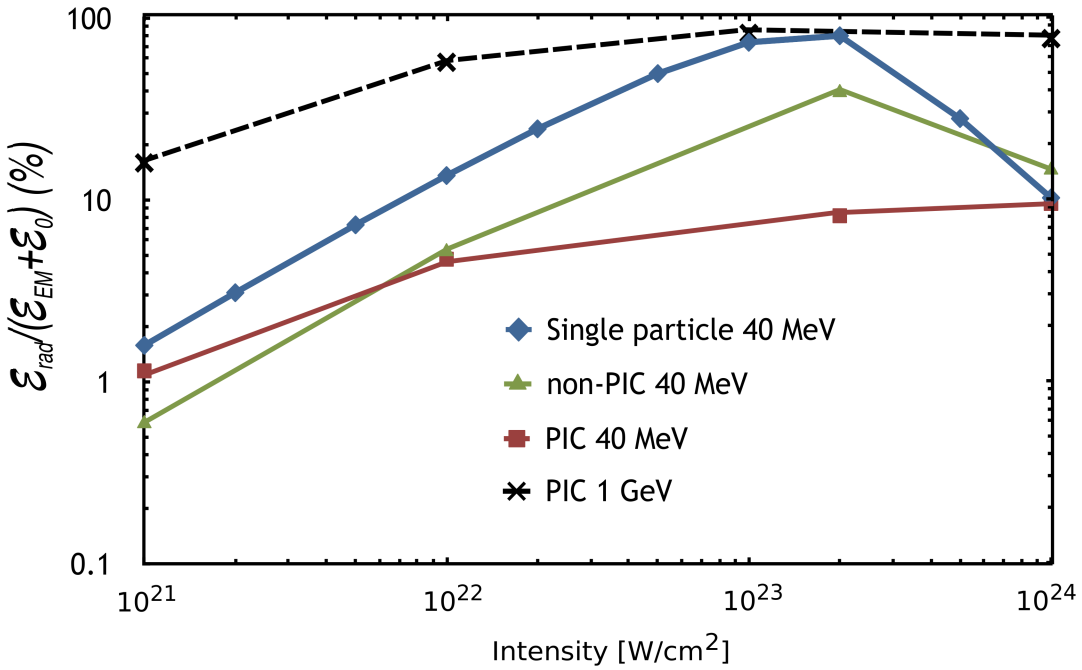

Figure 5.19: The radiation energy conversion from the total of electromagnetic work and its initial kinetic energy for single particle (blue square points), PIC (red square points), and non-PIC (green triangle points) for 40 MeV electron. The black crosses joined with the dashed line are the case of 1 GeV electron beam via PIC method.

5.6 Summary

In summary, we have shown the 3D PIC simulation results for the interaction of a pulsed Gaussian beam at different laser intensity with 40 MeV and 1 GeV electron beam. We considered a 10 fs laser pulse being focused to the waist radius of 2 μm. The longitudinal and transverse spread of 1 μm and 5 $\%$ of energy spread were assumed. We observed that the ponderomotive force plays a crucial role in determining the radiation emission at the laser intensity of 10^{23} W/cm^2 and 10^{24} W/cm^2. This force serves as a barrier to the electron with lower energy to enter the laser pulse and leads to the reduction of the radiation emission. If an electron beam with higher energy passes through the laser pulses of the above intensities, higher conversion efficiency will be obtained.

Chapter 6

Conclusions

In this thesis, we studied the dynamics of an electron in the strong laser field by including the effects of radiation reaction by employing the Sokolov model. The time evolution of electron energy, gamma ray emission spectra, photon number distribution and photon angular distribution are studied for electron energies 10 MeV to 1 GeV for laser intensities 10^{21} W/cm^2 to 10^{24} W/cm^2.

We defined the conversion efficiency to be the radiation energy conversion from the sum of initial electron energy and electromagnetic work done. We presented the conversion efficiencies of 40 MeV electron at different laser intensities and pulse durations. An optimum conversion efficiency was observed at the laser intensity of 2×10^{23} W/cm^2 and 10 fs pulse duration.

For a single particle, the laser energy depletion is negligibly small and we can assume the energy of the laser to be constant. However, for a realistic situation such as a bunch of 10^9 electrons, the laser energy depletion have to be taken into account. To do so, we solved Maxwell's equations self-consistently via Particle-in-cell method. We performed 3D PIC simulations for the interaction of a 10 fs pulsed Gaussian beam at laser intensities 2×10^{23} W/cm^2 and 10^{24} W/cm^2 with 40 MeV electron beam at ELBE, HZDR. The same interaction was studied at the laser intensity of 10^{23} W/cm^2 and 10^{24} W/cm^2 with 1 GeV electron beam to compare the effects of electron energy to the ponderomotive force.

6. CONCLUSIONS

The field components of the pulsed Gaussian beam are analysed. We studied the charge density distribution for these electron beams, the emission spectrum, photon number distribution, photon angular distribution and energy conservation with and without RR included. We then compared the results of PIC simulation with the non-PIC method. The results are summarized as follows:

- By including the effects of RR, the amplitude of electron oscillation is larger than the case without RR due to the decreases of the electron energy or the Lorentz factor. This, in turn, leads to the reduction of electron effective mass in the field.

- For the case $a_0 << \gamma_0$, the ponderomotive force is small, and the electron has sufficient energy to pass through the laser field. However, for the case $a_0 >> \gamma_0$, the ponderomotive force dominates. The electron does not have sufficient kinetic energy to overcome the ponderomotive potential, and its trajectory is reversed.

- The cumulative effects of RR lead to the suppression of the peak locations of emission spectra as we increase the initial kinetic energy of the electron. Such suppression is small for 10 fs laser pulse.

- The effects of RR also reduces the production of high energy photon and broaden the angular distribution due to the decreases of electron energy.

- An electron with an energy of 40 MeV would convert up to 80 $\%$ of the total of electromagnetic work and its initial kinetic energy when interacting with 10 fs laser pulse at intensity 2×10^{23} W/cm^2.

- When we treated the interaction self-consistently, however, the conversion efficiency reduces to 8 $\%$ due to the laser field energy depletion. The laser field energy reduction is sensitive to the motion of the electron perpendicular to the laser beam as a consequence of large ponderomotive force. As the energy of the electron beam increases, the laser energy reduction becomes relatively small.

To generate high-intensity gamma ray with high conversion efficiency at the energy range of 10 - 20 MeV by using the high-intensity laser above 10^{23} W/cm^2, we emphasized that

an electron beam with energy more than 1 GeV be required to overcome the ponderomotive potential from the laser field. The same requirement is also necessary in order to observe a clear signature of radiation reaction in the radiation spectrum at high power laser facility such as ELI where the laser intensity is expected to reach the order of 10^{23-26} W/cm^2.

Appendix A

Applications

Various kind of radioisotopes (RIs) are being used for nuclear physics, medicine and other applied science. For instance, RI Technetium (^{99m}Tc, half-life = 6 hours) are major ingredients for nuclear medicine imaging technique by using gamma rays in Single Photon Emission Computed Tomography (SPECT) while Molybdenum (^{99m}Mo, half-life = 66 hours) being the source for ^{99m}Tc production. RI productions and transmutation are usually proceeding via (n,γ) reaction and nuclear fission. However, RIs produced from such methods are not purely of desired RI but in addition with other RIs. The extraction and separation of the desired RIs are necessary but expensive.

On the other hand, resonant photonuclear isotope transmutation (RPIT) was recently reported [59] to be a promising way in the production of the desired RIs. This method uses resonant photonuclear (γ, n) and (γ, 2n) reactions through isovector E1 giant resonance (GR) for RPIT. The energetic photon beam to be used is obtained from laser Thomson/Compton backscattering off GeV electron. The resonant photonuclear GR reaction possesses the following advantages as candidates for RIs production. First, the cross section of GR is large because of resonant excitation of many nucleons. The cross section at GR energy is written as $\sigma(GR) \approx 2.5 \times 10^{-3}$A b, where A is the mass number. Second, the resonance width and resonance energy are insensitive to the individual nuclear structure. The resonance energy can be expressed as $E(GR) \approx aA^{-1/5} = 14 - 22$ MeV for A = 30 - 200 nuclei [see Fig. A.1]. Third, photonuclear reactions on medium-heavy nuclei

at GR energy are mostly (γ, n) and (γ, 2n) reactions. Nuclei with (Z, N-1) and (Z, N-2) are expected to be obtained. For light nuclei, (γ, p) reactions are used to obtain nuclei with (Z-1, N). Thus, the production of desire RIs seems promising. It was demonstrated that with medium-energy γ rays at the intensity of the order of $10^6/s$ irradiated on ^{100}Mo and ^{197}Au, RIs ^{99}Mo/^{99m}Tc and ^{196}Au production were observed. From that, RPIT with photon intensity of the order of $10^{13-15}/s$ is expected to produce RIs of ^{99}Mo/^{99m}Tc with the rate of $10^{11-13}/s$ and RI density of 0.5-50 G Bq/mg for many applications such as SPECT.

Besides, RPIT can be utilized for nondestructive high-sensitivity detection of nuclear isotopes called resonant photonuclear isotope detection (RPID) [60]. RPID uses RPIT to transmute impurity isotopes to RIs and measure the γ rays from RIs decay. For instance, H. Ejiri et al reported that the sensitivity of RPID of ^{196}Au RIs produced by RPIT from ^{197}Au in Mo-Au sample was measured to be around 5 ppm or lower by using Ge detector. For photon intensity of the order of $10^{13-15}/s$ one may expect the detection sensitivity up to ppt level. The source of energetic photon beam obtained from laser Thomson/Compton backscattering off GeV electron is chosen due to its unique feature of small beam divergence around 0.5 mrad for 1 GeV electron. This implies that it is possible to obtain high-density RI of the order of G Bq/mg. In addition, the photon energy of 16 MeV at GR energy can be obtained by tuning the energy of electron beam. This energy is more than the neutron binding energy of 8 MeV and is more than sufficient for photonuclear reactions. In contrast, photon produced from bremsstrahlung drop rapidly as the energy of electron increases and not effective for photonuclear reactions [1].

With present laser technologies and synchrotron facilities, energetic photon sources are available at HIγS with Free Electron Laser (FEL) [61], NewSUBARU with Nd-YVO_4 laser and others [62]. The photon production rate at HIγS by using 1.6 eV FEL and the electron with energy 0.475 GeV is the order of $10^9/s$. Meanwhile in NewSUBARU electrons with energy around 1 GeV and backscattered off with 1.064μm laser to produce photons with the energy of 6-17 MeV [62]. The photon production rate which was used by H. Ejiri et al was measured to be the order of $10^6/s$ [59]. Generation of MeV range

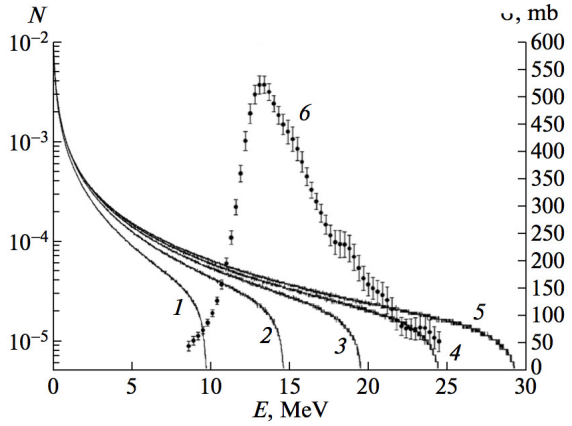

Figure A.1: Spectrum of bremsstrahlung gamma-quanta that hit the sample of the studied substance for a tungsten bremsstrahlung target 0.1 mm thick. Curves 1, 2, 3, 4, and 5 correspond to the energy of electrons E^m 10, 15, 20, 25, and 30 MeV respectively; curve 6 is the excitation cross section of GDR at the nucleus ^{197}Au. The left scale corresponds to curves 1–5, the right scale corresponds to excitation cross section of GDR at the nucleus ^{197}Au [1].

.

and ultra high brightness γ rays by nonlinear Thomson scattering of the ultrarelativistic laser-wakefield-accelerated electron beam was also reported recently [20]. On the other hand, a new generation of photon sources are being planned in Extreme Light Infrastructure (ELI) [4] with photon production rate of the order of $10^{13}/s$ by using laser intensity of the order of 10^{23-24} W/cm^2.

Bibliography

[1] B. S. Ishkhanov and Troschiev S. Yu. Bremsstrahlung target for studying photonuclear reactions in the giant dipole resonance energy region. *Mos. Univ. Phys. Bull.*, 65:39, 2010. xvi, 85, 86

[2] Gerard A. Mourou, Toshiki Tajima, and Sergei V. Bulanov. Optics in the relativistic regime. *Rev. Mod. Phys.*, 78:309–371, Apr 2006. 1

[3] V. Yanovsky, V. Chvykov, G. Kalinchenko, P. Rousseau, T. Planchon, T. Matsuoka, A. Maksimchuk, J. Nees, G. Cheriaux, G. Mourou, and K. Krushelnick. Ultra-high intensity- 300-tw laser at 0.1 hz repetition rate. *Opt. Express*, 16(3):2109–2114, 2008. 1

[4] Gerard A. et al Mourou. *ELI-Extreme Light Infrastructure Science and Technology with Ultra-Intense Lasers WHITE-BOOK*. Berlin: THOSS Media GmbH, 2011. 1, 86

[5] A. Di Piazza, C. Müller, K. Z. Hatsagortsyan, and C. H. Keitel. Extremely high-intensity laser interactions with fundamental quantum systems. *Rev. Mod. Phys.*, 84:1177–1228, Aug 2012. 1, 16

[6] A. R. Bell and John G. Kirk. Possibility of prolific pair production with high-power lasers. *Phys. Rev. Lett.*, 101:200403, Nov 2008. 2

[7] J G Kirk, A R Bell, and I Arka. Pair production in counter-propagating laser beams. *Plasma Physics and Controlled Fusion*, 51(8):085008, 2009. 2, 17, 25, 67

[8] A. M. Fedotov, N. B. Narozhny, G. Mourou, and G. Korn. Limitations on the attainable intensity of high power lasers. *Phys. Rev. Lett.*, 105:080402, Aug 2010. 2

[9] N. V. Elkina, A. M. Fedotov, I. Yu. Kostyukov, M. V. Legkov, N. B. Narozhny, E. N. Nerush, and H. Ruhl. Qed cascades induced by circularly polarized laser fields. *Phys. Rev. ST Accel. Beams*, 14:054401, May 2011. 2

[10] V. F. Bashmakov, E. N. Nerush, I. Yu. Kostyukov, A. M. Fedotov, and N. B. Narozhny. Effect of laser polarization on quantum electrodynamical cascading. *Physics of Plasmas (1994-present)*, 21(1):–, 2014. 2

[11] Remo Ruffini, Gregory Vereshchagin, and She-Sheng Xue. Electron–positron pairs in physics and astrophysics: From heavy nuclei to black holes. *Physics Reports*, 487(1–4):1 – 140, 2010. 2

[12] Esirkepov, T.Zh. and Bulanov, S.V. Fundamental physics and relativistic laboratory astrophysics with extreme power lasers. *EAS Publications Series*, 58:7–22, 2012. 2

[13] A. Di Piazza, K. Z. Hatsagortsyan, and C. H. Keitel. Strong signatures of radiation reaction below the radiation-dominated regime. *Phys. Rev. Lett.*, 102:254802, Jun 2009. 2, 16

[14] H. A. Lorentz. *The Theory of Electron*. Teubner, Leipzig, 1909. 2

[15] A. Abraham. *Theorie der Elektrizität*. Teubner, Leipzig, 1905. 2

[16] P. A. M. Dirac. Classical theory of radiating electrons. *Proc. R. Soc. A*, 167:148, 1938. 2, 10

[17] L. D. Landau and E. M. Lifshitz. *The Classical Theory of Fields*, volume 2 of *Course of theoretical physics*. Butterworth Heinemann, 1975. 3, 12, 37

[18] R. T. Hammond. *EJTP*, 7:221, 2010. 3, 13

[19] A. G. R. Thomas, C. P. Ridgers, S. S. Bulanov, B. J. Griffin, and S. P. D. Mangles. Strong radiation-damping effects in a gamma-ray source generated by the interaction of a high-intensity laser with a wakefield-accelerated electron beam. *Phys. Rev. X*, 2:041004, 2012. 4, 5

[20] G. Sarri, D. J. Corvan, W. Schumaker, J. M. Cole, A. Di Piazza, H. Ahmed, C. Harvey, C. H. Keitel, K. Krushelnick, S. P. D. Mangles, Z. Najmudin, D. Symes, A. G. R. Thomas, M. Yeung, Z. Zhao, and M. Zepf. Ultrahigh brilliance multi-mev γ-ray beams from nonlinear relativistic thomson scattering. *Phys. Rev. Lett.*, 113:224801, Nov 2014. 4, 26, 86

[21] James Koga, Timur Zh. Esirkepov, and Sergei V. Bulanov. Nonlinear thomson scattering in the strong radiation damping regime. *Physics of Plasmas (1994-present)*, 12:093106, 2005. 5, 16

[22] I.V. Sokolov, N. M. Naumova, J. A. Nees, G. A. Mourou, and V. P. Yanovsky. Dynamics of emitting electrons in strong laser fields. *Phys. Plasmas*, 16:093115, 2009. 5, 13, 15

[23] T. Nakamura, J. K. Koga, T. Zh. Esirkepov, M. Kando, G. Korn, and S. V. Bulanov. High-power γ-ray flash generation in ultraintense laser-plasma interactions. *Phys. Rev. Lett.*, 108:195001, 2012. 5

[24] C. Bula, K. T. McDonald, E. J. Prebys, C. Bamber, S. Boege, T. Kotseroglou, A. C. Melissinos, D. D. Meyerhofer, W. Ragg, D. L. Burke, R. C. Field, G. Horton-Smith, A. C. Odian, J. E. Spencer, D. Walz, S. C. Berridge, W. M. Bugg, K. Shmakov, and A. W. Weidemann. Observation of nonlinear effects in compton scattering. *Phys. Rev. Lett.*, 76:3116–3119, Apr 1996. 5

[25] A. Jochmann, A. Irman, M. Bussmann, J. P. Couperus, T. E. Cowan, A. D. Debus, M. Kuntzsch, K. W. D. Ledingham, U. Lehnert, R. Sauerbrey, H. P. Schlenvoigt, D. Seipt, Th. Stöhlker, D. B. Thorn, S. Trotsenko, A. Wagner, and U. Schramm.

High resolution energy-angle correlation measurement of hard x rays from laser-thomson backscattering. *Phys. Rev. Lett.*, 111:114803, Sep 2013. 5

[26] Mathias Siebold, Fabian Roeser, Markus Loeser, Daniel Albach, and Ulrich Schramm. Penelope: a high peak-power diode-pumped laser system for laser-plasma experiments, 2013. 5

[27] J.D. Jackson. *Classical Electrodynamics*. Wiley, 1975. 7, 37

[28] F. Rohrlich. *Nuovo Cimento*, 21:811, 1961. 10

[29] Claudio Teitelboim. Splitting of the maxwell tensor: Radiation reaction without advanced fields. *Phys. Rev. D*, 1:1572–1582, 1970. 10

[30] I. V. Sokolov, N. M. Naumova, and J. A. Nees. Numerical modeling of radiation-dominated and quantum-electrodynamically strong regimes of laser-plasma interaction. *Phys. Plasmas*, 18:093109, 2011. 13, 18, 23, 38

[31] I.V. Sokolov. Renormalization of the Lorentz-Abraham-Dirac equation for radiation reaction force in classical electrodynamics. *J. Exp. Theor. Phys*, 109:207, 2009. 13, 14

[32] David A. Burton and Adam Noble. Aspects of electromagnetic radiation reaction in strong fields. *Contemporary Physics*, 55(2):110–121, 2014. 15

[33] Rémi Capdessus, Adam Noble, Paul McKenna, and Dino A. Jaroszynski. Role of momentum and velocity for radiating electrons. *Phys. Rev. D*, 93:045034, Feb 2016. 15

[34] Anton Ilderton and Greger Torgrimsson. Radiation reaction from qed: Lightfront perturbation theory in a plane wave background. *Phys. Rev. D*, 88:025021, Jul 2013. 15

[35] A.Di Piazza. Exact solution of the landau-lifshitz equation in a plane wave. *Lett. Math. Phys.*, 83:305–313, 2008. 16

[36] A. Di Piazza, K. Z. Hatsagortsyan, and C. H. Keitel. Quantum radiation reaction effects in multiphoton compton scattering. *Phys. Rev. Lett.*, 105:220403, Nov 2010. 17

[37] Thomas Erber. High-energy electromagnetic conversion processes in intense magnetic fields. *Rev. Mod. Phys.*, 38:626–659, Oct 1966. 17

[38] Igor V. Sokolov, John A. Nees, Victor P. Yanovsky, Natalia M. Naumova, and Gérard A. Mourou. Emission and its back-reaction accompanying electron motion in relativistically strong and qed-strong pulsed laser fields. *Phys. Rev. E*, 81:036412, Mar 2010. 17

[39] V.B. Berestetskii, E.M. Lifshitz, and L.P. Pitaevskii. *Quantum Electrodynamics*. Course of theoretical physics. Butterworth-Heinemann, 1982. 18

[40] E. N. Nerush, I. Yu. Kostyukov, A. M. Fedotov, N. B. Narozhny, N. V. Elkina, and H. Ruhl. Laser field absorption in self-generated electron-positron pair plasma. *Phys. Rev. Lett.*, 106:035001, 2011. 18

[41] G. Breit and John A. Wheeler. Collision of two light quanta. *Phys. Rev.*, 46:1087–1091, Dec 1934. 19

[42] S. S. Bulanov, C. B. Schroeder, E. Esarey, and W. P. Leemans. Electromagnetic cascade in high-energy electron, positron, and photon interactions with intense laser pulses. *Phys. Rev. A*, 87:062110, Jun 2013. 19

[43] W. P. Leemans, A. J. Gonsalves, H.-S. Mao, K. Nakamura, C. Benedetti, C. B. Schroeder, Cs. Tóth, J. Daniels, D. E. Mittelberger, S. S. Bulanov, J.-L. Vay, C. G. R. Geddes, and E. Esarey. Multi-Gev electron beams from capillary-discharge-guided subpetawatt laser pulses in the self-trapping regime. *Phys. Rev. Lett.*, 113:245002, Dec 2014. 20

[44] D. Habs, T. Tajima, and V. Zamfir. Extreme light infrastructure–nuclear physics (ELI–NP): New horizons for photon physics in europe. *Nuclear Physics News*, 21:23, 2011. 20

[45] J. Teichert, A. Arnold, H. Büttig, M. Justus, T. Kamps, U. Lehnert, P. Lu, P. Michel, P. Murcek, J. Rudolph, R. Schurig, W. Seidel, H. Vennekate, I. Will, and R. Xiang. Free-electron laser operation with a superconducting radio-frequency photoinjector at {ELBE}. *Nuclear Instruments and Methods in Physics Research Section A: Accelerators, Spectrometers, Detectors and Associated Equipment*, 743:114 – 120, 2014. 20, 42

[46] A. Piel. *Plasma Physics: An Introduction to Laboratory, Space, and Fusion Plasmas*. Springer Berlin Heidelberg, 2010. 22

[47] A. Macchi. *A Superintense Laser-Plasma Interaction Theory Primer*. SpringerBriefs in Physics. Springer Netherlands, 2013. 22

[48] Y.I. Salamin. Fields of a gaussian beam beyond the paraxial approximation. *Applied Physics B*, 86(2):319–326, 2007. 28, 57

[49] K. T. McDonald. Gaussian laser beams and particle acceleration. http://www.hep.princeton.edu/ mcdonald/examples/gaussian.pdf. 28, 57

[50] K. T. McDonald. Gaussian laser beams with radial polarization. http://www.hep.princeton.edu/%7Emcdonald/examples/axicon.pdf. 28, 57

[51] Kane Yee. Numerical solution of initial boundary value problems involving maxwell's equations in isotropic media. *IEEE Transactions on Antennas and Propagation*, 14(3):302–307, May 1966. 52

[52] T. Zh. Esirkepov. Exact charge conservation scheme for particle-in-cell simulation with an arbitrary form-factor. *Computer Physics Communications*, 135(2):144 – 153, 2001. 53

[53] J. P. Boris. Proceeding of the 4th conference on numerical simulation of plasmas. naval res. lab. pages 3–67, November 2009. 53

[54] M. Vranic, J. L. Martins, R. A. Fonseca, and L. O. Silva. Classical Radiation Reaction in Particle-In-Cell Simulations. *ArXiv e-prints*, February 2015. 57

[55] L. W. Davis. Theory of electromagnetic beams. *Phys. Rev. A*, 19:1177–1179, Mar 1979. 59

[56] J. P. Barton and D. R. Alexander. Fifth-order corrected electromagnetic field components for a fundamental gaussian beam. *Journal of Applied Physics*, 66(7), 1989. 59

[57] Yousef I. Salamin, Guido R. Mocken, and Christoph H. Keitel. Electron scattering and acceleration by a tightly focused laser beam. *Phys. Rev. ST Accel. Beams*, 5:101301, Oct 2002. 60

[58] V. I. Ritus. Quantum effects of the interaction of elementary particles with an intense electromagnetic field. *Journal of Soviet Laser Research*, 6(5):497–617, 1985. 67

[59] H. Ejiri, T. Shima, S. Miyamoto, K. Horikawa, Y. Kitagawa, Y. Asano, S. Daté, and Y. Ohashi. Resonant photonuclear reactions for isotope transmutation. *J. Phys. Soc. Jpn.*, 80:094202, 2011. 84, 85

[60] H. Ejiri and T. Shima. Resonant photonuclear isotope detection using medium-energy photon beam. *Phys. Rev. ST Accel. Beams*, 15:024701, 2012. 85

[61] H. R. Weller, Mohammad W. Ahmed, H. Gao, W. Tornow, Ying K. Wu, M. Gai, and R. Miskimen. Research opportunities at the upgraded hiγs facility. *Prog. Part. Nucl. Phys*, 62:257 – 303, 2009. 85

[62] NewSUBARU BL01 laser compton gamma ray. `http://www.lasti.u-hyogo.ac.jp/NS-en/facility/bl01/`. 85